이학박사 학위논문

Individually addressable hybrid dimensional nanoarchitecture device arrays

개별 어드레싱이 가능한 복합차원 나노소자 어레이

2018년 2월

서울대학교 대학원
물리 천문 학부
최 영 빈

Doctoral Thesis

Individually addressable hybrid dimensional nanoarchitecture device arrays

Youngbin Tchoe

Department of Physics and Astronomy

Seoul National University 2018

Individually addressable hybrid dimensional nanoarchitecture device arrays

개별 어드레싱이 가능한 복합차원 나노소자 어레이

지도교수 이규철

이 논문을 이학박사학위논문으로 제출함

2017년 12월

서울대학교 대학원

물리 • 천문학부

최영빈

최영빈의 박사학위 논문을 인준함

2017년 12월

위원장 김대식

부위원장 이규철

위원 이탁희

위원 김도헌

위원 홍영준

DMS 201123283

최영빈 Youngbin Tchoe, Individually addressable hybrid dimensional nanoarchitecture device arrays, 개별 어드레싱이 가능한 복합차원 나노소자 어레이, Department of Physics and Astronomy, and Institute of Applied Physics, 2018, P 184, Adviser: Prof. Gyu-Chul Yi, Text in English

Abstract

One-dimensional (1D) semiconductor nanomaterial arrays grown on two-dimensional (2D) layered nanomaterials can provide an excellent platform for realizing novel electronic and optoelectronic devices by synergistically combining the unique physical properties of 1D and 2D nanomaterials. 1D semiconductor nanomaterials work as efficient channels for carrier transport, thereby greatly improving the device performances of electronic and optoelectronic devices. Moreover, graphene layers, which have excellent electrical and thermal conductivities, and high mechanical strength and elasticity, are novel substrates that offer new functionalities such as transferability and flexibility. This dissertation presents the fabrication and characteristics of individually addressable nanorod device arrays based on 1D+2D hybrid dimensional nanomaterials.

Ultrathin, flexible, and individually addressable ZnO nanorod device arrays on graphene layers were demonstrated. Using this system, we investigated the individual electrical characteristics of single ZnO nanorod within the arrays. Additionally, based on the optoelectronic and piezoelectronic characteristics of ZnO nanorods, we investigated photodetector and pressure sensor characteristics of the nanorod device arrays. Moreover, light-emitting diode (LED) arrays were fabricated

using GaN/ZnO coaxial nanorod heterostructure arrays and their device characteristics were investigated. Metal-cored nitride microtube structures are discussed as a method to significantly improve nanostructured LED performance by improving the current-spreading characteristics.

In addition to 1D+2D hybrid dimensional nanomaterial-based devices, semiconductor microstructure arrays grown on graphene substrates were used to show their potential for microdisplay. GaN microdisk LED arrays grown on graphene dots were assembled in ultrathin and individually addressable crossbar array for flexible, high-resolution microdisplay. Furthermore, for full-color microdisplay, morphology-controlled GaN microdonut-shaped and micropyramidal LEDs were used to demonstrate variable-color light-emitters. The interesting electrical and electroluminescence characteristics of the GaN nanoarchitecture LEDs are presented. The origin of multicolor emission is also investigated by analysing the structure and chemical composition of the LEDs by TEM.

The catalyst-free molecular beam epitaxy (MBE) growth of $In_xGa_{1-x}As$/InAs coaxial nanorod heterostructures on graphene layers are also demonstrated. Transmission electron microscopy (TEM) was used to investigate the crystallinity of the arsenide nanorods grown on graphene layers. Additionally, RHEED was used to investigate the growth behavior of nanorods on graphene layers in real time.

Finally, monolithic integration of wide and narrow band gap semiconductor nanorods vertically on each surface of graphene are demonstrated by showing InAs nanorods/graphene layers/ZnO nanorods double heterostructures. Their structural characteristics are investigated by both the cross-sectional and plan view TEM. Moreover, their dual-wavelength photodetector characteristics are demonstrated.

Table of contents

List of figures

Introduction

1

1.1. Hybrid dimensional nanomaterials and nanodevices

One-dimensional (1D) semiconductor nanomaterials, such as nanorods, nanowires, and nanotubes, have attracted tremendous attention as building blocks for future integrated electronic and optoelectronic devices due to their unique physical properties and high potential to be integrated into ultrahigh density devices.[4-6] Although many novel nanodevices based on 1D semiconductor nanomaterials have already been demonstrated,[7, 8] the high-density assembly of 1D nanomaterial devices has been extremely challenging, both because of the difficulties in preparing regular arrays of 1D nanomaterials and the problems in making devices that can address each 1D nanomaterial individually in the array. This dissertation suggests that these obstacles can be overcome using 1D semiconductor nanostructure arrays grown on two-dimensional (2D) nanomaterials such as graphene. Position- and morphology-controlled 1D semiconductor nanomaterial arrays grown on graphene layers, which have recently become available,[9] can provide an excellent platform for realizing high-density integrated semiconductor nanodevice arrays. Additionally, precisely aligned microelectrodes can be formed both on the top and bottom surfaces of the 1D+2D hybrid dimensional nanomaterials after lifting-off them from the substrate, so that individually addressable 1D nanomaterial device arrays can be realized. Furthermore, in these 1D+2D hybrid dimensional nanomaterials, 1D semiconductor nanomaterials work as efficient channels for carrier transport, thereby greatly improving the device performances of electronic and optoelectronic devices.[10, 11] Moreover, the graphene layers, which have excellent electrical and thermal conductivities, and high mechanical strength and elasticity, are novel substrates that offer new functionalities such as transferability and flexibility.[12-14] This dissertation presents the fabrication and characteristics of individually addressable nanodevice arrays based on 1D+2D hybrid dimensional nanoarchitectures.

1.2. Objective and approach

The present research focused on the fabrication of ultrathin and high-density nanorod device arrays using high-quality semiconductor nanoarchitectures grown on graphene. For the material preparation on graphene, selective-area metal-organic chemical vapor deposition (SA-MOCVD) and catalyst-free molecular beam epitaxy (MBE) growth techniques were used, which have the advantages of large-area growth capability and a relatively simple and accurate doping and thickness control. Moreover, graphene offers a hexagonal basal plane of atomic lattices, which enables growth of highly-aligned, single-crystalline ZnO, GaN, or InAs nanostructures without using expensive, bulk single crystal substrates.[15-17] These superior properties enables the preparation of position- and morphology-controlled 1D nanomaterial arrays on graphene substrates.[9,18] Facile lift-off of semiconductor/graphene heterostructures also enabled the fabrication of high-quality inorganic semiconductors in ultrathin and flexible forms that are suitable for wearable and implantable device applications. Methods for making individually addressable semiconductor nanoarchitectures on graphene films and newly developed fabrication techniques for ultrathin, high-density nanodevices on graphene are presented.

In addition to the integrated 1D nanorod devices on graphene substrates, microstructural GaN light-emitting diodes (LEDs) for microdisplay applications are presented in this thesis. An individually addressable form of GaN microdisk LEDs on graphene dots was fabricated for high-spatial-resolution microdisplay applications. Furthermore, for full-color LED display applications, multicolor light-emitters based on multifaceted microstructural LEDs were investigated. For multifaceted LEDs, by precisely controlling the morphology of the GaN microstructures, the chemical composition of $In_xGa_{1-x}N$ quantum wells on each microfacet could be varied, thereby tuning the emission color.

1.3. Outline

This dissertation consists of six parts. A general introduction is provided in Chapter 1. Chapter 2 reviews 1D semiconductor nanomaterial-based nanodevices for high-density device applications. This chapter also reviews recent research activities concerning optoelectronic devices made of inorganic semiconductors grown on graphene. Additionally, many different approaches to making ultrathin and flexible devices are discussed in this chapter. Chapter 3 describes the experimental set-ups and procedures, including growth, device fabrication and characterization methods. Chapter 4 presents the ultrathin and individually addressable nanorod device arrays on graphene substrates. In this chapter, integrated ZnO nanorod devices on graphene are discussed and the extreme flexibility of the devices is demonstrated. Furthermore, the variation observed in device characteristics of individual nanorod devices are presented. This chapter also reviews their applications as photodetector and pressure-sensor arrays. Light-emitting diode applications of coaxial GaN/ZnO nanorod heterostructure-based devices are presented at the end of this chapter. Metal-cored nitride microtube structures are discussed, which can significantly improve nanostructured LED performance by improving the current-spreading characteristics. GaN/ZnO nanorod arrays grown on large-area graphene are also presented for transferable and flexible device applications. Chapter 5 presents microstructural nitride semiconductor LEDs on graphene substrates for microdisplay applications. Ultrathin and individually addressable GaN microdisk LEDs on graphene dots are presented for microdisplay applications. Additionally, variable-color GaN microdonut-shaped and micropyramidal LED arrays were fabricated for full-color microdisplay. Chapter 6 summarizes the thesis and provides suggestions for future research.

There are two appendices to this dissertation. Appendix A presents the catalyst-free MBE growth of InAs nanorods and their coaxial nanorod heterostructures on graphene layers. Appendix B demonstrates the monolithic integration of wide and narrow band gap semiconductor nanorods vertically on each surface of graphene. This demonstrates that graphene can be used to combine various types of semiconductor nanostructures even those having great differences in lattice constants.

Background and literature survey

2

In this chapter, research activities on 1D semiconductor nanomaterial assembly based nanodevices are reviewed. After making an overview of nanodevices using horizontally and vertically assembled nanorods, semiconductor nanorods growth on graphene and their device application are discussed. Furthermore, general review of ultrathin and flexible devices and their applications are presented. Moreover, current status and issues are also discussed for each device applications.

2.1. Nanodevices made of 1D semiconductor nanomaterials assembly

2.1.1. Horizontally assembled 1D nanomaterial-based devices

In the early stage of 1D semiconductor nanomaterials research, nanorod devices were usually fabricated by dispersing the nanorods on insulating surface of the substrate and making metal contacts on the nanorods. This approach successfully demonstrated many novel nanorod based devices.[19, 20] Furthermore, by forming axial and coaxial heterostructures on nanorods, even more sophisticated electronic and optoelectronic nanorod devices were demonstrated.[7, 21] With the effective demonstration of single nanorod devices, many scientiests prospected the possibility of making high-density devices based on controlled assembly of nanorods. For this reason, aligned dispersion methods of nanorods were developed to assemble nanorods horizontally on the substrates in a controlled manner.

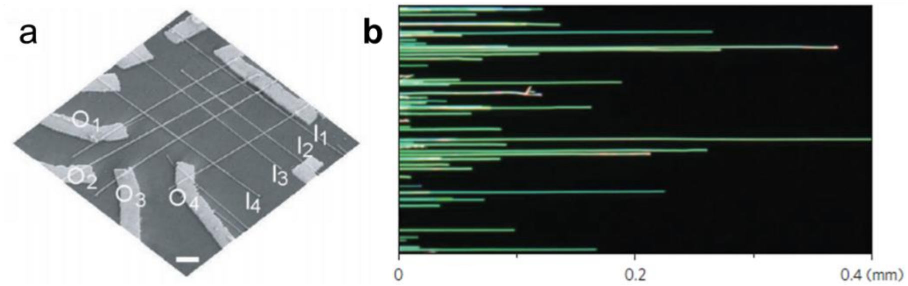

Figure 2.1. Horizontally assembled nanowires using (a) fluid-directed assembly technique[22] **and (b) nanocombining assembly technique in which nanowires are anchored to defined area.**[23]

For example, Liber *et al.* developed various nanowire assembly techniques such as fluid-directed and nanocombining assembly techniques, as shown in Figure 2.1.[22] Figure 2.1(a) shows nanowire crossbar arrays assembled by fluid-directed methods. Si/SiO_2 core-shell nanowires were used for this device, where oxide shells with controlled thickness served as gate dielectric. Each crossbar junction worked as nanowire field effect transistors (FET) and nanoscale addressable decoder was successfully demonstrated.

More recently, for the large scale assembly of highly aligned nanowires, nanoscale combining technique was developed.[23] This method works by precisely controlling the alignment force by defining anchoring and combining region on the target substrate, thereby one end of the nanowire is anchored on the anchoring region and become aligned on the combining region. The nanocombining assembly technique yielded highly aligned arrays where 98.5% of the nanowires were aligned to within ±1°.

Although these nanowire assembly methods successfully demonstrated that nanowire based nanoscale devices can actually work for integrated nanosystems, still the reproducibility of the nanodevices cannot be ensured because the position and dimension of nanowires cannot be precisely controlled.

2.1.2. Vertically aligned 1D nanomaterial-based devices

One of the most efficient way to assemble high-density of aligned nanorods would be the vertically aligned growth method of nanorods on the substrate.[24] As shown in the tilted and cross-sectional SEM images in Figure 2.2(a), the vertically aligned nanorods can be packed in very high density.[25] Using these high density of *n*-GaN/ZnO coaxial nanorods grown on *p*-GaN coated *c*-Al_2O_3 substrates, near ultraviolet (UV) LED was demonstrated.

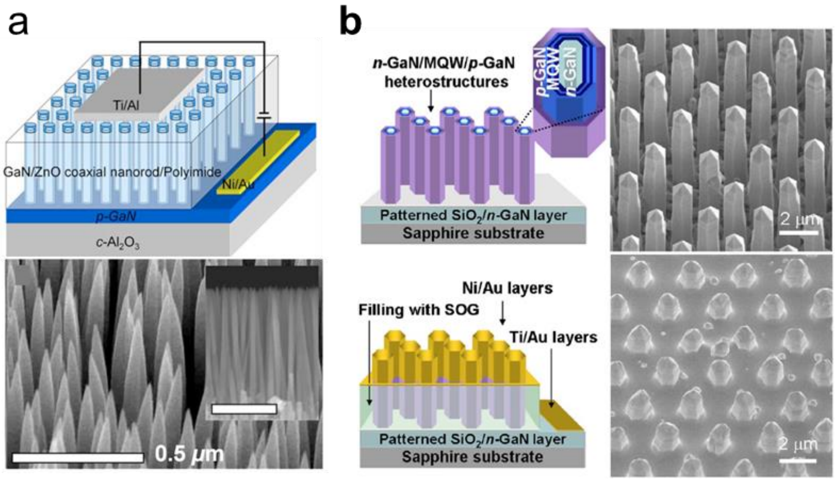

Figure 2.2. Vertically assembled nanowire crossbar array. (a) Randomly nucleated *n*-GaN/ZnO nanorods vertically grown on *p*-GaN substrates.[25] (b) Position- and dimension-controlled GaN/$In_xGa_{1-x}N$/GaN/ZnO nanorod arrays and LED applications.[26]

More recently, position- and dimension-controlled growth of vertical nanorod arrays were developed using the hole patterned growth mask.[27] By employing the growth mask, semiconductor nanorods can be selectively nucleated and grown on the exposed hole patterned region. Since the diameter and density of the nanorods can be controlled by the hole pattern diameter and spacing, the growth rate as well as the final length of the nanorods can be uniform. The regular arrays of nanorods can have many advantages over randomly grown nanorods. When growing axial or coaxial nanorod heterostructures, the chemical composition and doping concentration of the layers on each nanorod can be uniform, thereby the reliability and the performance of the nanorod devices can be further improved.[26] More importantly, the position- and dimension-controlled nanorod arrays can be potentially used for high density integrated device applications. Figure 2.2(b) shows the position- and dimension-controlled GaN/$In_xGa_{1-x}N$/GaN/ZnO coaxial nanorod hetrostructure LED arrays.[26] In this work, vertical nanorods with highly controlled diameter, height, and spacing were fabricated and precisely controlled $In_xGa_{1-x}N$/GaN multiple quantum well (MQW) layers, which determine the emission color, were also made. Using these elaboratately controlled nanorod arrays, nanoarchitecture LED microarray was succesfully demonstrated.

In addition to the controlled growth issue of nanorod arrays, it is very important to fabricate devices which can electrically address nanorods in the arrays for high-density device applications. As shown in Figure 2.3(a), Z. L. Wang *et al.* demonstrated addressable nanowires device using low-temperature hydrothermal synthesis of vertical ZnO nanorods on electrode lines pre-patterned plastic substrates.[28] The crossbar array structure was fabricated by making multiple top electrode lines on ZnO nanorods. In each crossbar junction, bundles of *c*-axis aligned vertical ZnO nanorods worked as a pressure sensor utilizing the piezoelectric properties of ZnO. This addressable nanorod device succesfully demonstrated flexible and transparent high-spatial-resolution tactile imaging sensor.

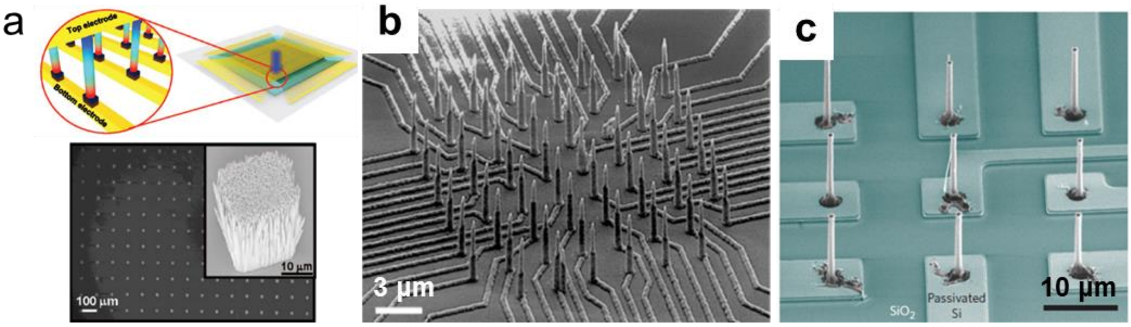

Figure 2.3. Addressable array of bundles of ZnO nanorods for piezoelectric pressure imaging sensor.[28] Individually addressable nanorods made by top down[29] and bottom up[30] approaches. Scale bars are 3 and 10 µm, respectively.

Individually addressable nanorod array device would potentially enable the fabrication of ultimate density device with rich functionalities, since the diameter of the nanorod can be scaled down as small as a few nanometers[31, 32] and many functionalities can be integrated in a single nanorod by making elaborate axial and coaxial heterostructures.[33] For these reason, both top-down[29] and bottom-up[30] approaches were used to make individually addressable nanorod arrays, as shown in Figures 2.3(b) and (c).

High-density individually addressable Si nanorod arrays were fabricated by top-down approach, as shown in Figure 2.3(b). To make this device, Si wafer was bonded to electrode pre-pattern substrate by nickel silicidation. Then, Ni dots were formed on the Si wafer in an aligned manner with the underlying electrodes and nanorods were formed by dry etching. This nanorod device arrays, which have superior spatial resolution and ideal geometry for interacting with cells, were used to record the intracellular activity of neurons.

Nanomaterials directly grown on certain spots on the substrate, which is called as bottom-up approach, can have higher material qualities than those prepared by top-down approach which usually involves thin film growth (or wafer bonding), multiple lithography and etching processes. The individually addressable nanorods prepared by bottom-up approach was recently demonstrated as shown in Figure 2.3(c).[30] The silicon-on-insulator (SOI) substrate was patterned in line shape and one Au dot were formed on each Si line. Then single Si nanorod was grown vertically on each Si line by vapor-liquid-solid (VLS) growth method. Electrolyte was filled on the nanowires and platinum wire was used as the counter electrode. Using this set-up, the photoelectrochemical measurement of single nanowire/electrolyte inteface was carried out.

Although this method worked fine to measure the signals from individual nanorods prepared by bottom-up growth approach, this method has several limitations as listed below. First, the material choice is strictly limited because we need to consider the nanomaterials should have growth compatibility, such as growth temperature and epitaxial relation, with the pre-patterned electrode lines. Secondly, the number of Si line patterns should be increased proportional to the number of Si nanorods, so it becomes extremely challenging to increase the number of nanorod devices while keeping nanorod device arrays in high density. For scalable approach, rather than making electrodes for each nanorod, crossbar type electrode design is desirable. These obstacles can be overcome basically using inorganic nanomaterials grown on graphene films, which can offer vertically aligned growth of various kinds of semiconductor nanorods and exhibit high temperature compatibility and good mechanical flexibility.[10, 16]

2.2. Semiconductor nanostructure devices on graphene substrates

After the first discovery that ZnO nanomaterials can be grown heteroepitaxially and vertically on graphene films,[15] growth of many different semiconductor nanomaterials, including ZnO, GaN, InAs, GaAs, and *etc.*, on graphene substrates were demonstrated.[34-36] The graphene substrates can be an excellent substrate for semiconductor growth, since graphene has great scalability and extremely thin layered hexagonal lattice structure of graphene can provide heteroepitaxial relation to the semiconductor crystals. [36] Additionally, graphene have high thermal stability at high temperature required for inorganic semiconductor growth. The excellent electrical and thermal conductivity of graphene can also be used for ultrathin electrodes as well as heat dissipation layers for semiconductor devices.[13] Moreover, the inorganic semiconductors prepared on large-area graphene can be easily lifted-off from the substrate due to their layered structure and weak bonding strength with the substrate.[16] These interesting characteristics make inorganic semiconductors/graphene hybrid heterostructures as a unique and novel material system for transferable and flexible device applications.

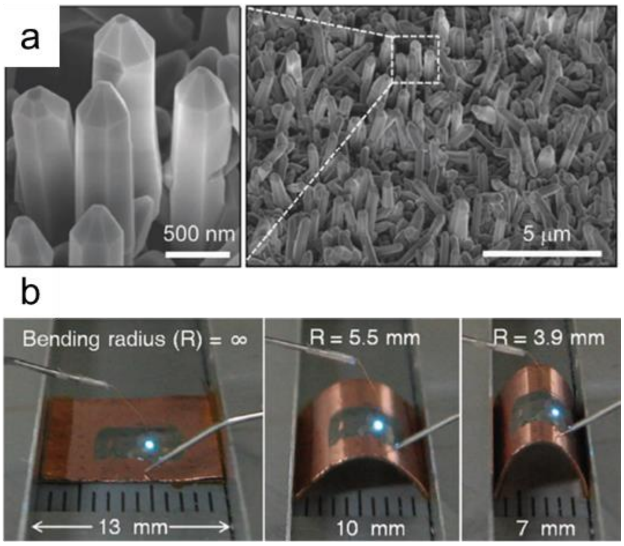

Figure 2.4. (a) Tilted SEM images of GaN/ZnO nanorods grown on CVD graphene layers. (b) Flexible inorganic LED using nanorods grown on graphene layers.[10]

Flexible inorganic LED was demonstrated using semiconductor nanorods grown on graphene layers, as shown in Figure 2.4.[10] To make the flexible LED, ZnO nanorods were grown on large-area, chemical vapor deposited (CVD) graphene layers. Although ZnO nanorods are known to grow vertically on exfoliated graphene layers, the quality of CVD graphene layers were not optimized and ZnO nanorods grown on CVD graphene layers were grown in many different directions other than the vertical direction. In more recent growth study, it is well demonstrated that perfectly aligned vertical ZnO nanorod arrays can be grown on large-area CVD graphene layers. After preparing the ZnO nanorods on graphene layers, GaN coaxial layer was heteroepitaxially coated on ZnO nanorods for blue LED application. Then, *p*-GaN, $In_xGa_{1-x}N$/GaN multiple quantum well, and *n*-GaN layers were heteroepitaxially grown on the surface of the GaN nanorods. The surface morphology of GaN/ZnO nanorod LED structures grown on graphene layers can be seen in the tilted SEM images in Figure 2.4(a). Flexible LED was fabricated by coating the nanorod/graphene hybrid heterostructures with polymer layers and lifting off these layers by wet chemical etching of the underlying SiO_2 layers by buffered oxide etchant (BOE). Then, these layers were transferred on copper (Cu) foil and ohmic metal contact was formed on the top surface of the nanorods. As shown in Figure 2.4(b), the flexible inorganic LED device showed blue light emission and worked reliably under various bending radius (see Figure 2.4(b)).

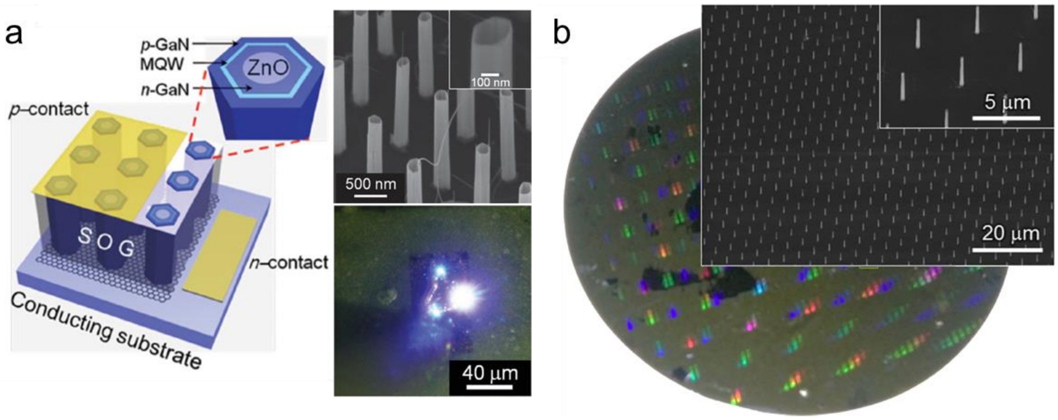

Figure 2.5. Position- and dimension-controlled nanorods on graphene substrates. (a) Schematic illustration of GaN/ZnO nanorod LEDs on exfoliated graphene layers, SEM image of ZnO nanorod arrays on exfoliated graphene layers, and light-emission image of the LED.[18] (b) 2-inch wafer scale grown ZnO nanorod arrays on CVD graphene layers.[9]

Position- and morphology-controlled nanorod array growth on graphene substrates was recently demonstrated to fabricate high-density nanorod devices that have better uniformity and reliability. Figure 2.5(a) shows SEM image of the position- and morphology-controlled ZnO nanorod arrays grown on exfoliated graphene layers.[18] The ZnO nanorods were grown selectively on exfoliated graphene layers by artificially making step edges by oxygen plasma ashing. Then GaN LED structures were heteroepitaxially coated on ZnO nanorods and LED device was made by making ohmic metal contact on *p*-GaN and underlying graphene layers as schematically shown in Figure 2.5(a). The device showed bright blue color emission as shown in Figure 2.5(a).

More recently, position- and morphology-controlled growth of ZnO nanorod arrays on large-area CVD graphene substrates were demonstrated as shown in Figure 2.5(b).[9] In this work, hole patterned SiO_2 growth mask was made on CVD graphene layers, where the surface of graphene layers was only exposed on the holes. ZnO only nucleated and grew on the graphene surface exposed by the hole patterns, so that ZnO nanorod arrays were prepared on 2-inch wafer scale CVD graphene layers. Since there are no practical limitation in production size of graphene layers, which can even be synthesized by roll-to-roll process, the ZnO nanorod arrays on graphene layers can also be prepared in much larger size. In this thesis, this novel material system was used to fabricate individually addressable nanorod devices that were ultrathin and flexible.

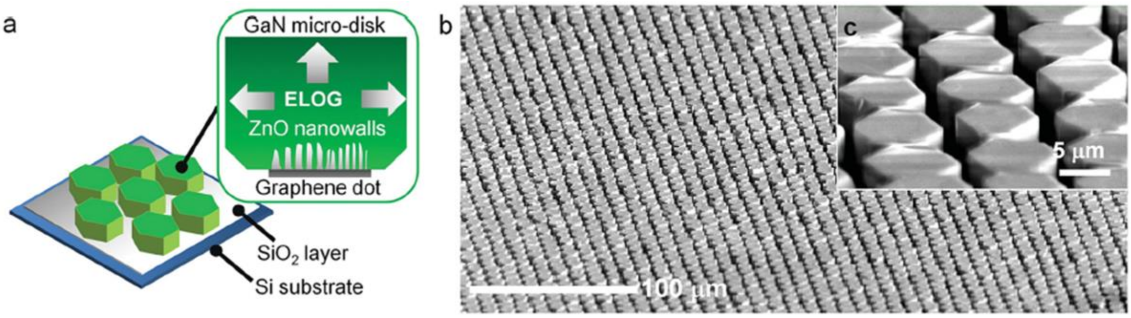

Figure 2.6. (a) Schematic illustration of the structure and ELOG growth of GaN microdisks on graphene dots. Tilted SEM images of GaN microdisk arrays growth on graphene dots at (b) lower and (c) higher magnifications.[37]

In addition to nanostructures grown on graphene substrates, semiconductor microstructures, such as microdisks and microrods, were also prepared on graphene layers for transferable and flexible device applications. Figure 2.6 shows the GaN microdisk LED arrays grown on ZnO nanowalls coated graphene dots.[37] High quality, single crystalline GaN microdisks were obtained using epitaxial lateral overgrowth (ELOG) technique, as schematically shown in Figure 2.6(a). The resulting structure is shown in the tilted SEM images in Figures 2.6(b) and (c), where regular arrays of GaN hexagonal microdisks with clear facets can be seen. Flexible LEDs with bright blue emission were made using this structure and the *c*-plane of GaN microdisks was used as a dominant light-emitting surface. In this thesis, this novel microdisk LED on graphene dots structure was used to make ultrathin and flexible GaN microdisk microdisplay on graphene substrates.

2.3. Ultrathin and flexible devices

Ultrathin, flexible nanodevices with high density, performance, and reliability are in high demand for wearable and implantable device applications. For the ultrathin bendable devices, organic films due to their excellent scalability and flexibility have widely been employed. Someya *et al.* demonstrated ultrathin and ultraflexible organic photonic skin (see Figure 2.7).[38] As shown in Figure 2.7(a), even with the multiple stack of layers, including substrates, electrodes, organic LED structures, and passivation layers, the total thickness of the device was as thin as 3 μm and display device was demonstrated on skin (see Figure 2.7(b)).

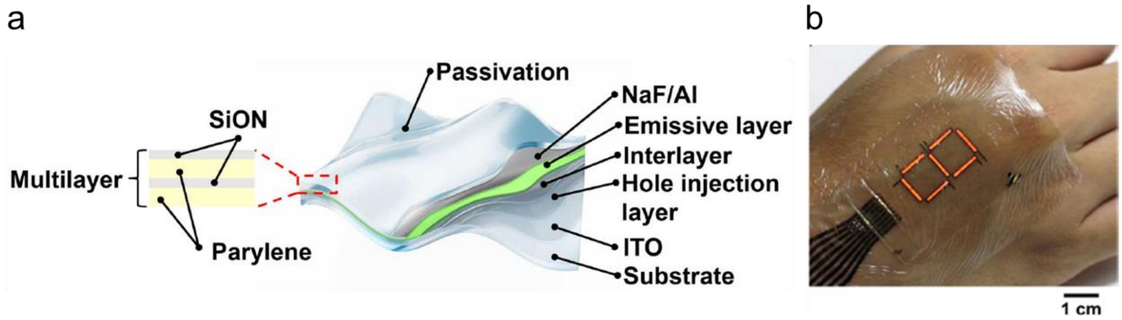

Figure 2.7. Ultrathin and flexible photonic skin fabricated with organic materials. (a) Schematic illustration of the device structure. (b) Demonstration of ultrathin organic LEDs on skin.[38]

Meanwhile, higher device performance is expected when using inorganic semiconductors in terms of high-carrier mobility, long-term stability, and reliability. Accordingly, flexible devices based on inorganic semiconducting materials have been extensively studied with the development of elaborate fabrication techniques, including epitaxial lift-off and micro-assembly. Rogers *et al.* demonstrated flexible display device by the epitaxial lift-off AlGaAs/GaAs LEDs from the substrate and assembled them on PET substrates, as shown in Figure 2.8(a).[39] The magnified photographs in Figure 2.8(b) shows the discrete arrays of AlGaAs/GaAs LED pieces integrated on flexible PET substrates.

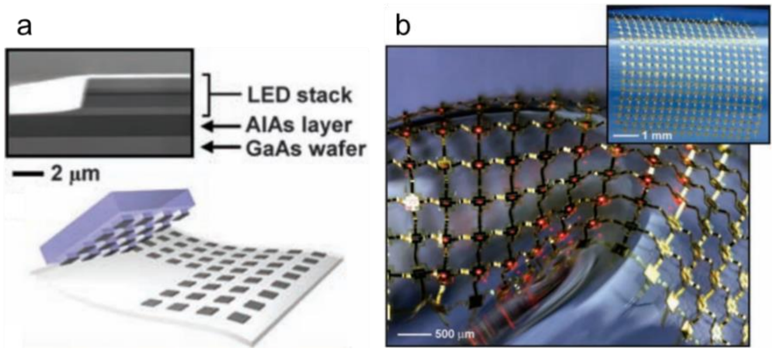

Figure 2.8. Flexible display using inorganic semiconductors. (a) Schematics of the fabrication method. Epitaxial lift-off of AlGaAs/GaAs LEDs from the substrate and assembly on PET substrate. (b) Magnified photograph of the inorganic LED display.[39]

Recently, to further increase the integration density of flexible inorganic devices, vertical inorganic nanomaterials have been suggested, which can have potential advantages over planar thin films due to their unique physical properties and high growth density. Using this approach, high-spatial-resolution tactile sensor arrays were fabricated using ZnO nanorods as schematically shown in Figure 2.3(a).[28] The piezoelectric characteristics of bundles of ZnO nanorods vertically aligned in *c*-axis were used to detect external pressure applied on the device. However, individual addressing of each nanorod in arrays would be an essential step to realize ultimate density device. However, up until now, flexible and individually addressable vertical nanorod devices has not been realized yet because of the difficulties in preparing position- and morphology-controlled nanorod arrays and problems in lifting-off the nanorod arrays from the substrate. These obstacles can be overcome basically using 1D semiconductor nanostructures grown on 2D nanomaterials. This dissertation will show the fabrication and characteristics of ultrathin and flexible individually addressable nanorod devices array based on 1D+2D hybrid dimensional nanomaterials.

Experimental methods

3

This chapter describes experimental methods and apparatus to fabricate individually addressable hybrid dimensional nanoarchitecture devices using semiconductor nanostructures grown on graphene substrates. The hybrid dimensional materials were prepared using selective-area MOCVD system and catalyst-free MBE for the growth of ZnO, GaN, and InAs nano- and micro-structures on graphene layers. Methods of fabricating individually addressable nanorod devices using 1D+2D hybrid dimensional nanomaterials will be presented in detail. Additionally, the characterization methods of high-density integrated nanorod device arrays, photodetectors, pressure sensors, and nanostructured LEDs will be described in detail.

3.1. Growth of semiconductor nanostructures on graphene substrates

3.1.1. Preparation of graphene substrates

Large-area, multilayer graphene (MLG) were synthesized on copper (Cu) foil using the CVD method. The Cu foil was inserted into a quartz tube and heated to 980 ◦C with an H_2 flow at 100 standard cubic centimeters per minute (SCCM) at 200 Torr. Graphene films were grown on the Cu foil for 90 min under a mixture of CH_4 and H_2 at flow rates of 10 and 100 SCCM, respectively. During growth, the reactor pressure was maintained at 220 Torr. Finally, the sample was cooled to room temperature (RT) under flowing H_2 at a pressure of 200 Torr.

3.1.2. Selective-area metal-organic vapor-phase epitaxy of ZnO and GaN semiconductors

- *ZnO nanorod arrays on graphene layers*

The ZnO nanorod arrays were grown on CVD graphene layers using selective-area metal−organic vapor-phase epitaxy (SA-MOVPE), as shown in Figure 3.1. To obtain selective growth on the substrate, graphene substrates were coated with a 50 nm amorphous SiO_2 masking layer with hole patterns. 50-nm-thick SiO_2 growth mask was deposited by plasma-enhanced chemical vapor deposition (PECVD) system installed at the Inter-university Semiconductor Research Center (ISRC) at Seoul National University. Hole patterns were formed on the growth mask by *e*-beam lithography (EBL) patterning followed by dry and wet etching using CF_4 reactive ion etching (RIE) and BOE.[9]

After making the growth mask, SA-MOVPE growth was performed using Diethylzinc (DEZn) and high-purity O_2 (>99.9999%) as reactants, and high-purity Ar (>99.9999%) as the carrier gas. The flow rates of DEZn and O_2 were 20 and 40 SCCM, respectively. During growth, Ar flowed into the quartz reactor through the bubbler with a DEZn bubbler temperature of −15◦C. To prevent premature reaction, the O_2 gas line was separated from the main gas manifold line. The reactor pressure was kept at 0.3 Torr during growth, and the temperature ranged from 600 to 700 ◦C.

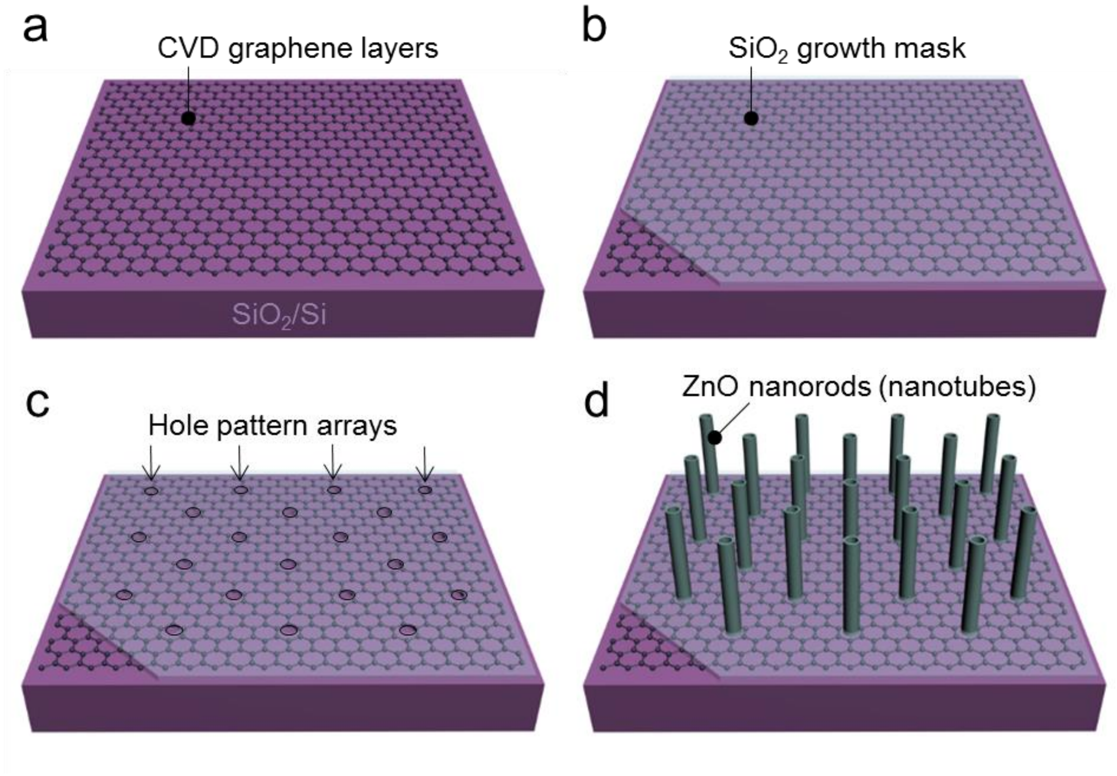

Figure 3.1. Preparation method of ZnO nanorod arrays on CVD graphene layers. (a) Transfer of CVD graphene layers on SiO_2/Si substrate followed by (b) SiO_2 growth mask deposition and (c) hole array patterning on SiO_2 growth mask. (d) ZnO nanorod arrays growth by SA-MOVPE.

- *GaN/ZnO microtube arrays*

After preparing the ZnO microtube arrays on CVD graphene layers or *n*-GaN/*c*-Al_2O_3, a thin layer of Si-doped *n*-GaN was then heteroepitaxially grown on the ZnO microtube arrays. The bottom parts of the *n*-GaN/ZnO microtubes were masked with a 50 nm SiO_2 layer. First, the entire surface of the microtube array was coated with a SiO_2 layer by magnetron sputtering deposition, and then BOE was used to etch the SiO_2 and expose the top GaN surface of the microtubes using a 1 μm thick poly(methyl methacrylate) (PMMA) layer which masked the lower parts of the microtubes. This PMMA layer was prepared by a spin-coating method first to coat the entire surface of the microtubes and then using oxygen plasma ashing to etch the PMMA layer from the top parts of the microtubes. After the lower parts of the *n*-GaN/ZnO microtubes were masked with the SiO_2 layer, the *n*-GaN/ZnO microtubes were then heteroepitaxially coated with Mg-doped *p*-GaN, *u*-$In_xGa_{1-x}N$/*u*-GaN MQWs, and Si-doped *n*-GaN layers. Finally, the Mg acceptors in the *p*-type layers of the microtubes were activated by rapid annealing at 650 ℃ for 5 min in a N_2 atmosphere.[40]

- *GaN microdisk arrays on graphene dots*

For the epitaxial lateral overgrowth (ELOG) of the GaN microdisks, continuous graphene films were patterned to graphene microdot arrays by photolithography and O_2 plasma dry etching. *c*-axis aligned ZnO nanowalls were first grown on graphene microdots using MOVPE and the GaN microdisk structure was produced using ELOG of GaN on ZnO covered graphene dots using a pulsed-mode MOCVD technique. After growing the GaN microdisks, an additional Mg-doped *p*-GaN, *u*-$In_xGa_{1-x}N$/*u*-GaN MQWs, and Si-doped *n*-GaN layers was regrown on the microdisks.[37]

- *GaN microdonut arrays*

The *n*-GaN microdonut arrays were prepared on Si-doped *n*-GaN/Al_2O_3(0001) using selective-area metal-organic vapor-phase epitaxy, as shown in Figure 3.2. For selective growth, a 100-nm-thick amorphous Si_3N_4 mask layer with hexagonal ring patterns was prepared on an *n*-GaN/Al_2O_3(0001) substrate by plasma-enhanced chemical vapor deposition (PECVD; HIGH-DEP BMR) and *e*-beam lithographic patterning (EBL; JEOL JSM 6510 – Raith GmbH ELPHY Quantum). After preparing the *n*-GaN microdonut arrays, Mg-doped *p*-GaN and electron-blocking *p*-$Al_xGa_{1-x}N$, *u*-GaN, and *u*-$In_xGa_{1-x}N$ layers were heteroepitaxially grown on the entire surface of the *n*-GaN microdonuts at 1000, 1100, 1000, 800, and 1100℃, respectively.

Trimethylgallium, trimethylaluminum, trimethylindium, ammonia, bis(methylcyclopentadienyl)magnesium, and disilane were used as Ga, Al, In, N, Mg, and Si sources, respectively. After growth, the films were rapidly annealed at 650℃ for 5 min in a N_2 atmosphere to activate Mg acceptors in the *p*-type layers.[3]

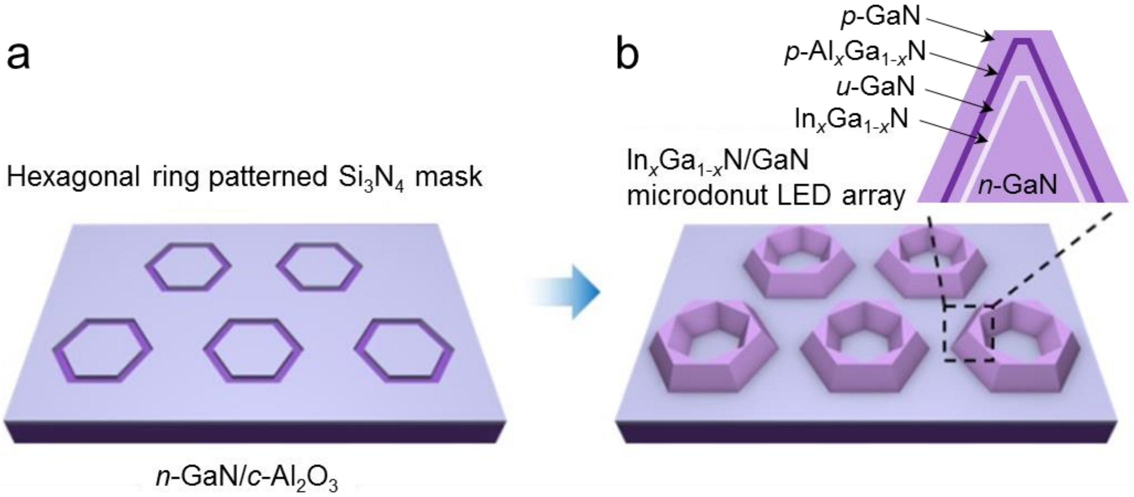

Figure 3.2. Preparation method of GaN microdonuts on *c*-sapphire substrate. (a) Hexagonal ring patterning of Si_3N_4 growth mask. (b) GaN microdonut growth by SA-MOVPE and LED structure coating including *p*−*n* junction, multiple quantum well and electron blocking layers.

3.1.3. Catalyst-free molecular beam epitaxy of $In_xGa_{1-x}As$/InAs coaxial nanorod heterostructures on graphene layers

For the catalyst-free molecular beam epitaxial growth of $In_xGa_{1-x}As$/InAs coaxial nanorod heterostructures on graphene layers, a two-step MBE process was used: (i) high-temperature synthesis of ultrafine-core InAs nanorods, and (ii) subsequent low-temperature coating of $In_xGa_{1-x}As$ shell layers on the InAs core nanorods. This two-step MBE growth method was employed to produce $In_xGa_{1-x}As$ shell layers with precisely controlled chemical composition and thickness, which resulted in highly controlled nanorod heterostructures with clean interface compared to spontaneous phase separated MOCVD grown InAs core and $In_xGa_{1-x}As$ shell nanowires.[41] Inside of a cryogenically cooled UHV growth chamber (RIBER 32P), InAs nanorods were grown at 530°C for 1 h, by supplying high-purity indium (In) and uncracked arsenic (As_4) molecular beams from Knudsen cells. (see Figure 3.3) The beam-equivalent pressures (BEPs) of In and As_4 were 6×10^{-8} and 7×10^{-5} Torr, respectively. For catalyst-free growth of InAs nanorods, we supplied As_4 to the substrates for 10 min before supplying In to prevent In droplet formation on the graphene layers, which resulted in quite different nucleation and crystal growth behavior from vapor–liquid–solid (VLS) growth.[36, 42]

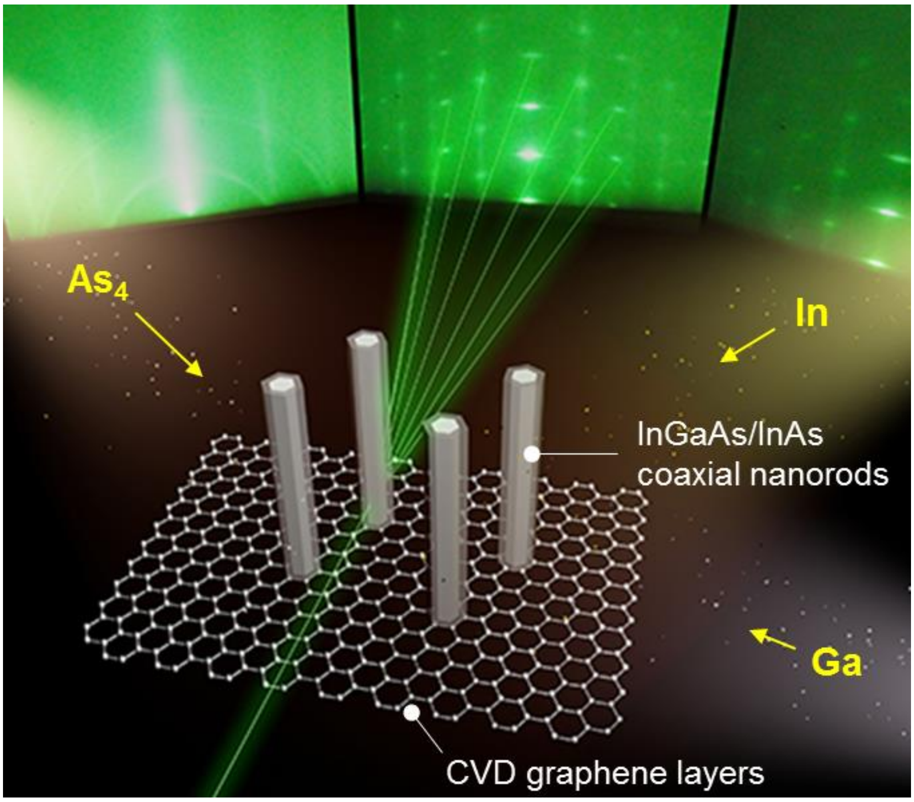

Figure 3.3. Preparation method of $In_xGa_{1-x}As$/InAs coaxial nanorod heterostructures on graphene layers.

3.2. Fabrication of ultrathin and individually addressable nanorod device arrays

3.2.1. Preparation of ultrathin layers composed of nanorod arrays on graphene layers

After preparing the ZnO nanorod arrays on CVD graphene layers, 3-μm-thick polyimide (PI) layers were formed on the sample by spin coating and the PI layers were prebaked at 120°C. The tips of the ZnO nanorods were exposed to air by selectively etching polyimide layers by 1 μm using oxygen plasma treatment. Then, the entire layers were mechanically lifted-off from the substrate (see Figure 3.4). After these freestanding layers composed of ZnO nanorods/graphene layers embedded in PI layers were prepared, the nanostructure-embedded layers were cured in N_2 atmosphere at 300°C.

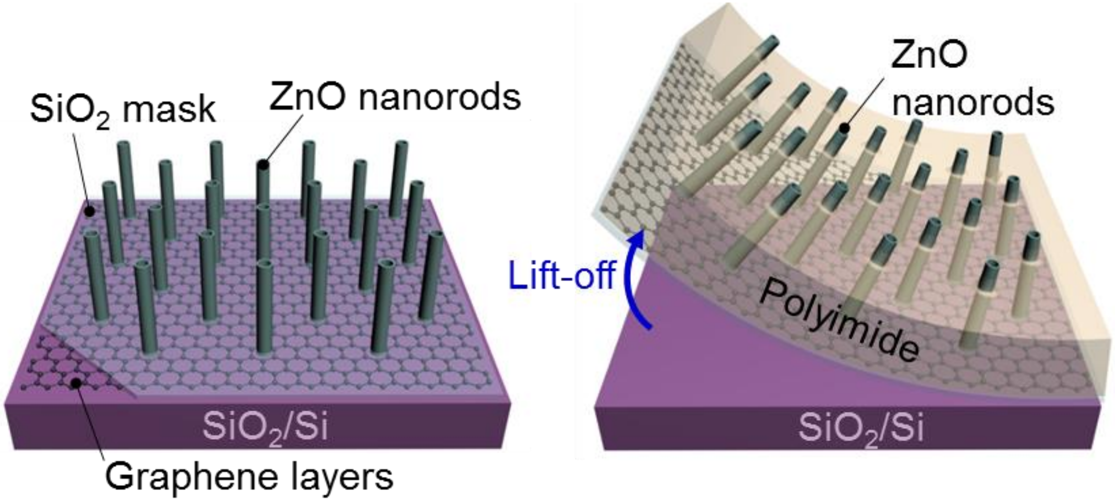

Figure 3.4. Lift-off of ultrathin layers composed of ZnO nanorod arrays on graphene layers from the substrate.

3.2.2. Microelectrodes formation on ultrathin layers

To form microelectrodes on the ultrathin and flexible layers, the ultrathin layers were transferred flat on a highly doped *n*-type Si substrate surface to be prepared for electron beam lithography (EBL). PMMA layers were spin coated on the ultrathin layer and patterned by EBL. Then, gold (Au) electrode lines with 3.7 μm period as top electrode lines were formed on the ZnO nanorod arrays by standard EBL, metal deposition, and subsequent metal lift-off procedures. Grazing angle metal deposition method was used to coat Au electrodes conformally on the ZnO nanorod surface. Incident metal flux angle of 20° was used while rotating the substrate. In this configuration, when 100-nm-thick Au layers were deposited on the PI layer surface, 12-nm-thick Au can be conformally deposited on the upright sidewall of ZnO nanorods. After flipping the freestanding layers and transferring on *n*-Si substrate, bottom chromium (Cr)/Au electrodes were formed in the same manner. Then, we dry etched the graphene layers that were not covered with Cr/Au, forming electrically separated graphene layers/Cr/Au bottom electrodes (see Figure 3.5).

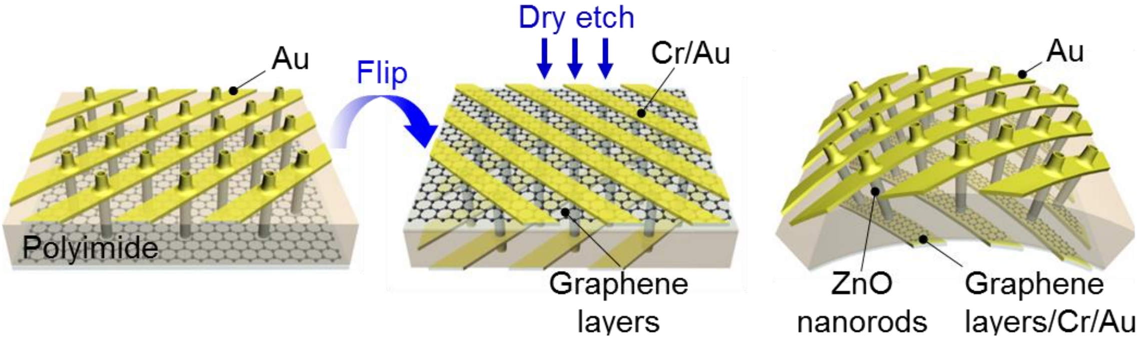

Figure 3.5. Microelectrode lines formation top and bottom surfaces of the ultrathin layers composed of ZnO nanorod arrays on graphene layers.

3.3. Fabrication of nanoarchitecture light-emitting diodes

3.3.1. GaN micropyramid and microdonut LED fabrication

Micropyramid and microdonut LEDs were fabricated by forming ohmic metal contacts on both *p*- and *n*-type GaN layers, as shown in Figure 3.6. To form ohmic metal contact to *p*-type GaN, semitransparent Ni/Au (10/10 nm) layers were deposited by thermal evaporator on *p*-GaN surface. To form *n*-contact electrodes, the underlying or *n*-GaN layer were exposed to air by removing the Si_3N_4 masking layer with buffered oxide etch (BOE), and ohmic contacts were made on the *n*-GaN. Post-annealing of the LEDs at 400℃ for 5 min in air reduced ohmic contact resistances and enhanced the device characteristics.[3]

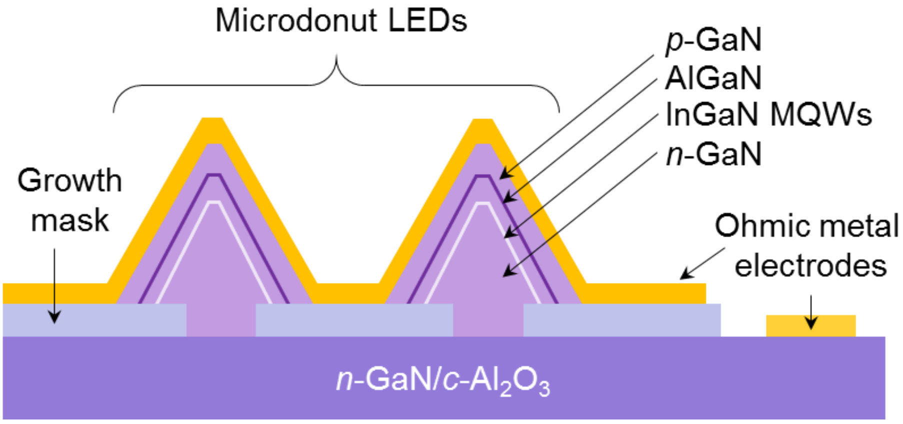

Figure 3.6. Device structure of GaN microdonut LEDs.

3.3.2. Metal-cored GaN microtube LED fabrication

Schematic illustration of the steps required to fabricate metal-cored microtube LEDs are shown in Figure 3.7. The LED devices were fabricated by making Ohmic metal contacts between the top *p*-GaN surface layers and the underlying *n*-GaN layers. The first step in making the contacts is to evaporate layers of Ti/Au (30/40 nm) onto an *n*-GaN layer. Next, the device was spin-coated with a 3 μm thick polyimide layer and cured at 300 ℃. Oxygen plasma ashing exposed the top *p*-GaN surface to air. To make the metal contacts on the *p*-GaN layer, the *p*-GaN surface was coated by deposition with semitransparent Ni/Au (10/10 nm) layers with a pad size of 50 × 50 μm^2. The metal contacts were annealed at 400 ℃ for 5 min in air to reduce the Ohmic contact resistance and enhance the device characteristics. Once we had the basic LED devices, we had to make the metal cores. The entire top surface of the device was coated with Ni/Au (10/10 nm) layers and then rapidly annealed to create Ohmic contact. Then Ag plating solution (Alfa Aesar 44067) was used to electrochemically deposit a micrometer-thick Ag layer onto the Ni/Au electrodes. To enhance the adhesion between the electroplated Ag layer and the microtube LEDs, the samples were annealed in air at 400°C for 5 min. The microtube LEDs were then immersed in BOE to obtain lift-off from the *n*-GaN/*c*-Al_2O_3 substrate and remove the underlying sacrificial ZnO layer. After the device was rinsed in deionized water, it was transferred upside-down onto a polyimide film coated with carbon tape. To make the metal cores of the microtubes, semitransparent Ti/Au (2/2 nm) layers were deposited using an *e*-beam evaporator. The flipped microtubes were coated with a 1 μm layer of ITO by RF magnetron sputter deposition with a pad size of 50 × 50 μm^2. To reduce the contact resistance of the *n*-electrodes, the samples were then annealed in air for 5 min at 300 °C.[40]

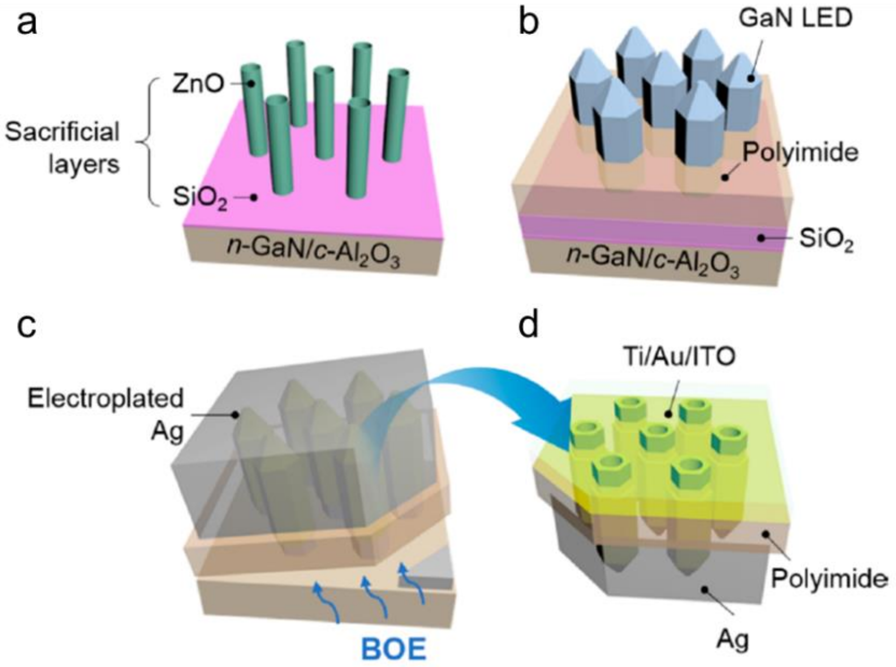

Figure 3.7. Schematic illustration of the steps required to fabricate metal-cored microtube LEDs. (a) SA-MOVPE epitaxy growth of ZnO microtube arrays on SiO_2-masked *n*-GaN/*c*-Al_2O_3 substrates. (b) Coaxial coating of the *p*-GaN layers with *u*-GaN/indium gallium nitride (*u*-$In_xGa_{1-x}N$) multiple quantum wells and *n*-GaN layers on the ZnO microtubes and formation of polyimide layers. (c) Lift-off of the GaN/$In_xGa_{1-x}N$ microtube LED array structure from the substrate after electrochemical deposition of Ag layers. (d) Deposition of the ITO/Ti/Au *n*-electrodes after upside-down transfer of the lifted-off microtube LED array structure on foreign substrates.

3.4. Fabrication of ultrathin microdisplay using GaN microdisks grown on graphene dots

3.4.1. Transfer and assembly of microdisk LEDs in ultrathin form

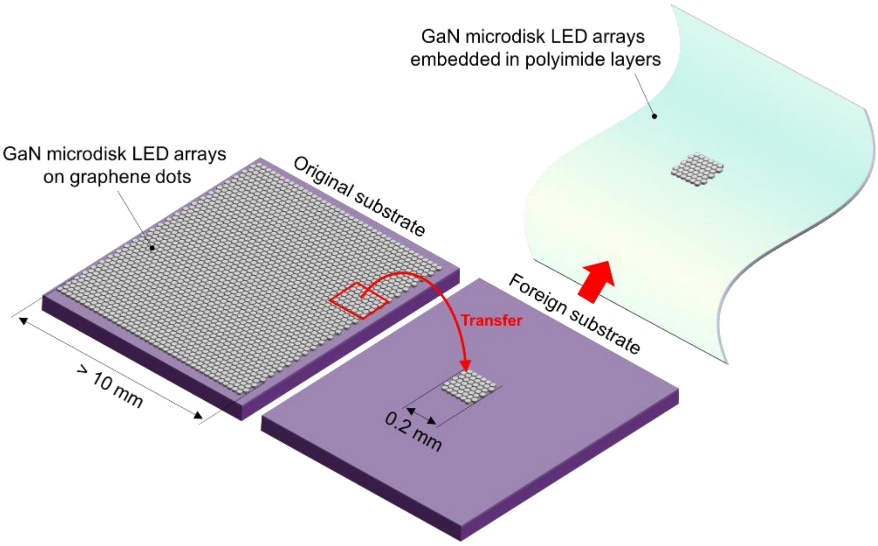

Figure 3.8. Schematic illustration of transfer process of small parts of the GaN microdisk arrays grown on graphene dots from the original substrate to foreign substrate. Then, after coating PI layer on GaN microdisk arrays, the ultrathin and freestanding layers are lifted-off from the substrate. (Figures not drawn to scale).

Large-area grown GaN microdisk LED arrays on graphene microdots were used as a starting material for the fabrication of ultrathin microdisplay. As shown in Figure 3.8, the first step was to transfer some parts of the GaN microdisk arrays from the original substrate to the foreign substrate. By transferring small pieces of microdisk arrays, which had size under 0.2 × 0.2 mm^2, for 16 by 16 microdisplay application, it is possible to obtain more than 2,000 samples from microdisk arrays grown on 10 × 10 mm^2 substrate. To transfer the discrete GaN microdisks while keeping the regularly spaced array structure, polyimide (PI) layer was spin coated on GaN microdisk arrays.

GaN microdisk arrays embedded in PI layer was chemically lifted-off by removing underlying SiO_2 layer of SiO_2/Si substrate by BOE. Then, under optical microscope, a small piece of GaN microdisk arrays in PI layer was divided and transferred on foreign substrate.

After transferring the small piece of GaN microdisk arrays on foreign SiO_2/Si substrate, 2nd PI layer was spin coated on the substrate. Then, the SiO_2 layer was removed by BOE and the ultrathin and freestanding layer composed of GaN microdisk arrays embedded in PI was prepared (see Figures 3.8 and 3.9(a)).

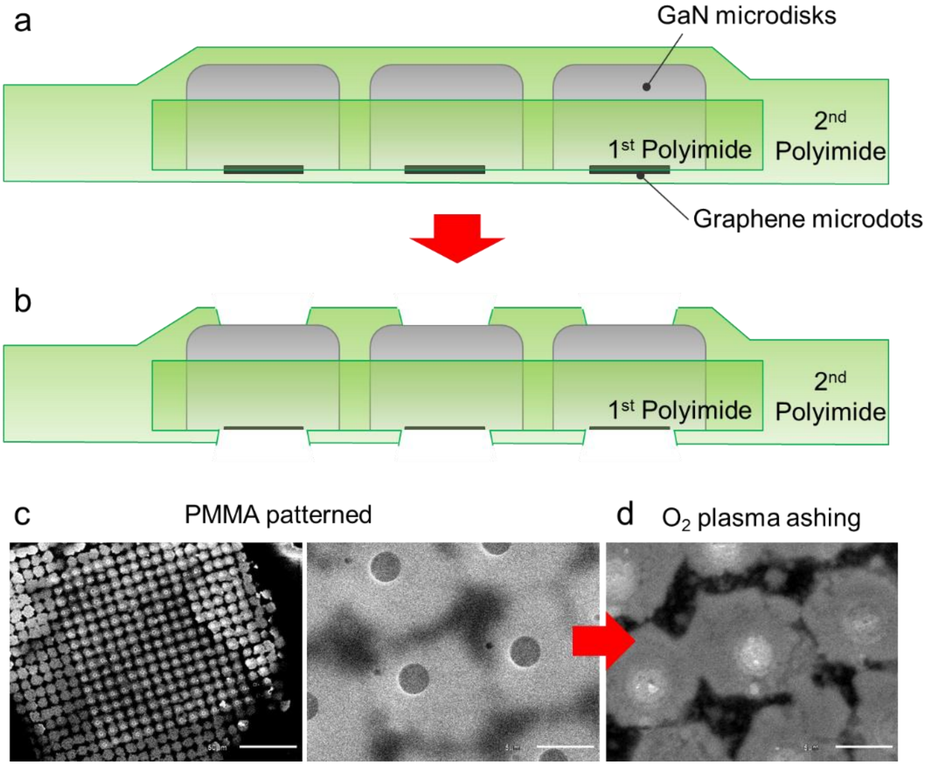

Figure 3.9. Method of exposing the *p*-GaN and underlying graphene dot surface for metallization. (a) Ultrathin layer composed of GaN microdisk arrays and (b) selectively etching PI layers to expose GaN microdisks surfaces. SEM images (c) after coating PMMA layers and patterning hole arrays and (d) after selectively etching PI layers by oxygen plasma.

The surfaces of *p*-GaN and graphene microdot were exposed to air before the metallization process by selectively etching the PI layers which covered the top and bottom surface of GaN microdisks, as shown in Figure 3.9. PMMA layers were coated on the ultrathin layers containing microdisk arrays and 3 μm diameter hole arrays were patterned in an aligned manner with the individual GaN microdisks (see Figure 3.9(c)). Then, oxygen plasma asher was used to selectively etch the PI layers through the hole patterned PMMA mask (see Figure 3.9(d)). The selective etching of PI layer was performed on both the top and bottom surfaces of the GaN microdisk LED arrays, thereby exposing the surface of *p*-GaN and graphene microdot.

3.4.2. Single walled carbon nanotubes (SWCNT) embedded metal microelectrodes

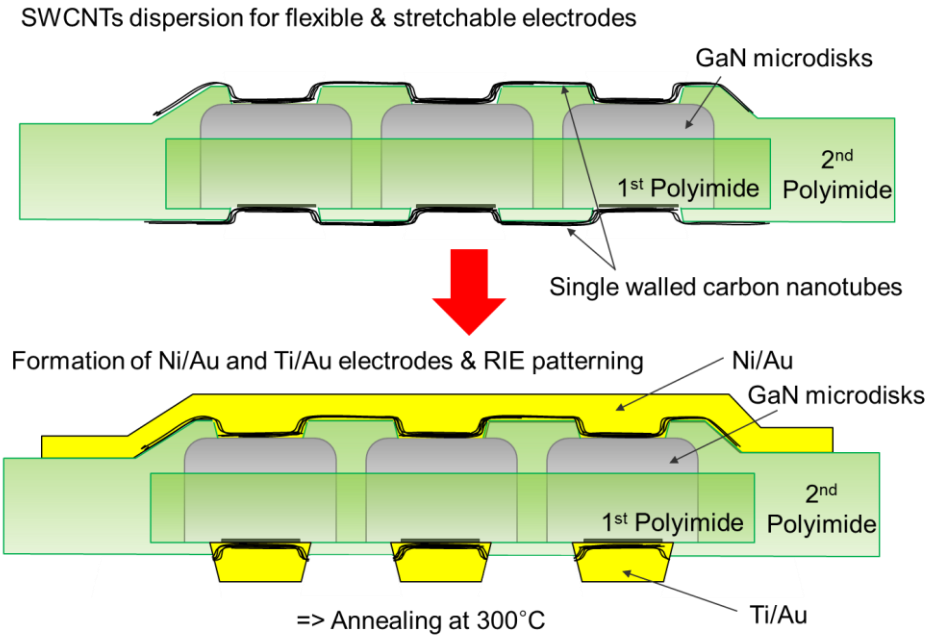

Figure 3.10. Metallization of the GaN microdisk LED arrays using single-walled carbon nanotube (SWCNT) networks embedded metal electrodes.

Single-walled carbon nanotubes (SWCNTs)/Ni/Au and SWCNTs/Ti/Au multiple electrode lines were formed on the top and bottom surface of GaN microdisk arrays in an aligned manner and crossing each other, as shown in Figure 3.10. The SWCNTs embedded metal electrodes was formed by dispersing SWCNTs on the ultrathin layer and depositing microelectrodes. Then, SWCNTs were patterned by etching SWCNTs that were not covered by metal electrodes, leaving only the SWCNTs embedded metal microelectrodes.

3.5. Electrical and optical characterization

3.5.1. Electrical characterizations of individually addressable nanorod device arrays

The current–voltage (I–V) characteristics of the devices were measured by applying a DC voltage to the device using a source meter (Keithley 2400). Two 16-channel CMOS multiplexers (ADG1406, Analog Devices) and data acquisition (DAQ, National Instruments) system were used to address each nanorod device of the 16 by 16 crossbar array.

Ideality factor and barrier height of the Schottky diodes were estimated using the following equation based on a thermionic emission theory,[43]

$$I = aA^{*}T^{2}\exp\left(\frac{-q\Phi_B}{kT}\right)\left[\exp\left(\frac{qV}{nkT}\right)-1\right],$$

where a is the contact area, A^* is the Richardson constant of ZnO, known as 32 $\mathrm{AK^{-2}cm^{-2}}$, T is temperature in Kelvin, k is the Boltzmann’s constant, q is the electric charge, n is the ideality factor and Φ_B is the barrier height.

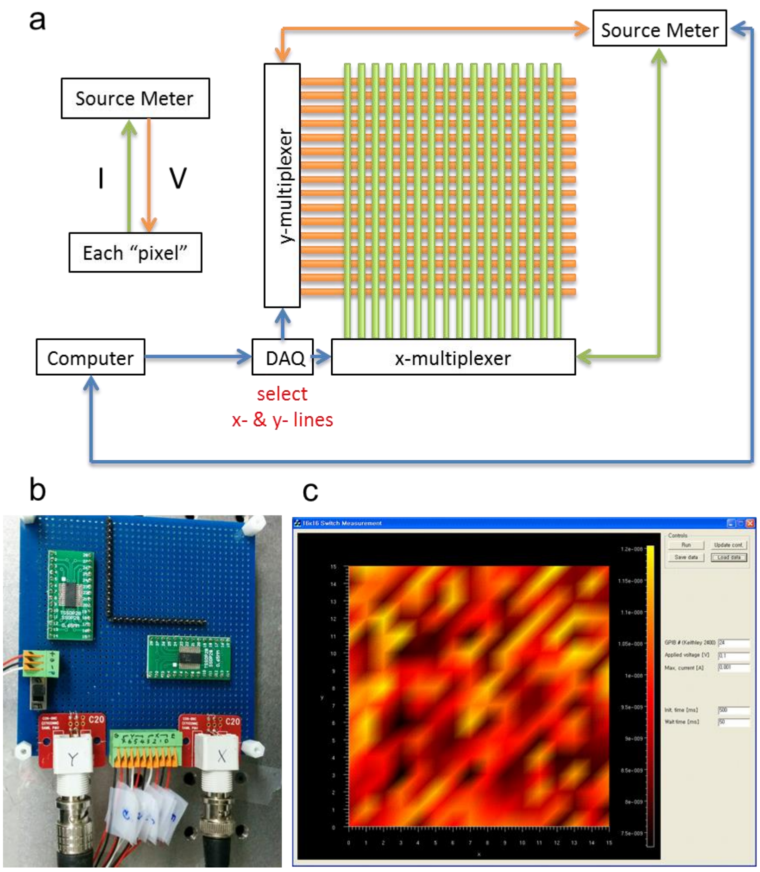

GPIB # (Keithley 2400) 24
Applied voltage [V] 0.1
Max. current [A] 0.001
Init. time [ms] 500
Wait time [ms] 50

Figure 3.11. Analog multiplexer system used to measure the addressable nanorod arrays (a) Circuit diagram of the multiplexing system. (b) Photograph of the actual measurement system on circuit board. (c) Computer program designed for measurement. (Special thanks to Dr. Hosang Yoon for developing the multiplexer system)

3.5.2. Photodetector characterizations

In the photodetection experiments, the photocurrent was measured through monitoring the change of current in response to irradiation of the UV lights with a fixed bias voltage. As a UV illumination source, 325 nm He-Cd laser was used and the continuously variable neutral density filter (NDC-50C-4M) was used to control the intensity of light illuminated on the device between 0.02 to 20 mW/cm^2. The illumination power of the 325 nm laser was measured by a UV extended Si photodetector (Thorlabs S120VC). The time-dependent photoresponses were also measured under duty-cycled on/off UV irradiation as shown in Figure 3.12.

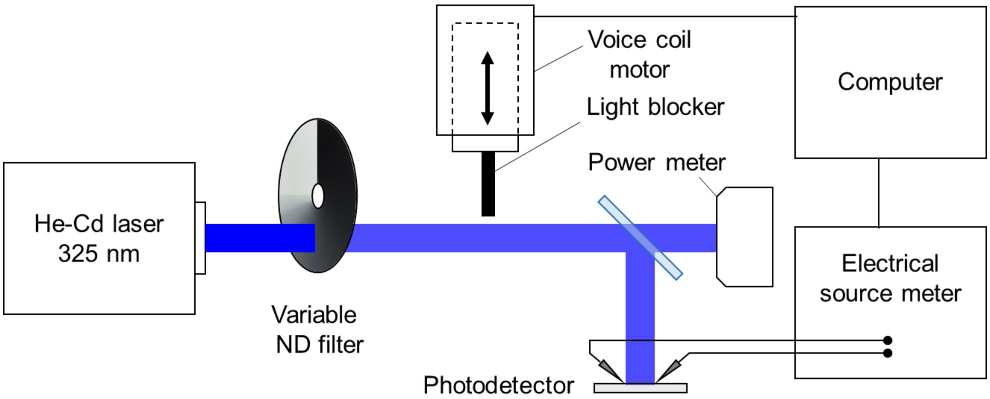

Figure 3.12. Photodetector responsivity and time response measurement system

The spectral response of the photosensor device were measured by recording the photocurrent as a function of the wavelength of the monochromatic light irradiated on the device, as schematically shown in Figure 3.13. Monochromatic light was generated by a Xenon lamp and a monochromator. Additionally, the time-dependent photoresponses of the nanodevice were obtained at a fixed bias voltage under duty-cycled on/off (30/30 s) UV irradiation.

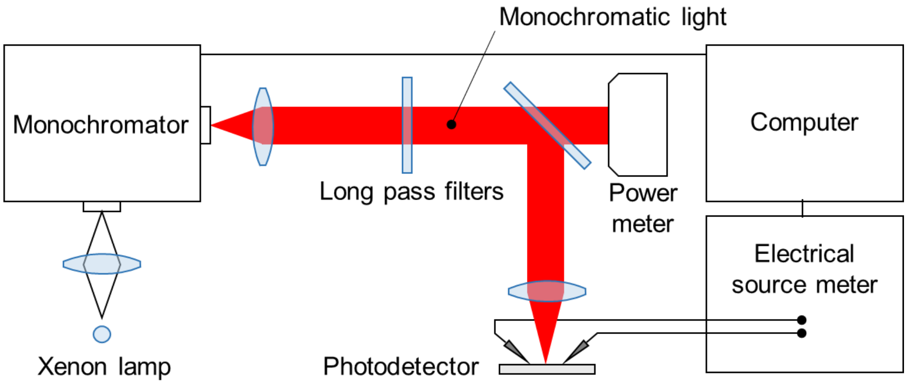

Figure 3.13. Photodetector spectral response measurement system

3.5.3. Pressure sensor characterizations

The pressure sensor characteristics was measured by monitoring the change of current in response to pressure, as schematically shown in Figure 3.14. Precisely controlled external pressure was applied on the device using linear voice coil actuator (PIMag® VoiceCoil Linear actuator, V-275.431). The linear voice coil actuator was controlled in 1 mN force resolution and the pressure was applied on the device through 2 × 2 mm^2 insulating block that had flat surface.

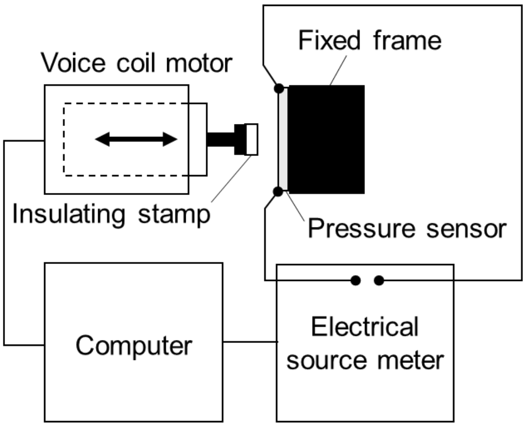

Figure 3.14. Pressure sensor measurement system

3.5.4. LED characterizations

The LED characteristics were investigated by operating the LED using electrical source meter and measuring the electroluminescent (EL) power and spectra, as schematically shown in Figure 3.15. Optical microscope (Carl Zeiss Co. Axioskop 2 MAT) was used for probing as well as EL emission collecting. Electrical source meter (Keithley 2400) was used to measure *I–V* curves and to apply voltages or currents to LEDs. EL spectra were measured using a monochromator (Dongwoo Optron Co. DM150i) and a detection system equipped with a charge-coupled device (Andor InC. DU401A). The output power of the LED was measured by a UV extended Si photodetector (Thorlabs S120VC), which was placed on the backside of the LEDs. The resolution of the EL spectrum was 1 nm and the typical scan range was between 300 to 800 nm. To investigate the output power and the efficiency of the LEDs, the emission power was directly measured by power meter. The power of the LED was also estimated by comparing the EL spectra with the reference LED sample.

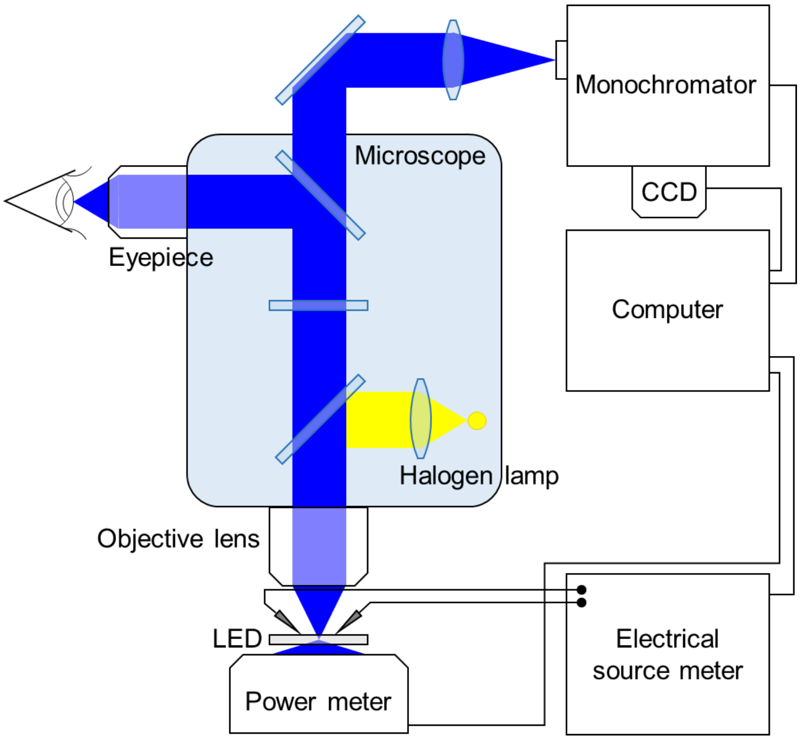

Figure 3.15. Schematic illustration of the LED characterization system.

3.6. Structural characterization

Morphological and microstructural analyses were performed using a field-emission SEM (FE-SEM; Carl Zeiss AURIGA) and high-resolution TEM (HR-TEM; FEI Tecnai F20), respectively. For cross-sectional TEM imaging and electron diffraction analysis, samples were milled with 30-kV-accelerated gallium ions using a focused ion beam machine (FIB; Quanta 3D FEG) in dual-beam mode. The compositional profile of each layer was obtained from EDX spectroscopy in the scanning TEM mode (STEM-EDX; JEOL JEM 2100F).

Individually addressable nanorod device arrays on graphene substrate

4

4.1. Introduction

1D nanomaterials can be an ideal building block for ultimate density devices, since the diameter of 1D nanostructures can be reduced down to a few atoms thickness[31] and even a single nanorod can have many functionalities by elaborately forming axial and coaxial heterostructures.[5, 6, 33] Nevertheless, because of the difficulties in preparing the 1D nanomaterials and nanodevices in a well-controlled and ordered manner, it has long been very challenging to monolithically integrate many number of single 1D nanostructure device into a small space in a well-organized manner. Recently, to make addressable nanorod devices, methods of growing 1D nanomaterials on electrodes pre-patterned substrates have been suggested. However, because of the difficulties in preparing bottom electrodes that have growth compatibility with 1D nanomaterials, this method only worked for the addressing of bundles of nanorods synthesized by low-temperature hydrothermal growth method.[28] The individual addressing of single 1D nanomaterials would require fundamentally different approach. In this chapter, we suggest that these obstacles can be overcome basically using 1D nanomaterial arrays grown on 2D layered nanomaterials (see Figure 4.1).

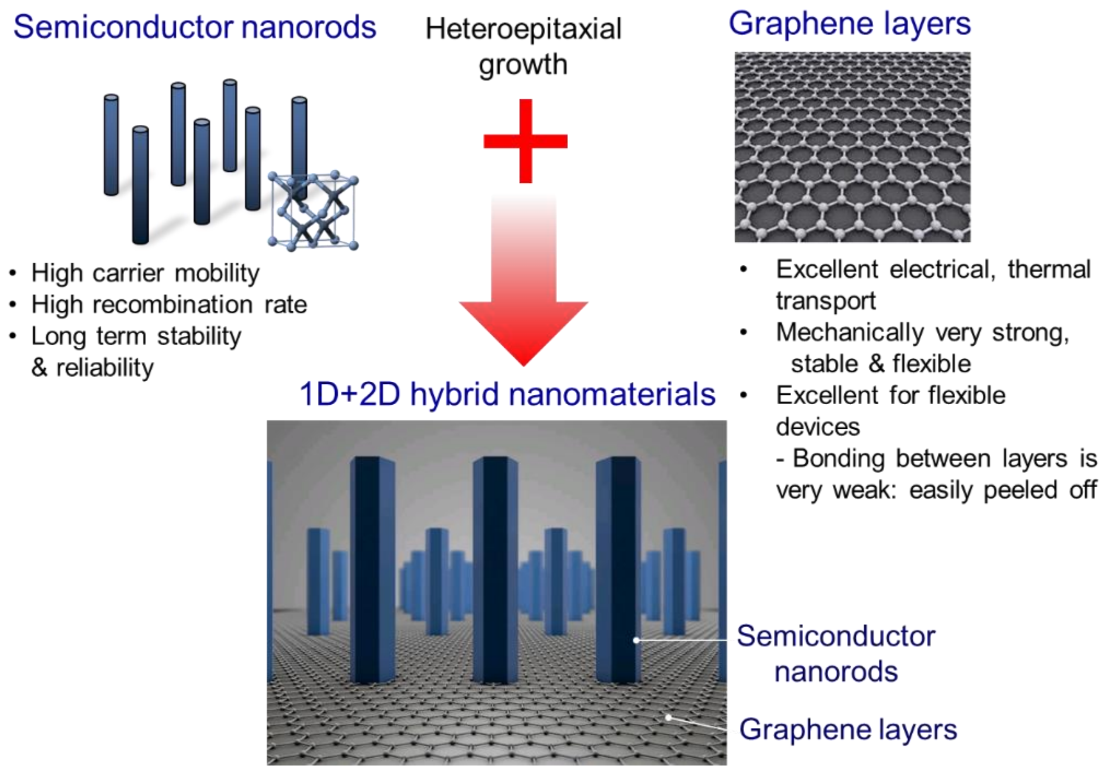

Figure 4.1. 1D+2D hybrid dimensional nanomaterials prepared by heteroepitaxial growth of 1D semiconductor nanorods on 2D graphene layers.

The 1D+2D hybrid nanomaterials, composed of 1D semiconductor nanorods grown on 2D layered nanomaterials, can be easily lifted-off from the substrate[10] and the bottom electrodes can be simply formed on the underlying surface of the hybrid nanomaterials without considering the growth compatibilities. Additionally, this 1D+2D hybrid nanomaterial system can synergistically integrate the advantages of each nanomaterial. In this chapter, the fabrication and characteristics of ultrathin and individually addressable ZnO nanorod device arrays on graphene layers will be presented. The graphene layers played a critical role in this work. They not only served as a heteroepitaxial substrate for vertical ZnO nanorod growth but they also acted as a lift-off layer and ultrathin electrodes for flexible device operation.

4.2. Ultrathin and individually addressable ZnO nanorod device arrays on graphene layers

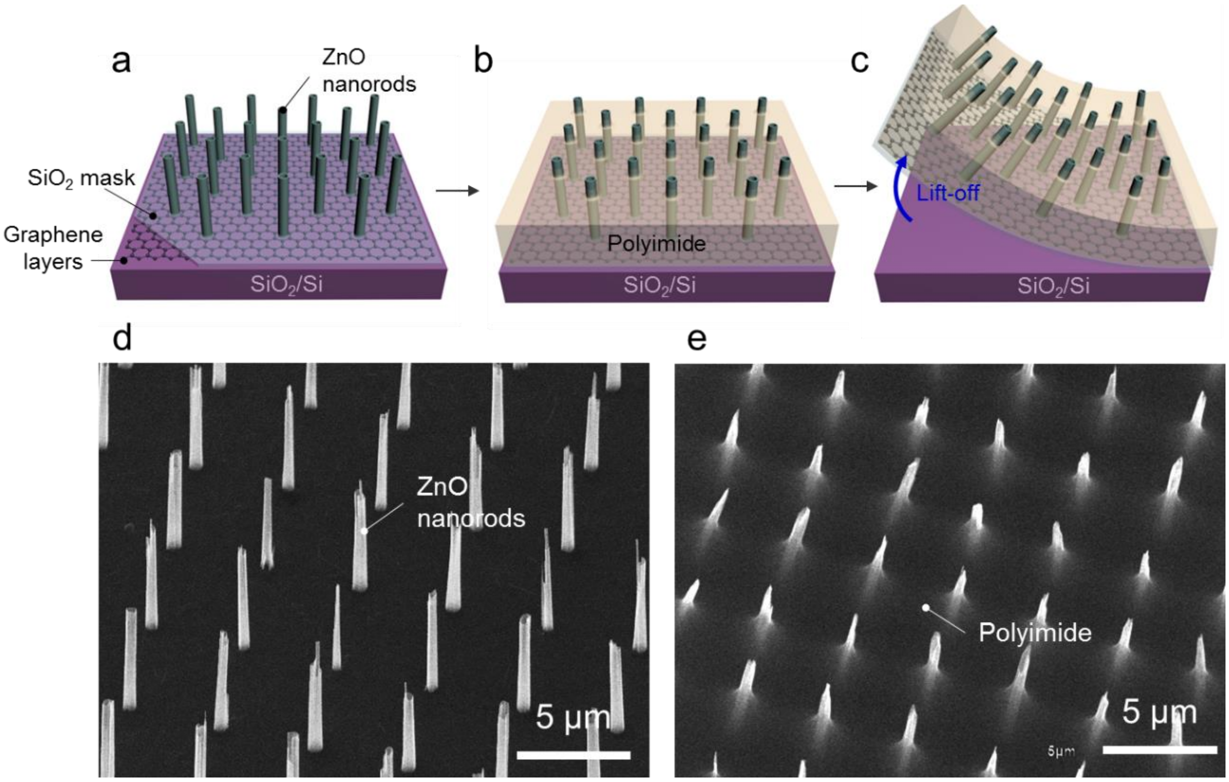

Figure 4.2. Ultrathin layer composed of ZnO nanorod arrays on graphene layers embedded in PI layers. (a) Selective area MOVPE growth of ZnO nanorod arrays on CVD graphene layers, followed by (b) polyimide layer coating and (c) mechanical lift-off. (d) Corresponding tilted SEM image of the ZnO nanorod arrays on graphene substrate and (e) after PI layer coating and lift-off.

The basic strategy for the fabrication of flexible vertical nanodevice array is illustrated in Figure 4.2. As schematically shown in Figure 4.2(a), the first step is the preparation of vertically aligned ZnO nanorod arrays on CVD graphene layers.[9] The nanorods exhibited excellent uniformity, with a mean length, diameter, and period of 7, 0.5, and 4 μm, respectively, all of which could be controlled by changing the lithography design and growth parameters. After preparing the ZnO nanorod arrays on CVD graphene layers, the gaps among the nanorods were filled with an insulating, flexible polyimide layers. As an essential step for creating a flexible device, the entire layers were mechanically lifted-off from the substrate (Figure 4.2(b)), due to the weak bonding strength between the substrate and the graphene layers. After these freestanding layers composed of ZnO nanorods/graphene layers embedded in PI layers were prepared, the nanostructure-embedded layers were cured, which enhanced the mechanical strength and chemical resistance of the layers.

The freestanding form of ZnO nanorod arrays on graphene films, embedded in polyimide film, enabled the fabrication of flexible ZnO nanorod crossbar array. The basic approach for fabricating flexible and individually addressable nanorod crossbar arrays is shown in Figure 4.3. After preparing freestanding form of ZnO nanorod arrays on graphene films, gold (Au) electrode lines with 3.7 μm period were deposited on the top surfaces of the ZnO nanorods in a highly aligned manner with the nanorod array, as schematically shown in Figure 4.3(a). Au electrodes was used to make Schottky contact on ZnO nanorods, since Au and single-crystalline ZnO nanorods are well known to form good Schottky contact.[43] After flipping the freestanding layers upside-down, chromium (Cr)/Au electrode lines were formed on the bottom surface of nanorods in the same manner (see Figure 4.3(b)). Then, graphene layers that were not covered with Cr/Au were removed by dry etching, so that graphene layers/Cr/Au bottom electrodes were formed. Ohmic contact can be expected at the bottom side composed of ZnO nanorod/graphene layers/Cr/Au.[18, 44] The tilted SEM image in Figure 4.3(d) shows the top Au electrode lines formed in a precisely aligned manner with the ZnO nanorod arrays. Figure 4.3(e) shows the top view SEM image of the graphene layers/Cr/Au electrode lines formed on the bottom surface of the ZnO nanorod arrays.

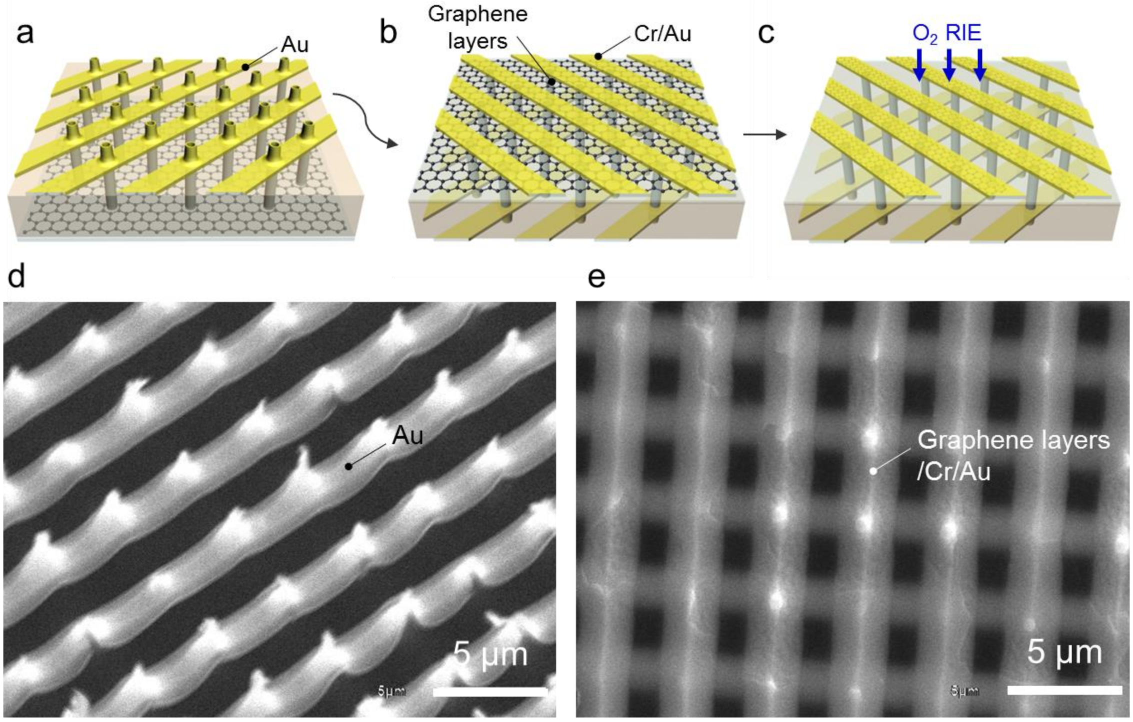

Figure 4.3. Microelectrode fabrication for individually addressable nanorod device. Schematic illustration of making (a) Au-ZnO Schottky contact on the top side and (b) depositing Cr/Au electrodes and (c) etching the exposed graphene layers to make ZnO-graphene layers/Cr/Au ohmic contact on the bottom side. (d) Corresponding tilted SEM image of top Au electrode lines formed on the upper surface of ZnO nanorod array and (e) bottom graphene layers/Cr/Au electrode lines formed on the bottom surface of the ZnO nanorod array.

The final device structure are schematically illustrated in Figure 4.4(a), where Au and graphene layers/Cr/Au electrodes are contacting the top and bottom surface of a single nanorod and crossing each other. The photograph of the device in Figure 4.4(b) shows that the device layer had an ultrathin and extremely flexible form. The highly-ordered, regular formation of single nanorod nanodevice array was confirmed by field emission (FE) SEM images in Figure 4.4. The top and bottom electrode lines were formed in a highly aligned manner with each ZnO nanorod, contacting top and bottom surface of each ZnO nanorod and crossing each other perpendicularly, forming a 16 by 16 single ZnO nanorod crossbar array. The unit nanodevice was composed of a single ZnO nanorod with Au top contact and graphene layers/Cr/Au bottom contact separated by PI spacer.

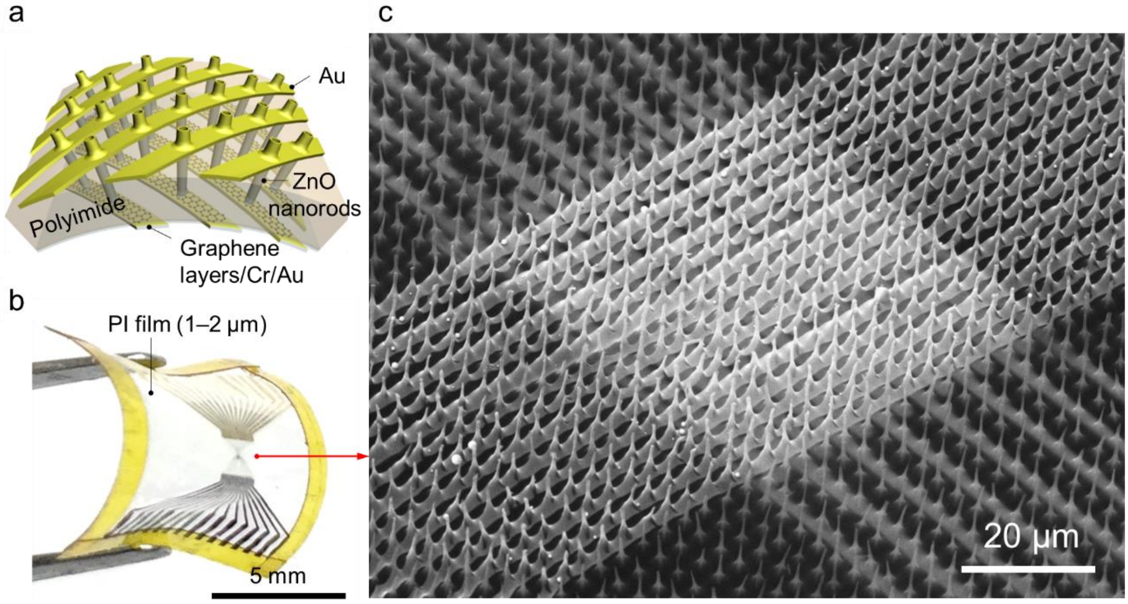

Figure 4.4. Ultrathin and individually addressable ZnO nanorod device arrays on graphene. (a) Schematics of the final device structure. (b) Photograph of the actual device and (c) tilted FE-SEM image of the nanorod device array.

The FE-SEM images of the upper and lower surface of the device are shown in Figures 4.5(a) and (b), respectively. In these images, we can see that the Au and graphene layers/Cr/Au electrode lines were formed in a highly aligned manner with the nanorod array, conformally contacting top and bottom surface of each ZnO nanorod. The cross-sectional FE-SEM image of the device are shown in Figure 4.5(c), from which we can see that the top and bottom electrodes were spatially separated with PI spacer and the PI layer between the nanorods were as thin as 1.4 μm (the vertical and horizontal scales of the cross-sectional FE-SEM image are calibrated to be the same). The coaxial thickness of the PI layer coated on each nanorod gradually decreased from 1 to 0 μm as the distance from the substrate increased from 1 to 5 μm. The morphology of the PI layer near the ZnO nanorod arrays can be controlled by changing the spin coating speed, oxygen plasma treatment time, and the spacing between nanorods. On the uppermost region of the ZnO nanorods, Au-ZnO contact was formed on the 2-μm-long exposed area of ZnO nanorods.

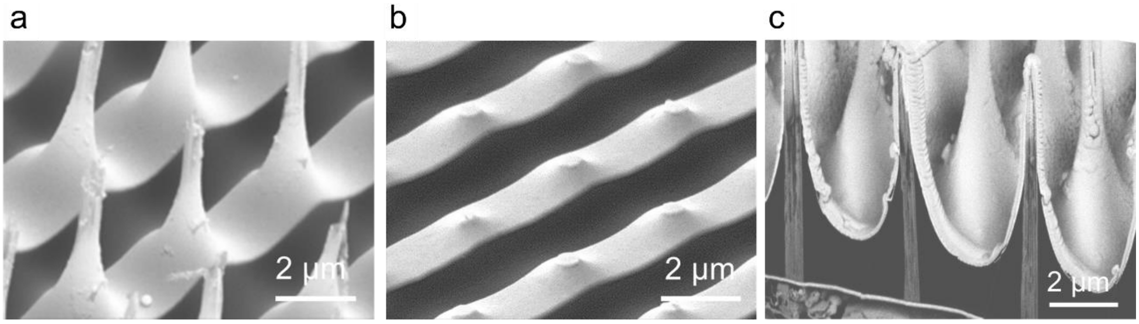

Figure 4.5. FE-SEM images of the (a) top and (b) bottom surface and (c) cross-section of nanodevice array.

4.2.1. Electrical characteristics of individual ZnO nanorod devices

The electrical characteristics of the nanodevice arrays were investigated by measuring their current–voltage (*I*–*V*) characteristics curves. Figure 4.6 shows the typical *I*–*V* curves of the nanodevices which showed good rectifying behavior and low leakage current. The nonlinear and clear rectifying behavior in *I*–*V* characteristics results from the Schottky contact formation between the Au electrode and ZnO nanorod. These diode elements, which can act as a selector in crossbar array, are very important in preventing crosstalk effect for the reliable operation of the crossbar array.[45] 98% of the nanodevices showed good Schottky diode characteristics as shown in Figure 4.6. However, 2% of the nanodevices showed high reverse leakage current. These exceptional behavior presumably results from the slight variation in ZnO nanorod morphology and metallization conditions, which can results in point contact junctions and easy electron tunneling across metal-semiconductor interface.

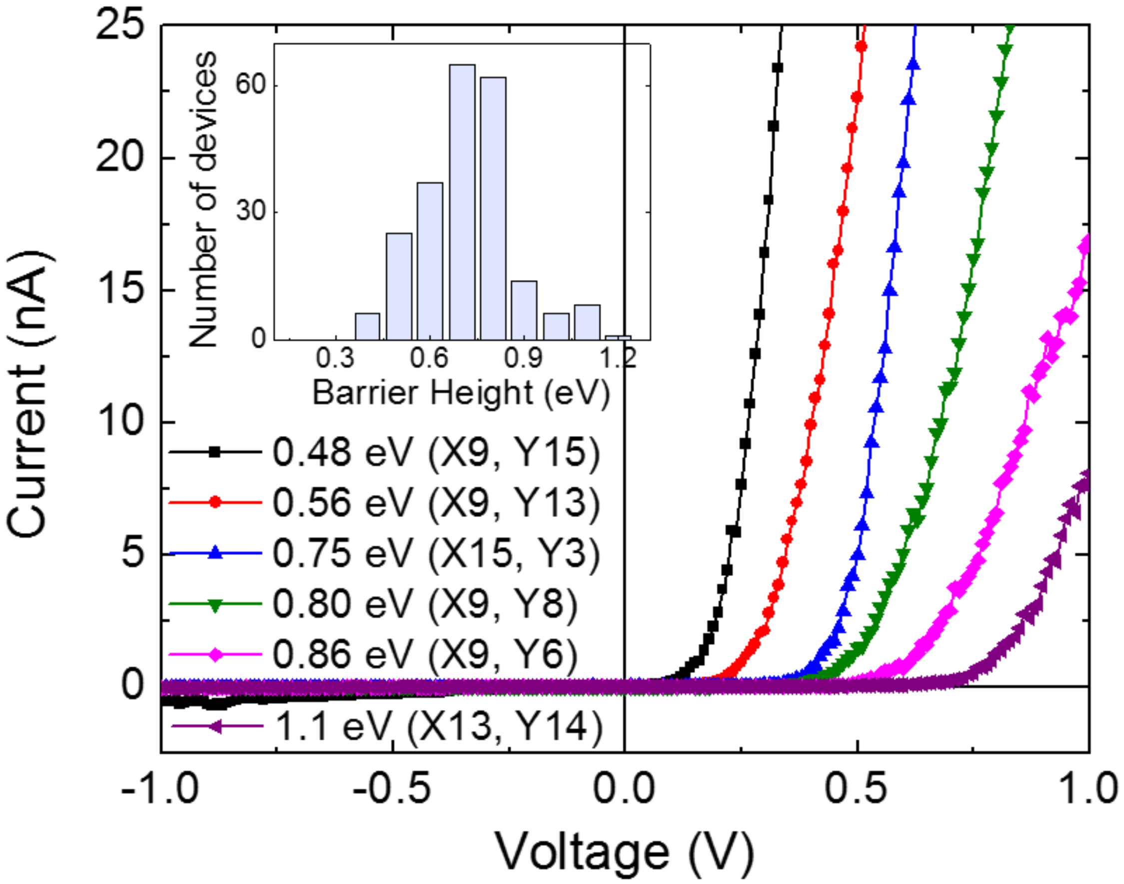

Figure 4.6. Current–voltage characteristics curves from individual nanorod devices within the nanorod device array. The inset figure shows the histogram of the estimated barrier height values of the devices.

Quantitative Schottky diode characteristics were investigated further by obtaining barrier height from the *I–V* characteristic curves of the devices. The *I–V* curves of the nanodevices with different barrier height were shown in Figure 4.6. Comparing the nanodevices having different barrier heights, we can see that the Schottky diode with higher barrier height have higher turn-on voltage and lower current level under the same forward bias voltages. The inset figure in Figure 4.6(b) shows the histogram of the barrier height, where the barrier height showed considerable variations ranging from 0.4 to 1.2 eV, and the most frequently observed value for the barrier height was 0.7 eV.

The electrical characteristics of the nanodevice array were investigated by spatially mapping the barrier heights of all the nanodevices in the array, as shown in Figure 4.7. Some electrode lines that were not properly connected to the measurement system were excluded in this diagram. The barrier height of individual nanodevices were different from each other with considerably huge variation ranging from 0.4 to 1.2 eV. The observed nonuniformities of the individual nanorod devices presumably resulted from the nanoscale variation in the morphology of each nanorod in the array which also resulted in different metallization conditions for each nanorod device. We believe that such nonuniformity can be improved by optimizing the conditions for the growth and fabrication processes.

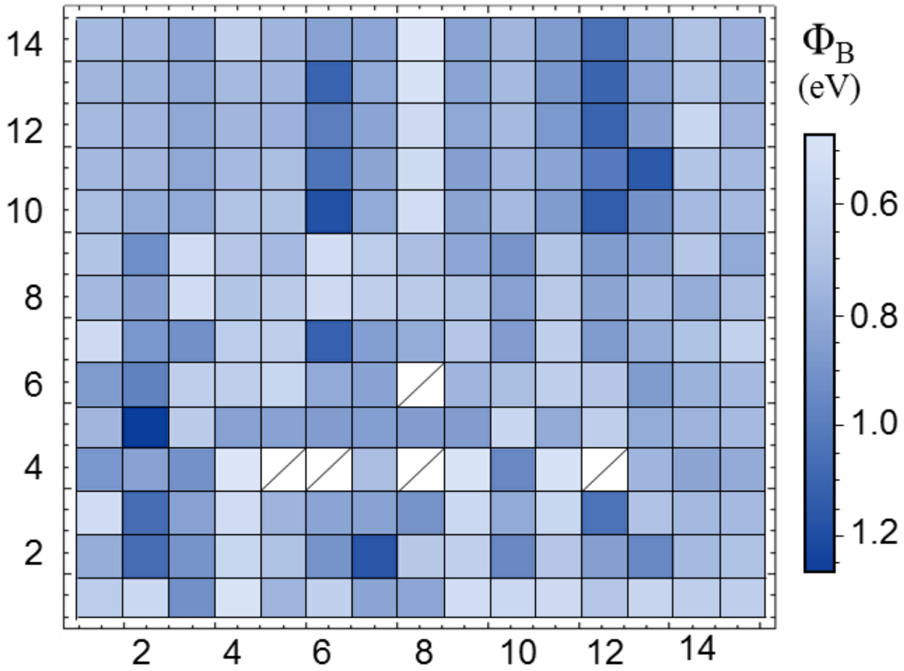

Figure 4.7. Mapping of the estimated barrier heights of the nanorod device array. 98% of the devices shows Schottky diode characteristics and 2% of the devices (marked with diagonal-square) shows ohmic characteristics or diode characteristics with high leakage current level.

4.2.2. Flexible device characteristics

The vertical nanodevice array could accommodate extreme bending conditions because of the micrometer-sized dimension and spacing of the nanodevice arrays.[46, 47] To evaluate the effect of mechanical deformation, the nanodevice arrays were bent by intentionally forming a wrinkle such that the bending radius was 50 μm. Figure 4.8(a) shows the corresponding FE-SEM image of the wrinkled film; no sign of tear or damage to the array is observable. Hybrid structure with nanorod that have a very small contact area with the graphene exhibited remarkable endurance under flexural deformation. Furthermore, because the bending radius was much larger than the characteristic dimension and spacing of the nanodevice array, the macro-sized curvature imposed by the bending did not affect the local structural integrity of the nanodevice array.[37]

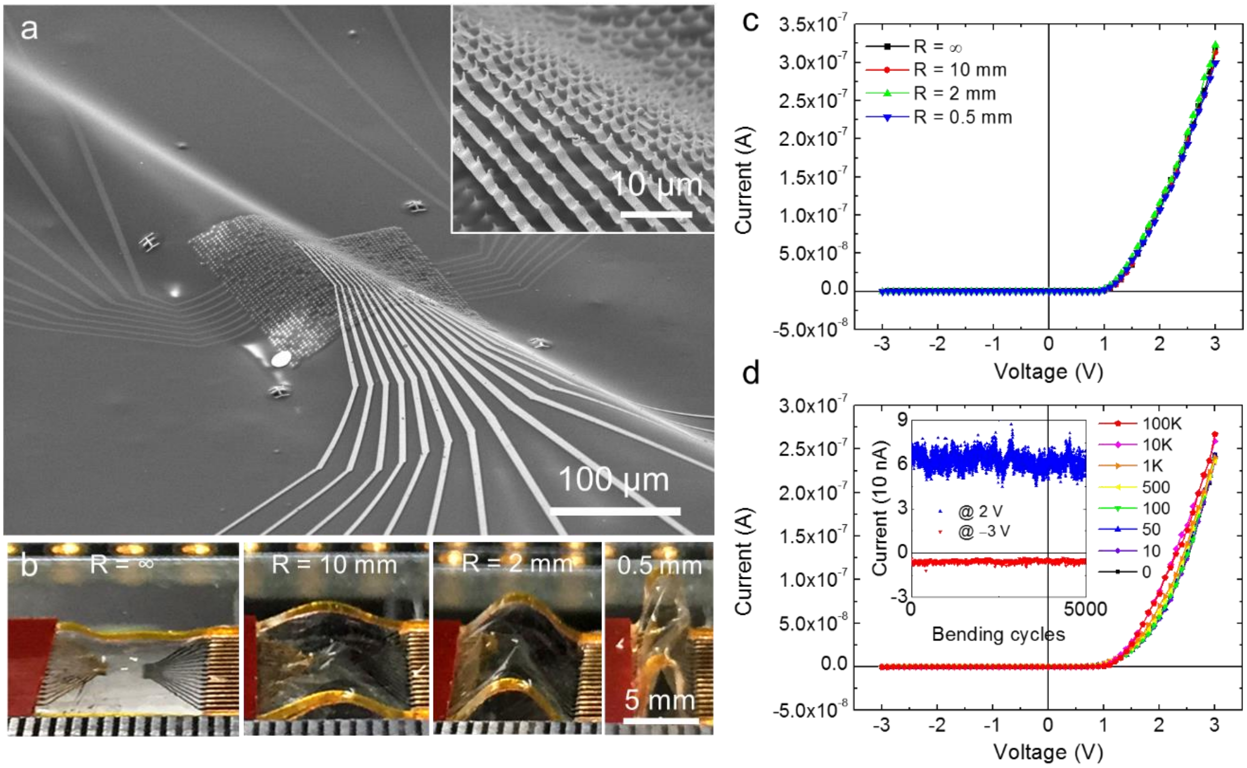

Figure 4.8. Flexible nanodevice array. (a) SEM image of the device under a few tens of micrometer scale bending radius. The inset shows higher magnification

SEM image near the crossbar junctions. (b) Photography of the device under various bending radii of ∞, 10, 2, and 0.5 mm, and the corresponding (c) current–voltage characteristics curves measured under these bending radii. (d) Current–voltage characteristics curves under repeated bending cycles. Inset graph shows the current level monitored at 2.0 and –3.0 V with repeated bending cycles.

The effect of bending on the nanodevice array was further investigated by obtaining electrical characteristics at various bending radii. Figures 4.8(b) and (c) shows photographs and corresponding *I–V* curves at bending radii of ∞ , 10, 2, and 0.5 mm. The *I–V* curves obtained at different bending radii (Figure 4.8(c)) exhibited very similar rectifying behavior, without appreciable differences in the device parameters, such as the turn-on voltage or leakage current. This suggests that no serious mechanical damage or fracture occurred at the electrodes or the junctions between the nanostructures and graphene during the bending test.

Additionally, the reliability of the nanodevice array under repeated bending conditions was investigated by measuring electrical characteristics on repeating up to 100,000 bending cycles. First, as shown in Figure 4.8(c), the nanodevice array exhibited almost identical *I–V* curves with repetitive bending, and the integrated emission intensities remained nearly constant over up to 100,000 bending cycles. In addition to the luminescent characteristics, the electrical characteristics were preserved with repetitive bending, exhibiting very similar rectifying *I–V* curves shown in the inset of Figure 4.8(c). The device parameters, including the forward (I_f) and reverse current (I_r) at 2.0 and –3.0 V, were recorded while dynamically bending the ultrathin device. As shown in the inset of Figure 4.8(d), both I_f and I_r did not significantly degraded with repeated dynamic bending cycles; I_f and I_r remained nearly constant value of 6×10^{-8} and 5×10^{-9} A, respectively. All these characteristics of the nanodevice array fabricated on graphene films demonstrate reliable operation of the ultrathin in a flexible form.

4.3. High-spatial-resolution ZnO photodetector arrays on graphene

4.3.1. Photodetector characteristics of ZnO nanorod devices

Ultraviolet (UV) photosensor characteristics of the ZnO nanorod device arrays were also investigated. Figure 4.9 shows the UV irradiation power dependent *I*–*V* curves of the nanodevice, which show the dark and photoexcited current levels. With increasing irradiation power density ranging from 0.02 to 20 mW/cm^2, the current levels in both forward and reverse bias voltages clearly increased. Dramatic increase in current level was observed at reverse bias voltages. Especially, at −3.0 V, the currents level increased nearly three orders of magnitude.

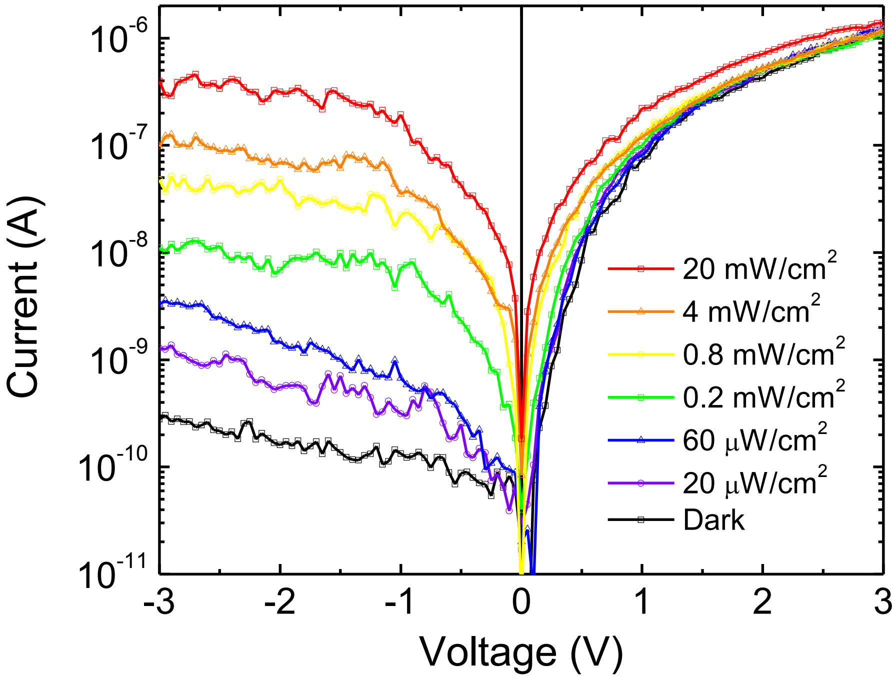

Figure 4.9. *I*–*V* curves of the nanorod device with increasing UV irradiation power.

4.3.2. Spectral and temporal responses

The detailed photosensor characteristics were investigated by measuring the temporal and spectral photoresponses of the nanorod device arrays. The time-dependent photoresponses were measured under duty-cycled on/off (30/30 s) UV irradiation in Figure 4.10. The UV irradiation dramatically increased the electrical current of the ZnO nanorod photosensor at a bias of −3.0 V. The mean on/off ratio of the photocurrent-to-dark current of the ZnO nanorod photodetector was measured to be ~100, indicating sensitive UV detection of the ZnO nanorod.

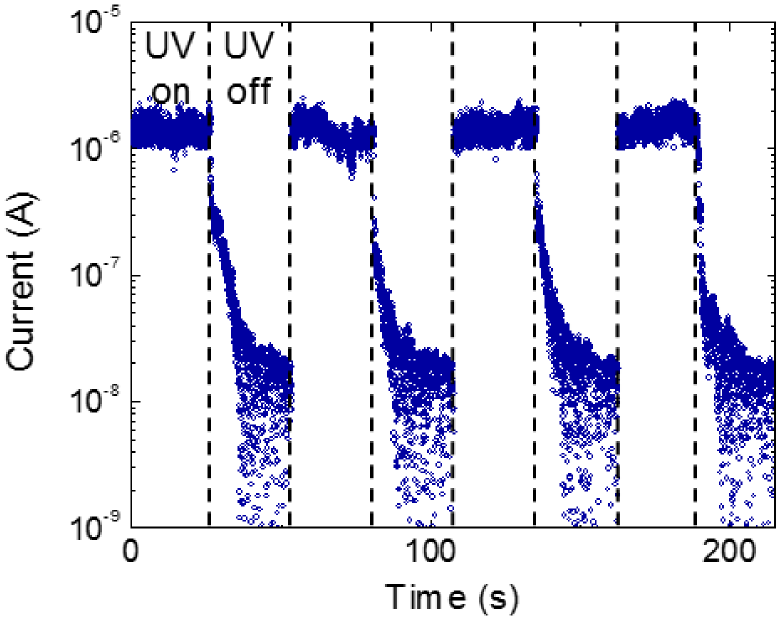

Figure 4.10. Temporal response of the nanorod device to UV illumination

Notably, no obvious photoresponses were observed by indoor light illumination or white radiation from a halogen lamp, indicating that the UV photoconductor device of the ZnO nanorod is selectively sensitive only to UV light with a photon energy higher than the band gap energy of ZnO. This selective UV sensitivity is evident in Figure 4.11, which shows spectral sensitivity of the nanodevice. As we can see in this graph, the nanodevice showed high responsivity near the UV wavelength range (300–

380 nm), but showed low responsivity in the visible range (380–500 nm). The peak responsivity of 9 × 10^5 A/W was observed a 310 nm and the responsivity rapidly decreased near 330 nm. The inset figure in Figure 4.11 shows the spatial mapping of the responsivity of each nanodevice in the crossbar array. All the nanorod devices in the array showed high responsivities in the order of 10^5–10^6 A/W, but the responsivity of individual Schottky photodiodes were different from each other. The observed nonuniformities of the responsivity of individual nanorod devices presumably resulted from the nanoscale variation in the nanomaterial morphology and the metallization conditions. However, we believe that such nonuniformity can be improved by optimizing the conditions for the growth and fabrication processes.

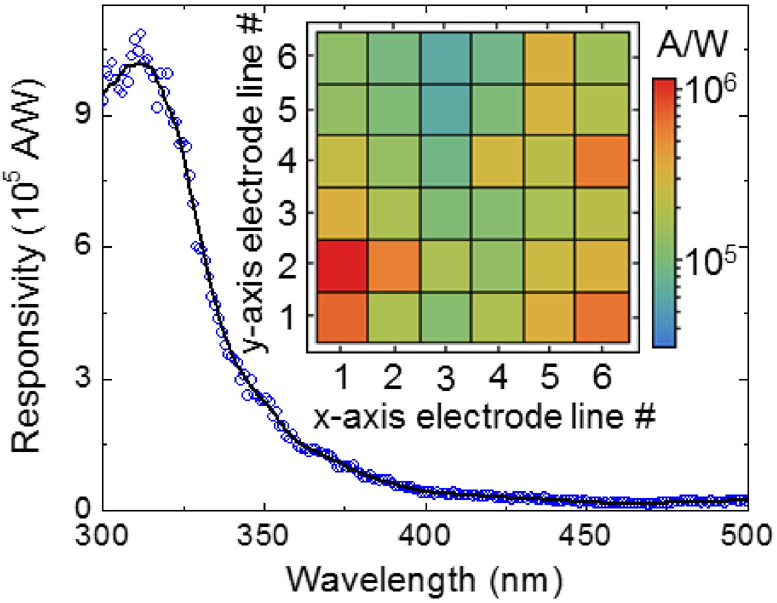

Figure 4.11. Spectral photoresponse of the nanorod device in the array. Inset figure shows the spatial mapping of the responsivity of the nanodevices in the array.

4.4. High-spatial-resolution ZnO nanorod pressure sensor arrays on graphene

The pressure sensor characteristics of the ZnO nanorod device arrays were investigated based on the previous studies that ZnO nanostructures can be used for strain-gated piezotronic transistors.[28, 48] Under various pressure ranging from 0 to 50 kPa, the current level was measured at bias voltages between −2.5 and 2.5 V as shown in the pressure dependent *I*–*V* curves in Figure 4.12. With increasing pressure from 0 to 25 kPa, the current levels at forward bias voltages continuously dropped. However, above 25 kPa, the increasing pressure did not further affected the current level. Since there can be many possible origins other than the piezoelectricity of ZnO that might affected the change in current level of the device while pressing, more profound study would be necessary to understand the real origin of the observed results.

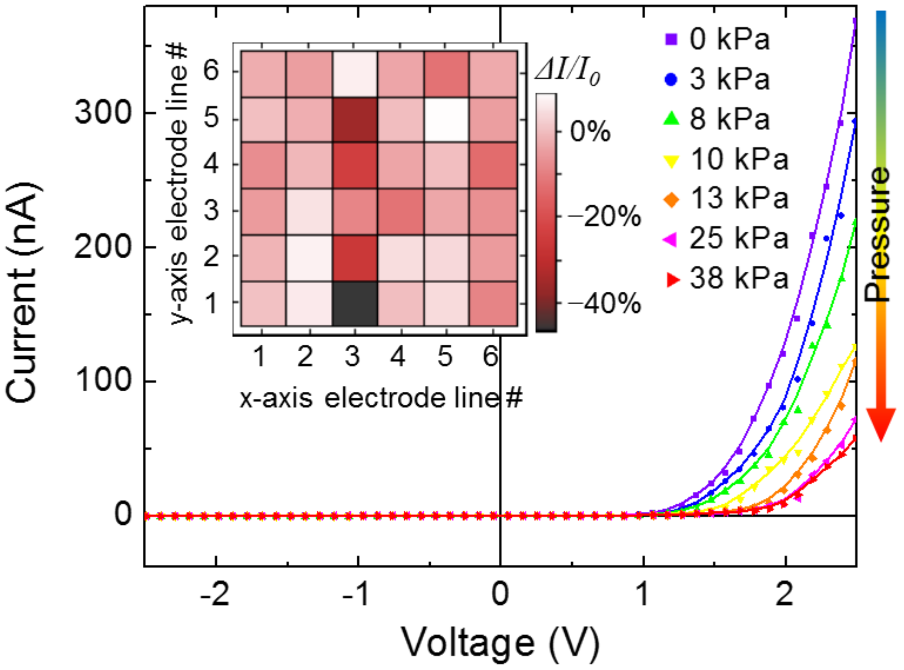

Figure 4.12. Pressure-dependent *I*–*V* curves of the single ZnO nanorod device in the array. The inset figure shows the spatial variation of pressure sensitivity.

The pressure sensitivity of each nanodevice in the array was evaluated by spatially mapping the change in current level under the 75 kPa external pressure, as shown in the inset figure of Figure 4.12. Generally almost all nanorod devices in the array showed decrease in current level under external mechanical pressure. However, the degree of current level changes under the same pressure were different from each other and some nanorods in the array actually showed no change in current level. The observed nonuniformities of the pressure sensitivity of individual nanorod devices presumably resulted from the slight variation in the height and morphology of the nanorods in the array, as we can see in the SEM image in Figure 4.2. Under the same pressure, a slightly longer nanorod can show a clear pressure-response, whereas some relatively shorter nanorod device may not even be pressed. However, we believe that such nonuniformity can be improved by optimizing the conditions for the growth and fabrication processes.

The temporal pressure-responses of the ZnO nanorod crossbar array was measured to further investigate the reliability of the pressure sensor. The time-dependent pressure-responses were measured by monitoring the current at a bias of 2.0 V under 50 kPa press-and-release cycles (10/10 s) as shown in Figure 4.13. As soon as the pressure was applied on the device, the current level rapidly dropped from 300 to 20 nA and, when the pressure was released, the device immediately recovered its original conductivity. The mean on/off ratio of the current with and without 50 kPa pressure was measured to be ~150, indicating sensitive pressure sensor characteristics of the ZnO nanorod based nanodevices.

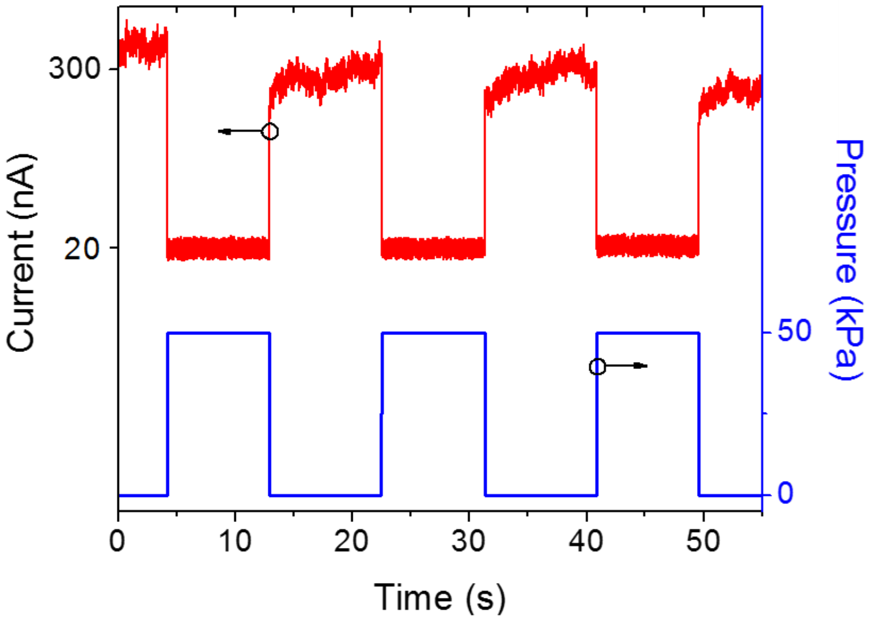

Figure 4.13. Temporal pressure response characteristics measured at bias voltage of 2.0 V under press-and-release cycles at 50 kPa.

4.5. Light-emitting diodes using GaN/ZnO coaxial nanorod arrays

One of the most important key advantage of nanorods is that they can incorporate very rich functionalities in a single nanorod by making axial or coaxial nanorod heterostuctures.[33] So far, we have discussed the device applications based on ZnO nanorod arrays grown on graphene substrates. By forming coaxial nanorod heterostructures on the ZnO nanorod arrays, tremendous varieties of applications can be realized. In this section, we coaxially coated GaN layers on the ZnO nanorods for LED applications (see Figure 4.14). High quality GaN shell layers can be heteroepitaxially coated on ZnO nanorods, because GaN and ZnO have the same wurtzite crystal structure and a low lattice constant misfit of 1.9%.[49]

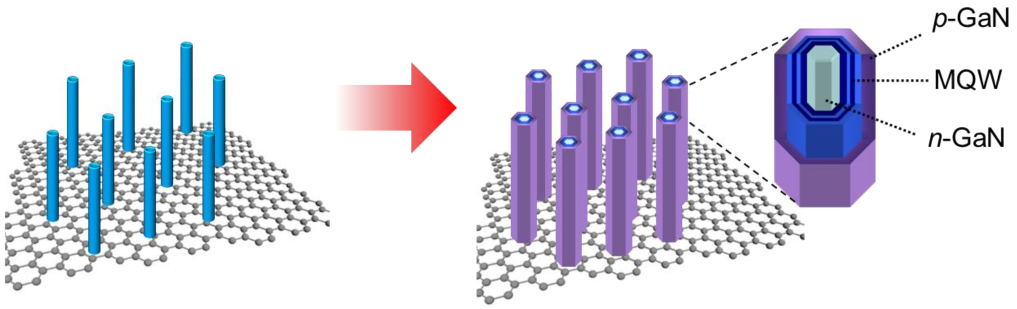

Figure 4.14. Schematic illustration of position- and dimension-controlled ZnO nanorod arrays on graphene substrates and the coaxial coating of *p*-GaN, *u*-$In_xGa_{1-x}N$/GaN multiple quantum wells (MQWs), and *n*-GaN layers on ZnO nanorod arrays for LED application.

These coaxial GaN nanorod LEDs can have many advantages over conventional GaN thin film LEDs (see Figure 4.15). Nanostructured LEDs can have (1) larger surface area for light-emission,[26] (2) higher light out-coupling efficiency,[50] (3) reduced quantum confined stark effect (QCSE) due to the use of non/semi-polar facets,[51] and (4) higher crystallinity compared to conventional thin film LEDs[52]. This section will describe LED applications of GaN/ZnO coaxial nanorod heterostructure arrays grown on graphene substrates. Additionally, metal-cored GaN/ZnO microtube will be presented as a method to significantly improve current spreading characteristics and output power of the nanostructured LEDs.[40]

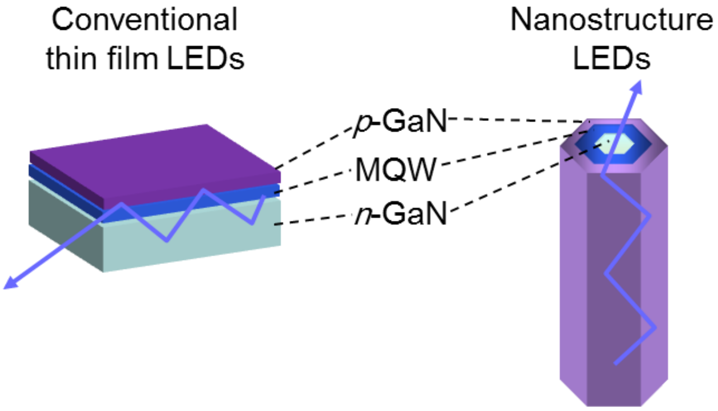

Figure 4.15. Schematic illustration of conventional thin film LEDs and coaxial nanorod LEDs.

4.5.1. GaN/ZnO coaxial nanorod LED arrays on graphene

Flexible inorganic LEDs on graphene layers can be demonstrated by employing $In_xGa_{1-x}N$/GaN LED structures on ZnO nanorod arrays. This device concept was first demonstrated by C.-H. Lee *et al.* using randomly nucleated GaN/ZnO nanorods grown on CVD graphene layers.[10] Although flexible LEDs on graphene were already successfully demonstrated with randomly nucleated nanorod arrays on graphene, flexible LEDs fabricated with position- and morphology-controlled GaN/ZnO coaxial nanorod arrays on graphene are expected to show higher power, uniformity, and reliability. Additionally, as I emphasized many times in this thesis, the position controlled preparation of GaN/ZnO nanorods is also a very important step to fabricate individually addressable nanorod device arrays. Using this highly controlled

GaN/ZnO nanorod array on graphene, high-resolution microdisplay can be fabricated where each nanorod LED works as an individual pixel.

The position- and morphology-controlled GaN/ZnO coaxial nanorod array on CVD graphene layers were demonstrated as shown by the tilted SEM image in Figure 4.16. This structure was fabricated by heteroepitaxially coating *p*-GaN, *u*-$In_xGa_{1-x}N$/GaN multiple quantum wells (MQWs), and *n*-GaN layers on position- and morphology-controlled ZnO nanorod arrays grown on CVD graphene layers. The coaxial coating of GaN and $In_xGa_{1-x}N$ layers on ZnO nanorod increased the diameter of the nanorods from 0.5 to 3 μm. We can see that the GaN/ZnO nanoarchitectures had clearly defined hexagonal facets with mean height, diameter, and spacing of 8, 3, and 4 μm, respectively.

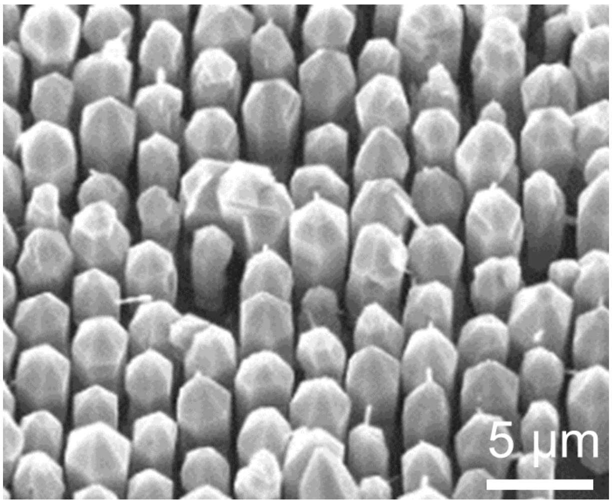

Figure 4.16. SEM image of the position- and morphology-controlled GaN/ZnO nanoarchitecture arrays grown on CVD graphene substrates.

Nanostructured LED was fabricated by filling the gaps between the nanorod arrays using polyimide layers and making ohmic metal contact on both the upper *p*-GaN surface of the GaN/ZnO coaxial nanorods and the underlying graphene layers. The $I-V$ characteristics curve in Figure 4.17(a) shows clearly rectifying behavior, indicating the formation of good $p-n$ junctions. EL characteristics of the LED is shown in Figure 4.17(b), where blue light-emission was observed with a dominant EL peak observed at 428 nm. The inset figure in Figure 4.17(b) shows the EL image of the LED. The multiple light-emitting spots on the EL image indicate light-emission from discrete GaN/ZnO nanorod arrays. However, non-uniformities in EL emission were also observed from the nanorod arrays; the brightness of each nanorod LED was different with each other and slight difference in EL colors was observed as well. Additionally, it seems like there were many nanorods which did not emitted light at all. The non-uniformities observed in nanorod LED arrays may be due to the slight variation in the morphology of the nanostructured LEDs, which can result in difference in chemical composition and thickness of each LED layer. I believe that the uniformity of the nanorod LED array can be improved by further optimizing the uniformity of the nanomaterials and developing more reliable device fabrication methods.

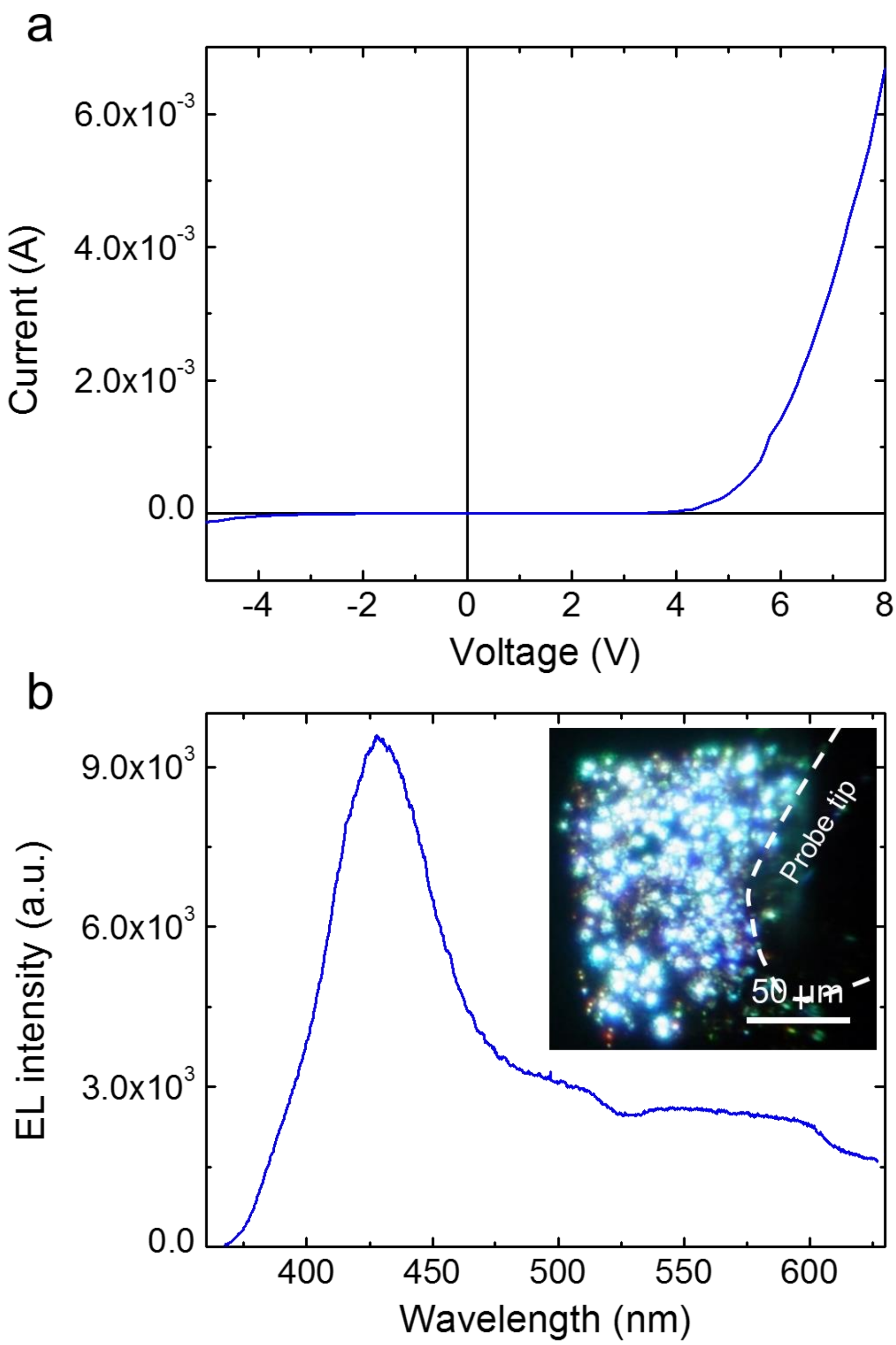

Figure 4.17. LED characteristics of position- and morphology-controlled GaN/ZnO coaxial nanorod LED arrays grown on CVD graphene substrates. (a) *I*−*V* and (b) EL spectrum of the LED. Inset figure shows the EL image of the device.

4.5.2. Metal-cored nitride semiconductor microtube LED arrays

Three-dimensional (3D) semiconductor nanoarchitectures, including nano- and microrods, pyramids, and disks, are attracting tremendous interest as candidates for next-generation light emitters,[53-55] as they offer a huge amount of additional light-emitting area[56-58] and enhanced light out-coupling efficiency[26, 59, 60] compared with that of planar LEDs and show many unconventional properties that were very hard to achieve with conventional LEDs.[61-63] The unique characteristics of nanoarchitecture LEDs include the use of semipolar/nonpolar nano- or microfacets of nitride semiconductor nanostructures that can significantly reduce the quantum-confined Stark effect,[51] which is known to have detrimental effects on the device characteristics of planar LEDs.[64] Additionally, using the difference in the growth dynamics of each facet in multifaceted nitride nanoarchitectures, it is possible to fabricate multicolored LEDs on a single substrate without phosphor conversion.[65] Furthermore, due to their elaborate 3D geometry, the current spreading characteristics of 3D nanoarchitecture devices differ dramatically from those of conventional thin film devices, which can be exploited in a highly controlled manner.[63, 66, 67] For instance, by carefully controlling the spatial distribution of the current density over multifaceted GaN LEDs, color-tunable LEDs have been produced.[63] However, to obtain very bright single-color LEDs or laser diodes, a uniform, high density electrical current must be injected into the entire active area of the nanoarchitecture device. Here, we report a novel device structure where currents with the required properties can be injected into the 3D semiconductor nanoarchitecture LEDs. This is achieved by depositing layers of metal into the microtube LEDs to form a metal core. We investigated the effects of the metal cores in coaxial nitride tube LEDs experimentally and by computational modeling.

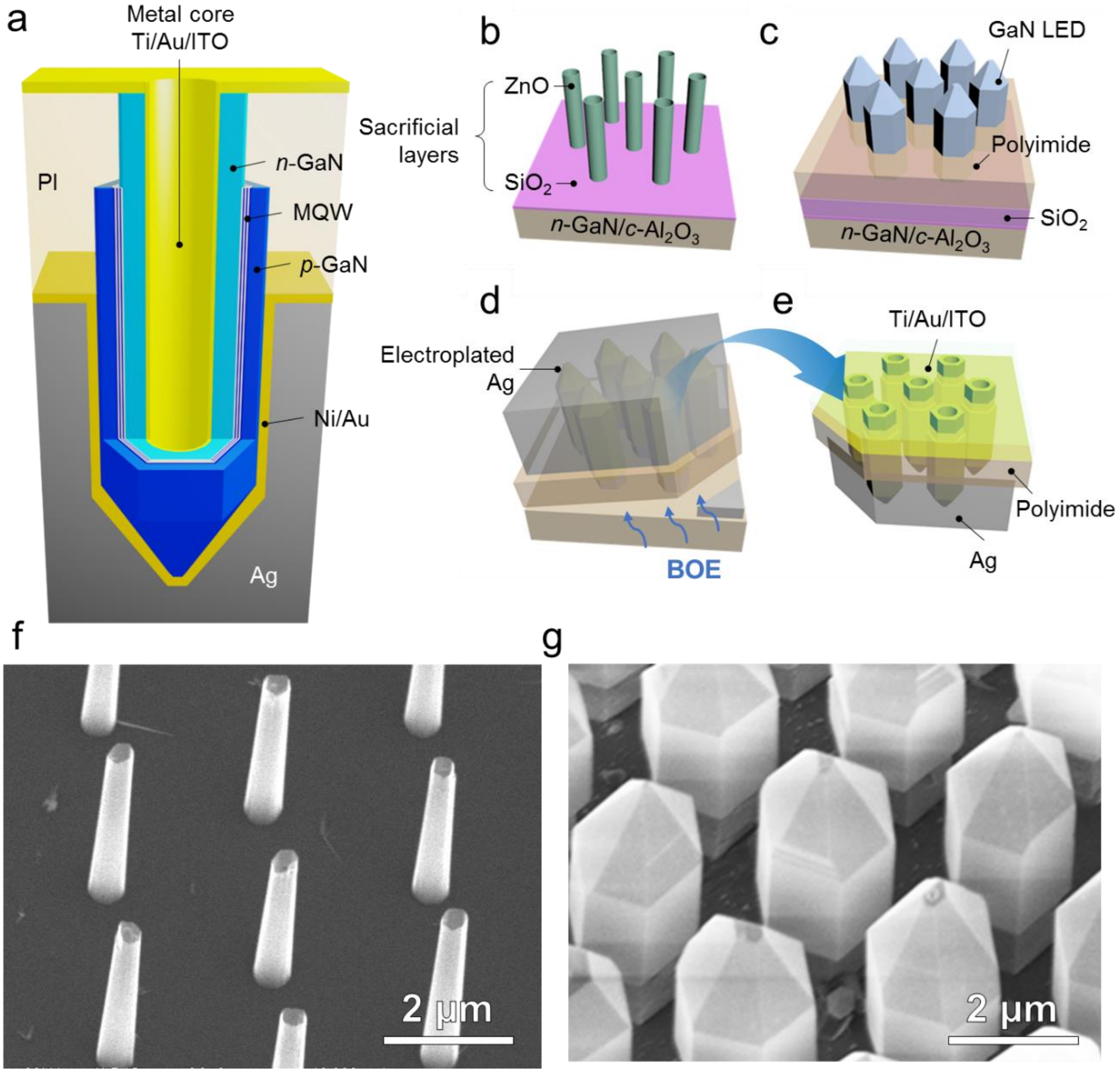

Figure 4.18. Schematic illustration of the steps required to fabricate metal-cored microtube LEDs. (a) Overall structure of the metal-cored microtube LEDs, with Ti/Au/indium tin oxide (ITO) layers filling the inner shell of the *n*-GaN microtubes, and Ni/Au and Ag layers covering the *p*-GaN layer of the LED. (b) Selective-area metal−organic vapor-phase epitaxy growth of ZnO microtube arrays on SiO_2-masked *n*-GaN/*c*-Al_2O_3 substrates. (c) Coaxial coating of the *p*-GaN layers with *u*-GaN/indium gallium nitride (*u*-$In_xGa_{1-x}N$) multiple quantum wells and *n*-GaN layers on the ZnO microtubes and formation of polyimide layers. (d) Lift-off of the GaN/$In_xGa_{1-x}N$ microtube LED array structure from the substrate after electrochemical deposition of Ag layers. (e) Deposition of the ITO/Ti/Au *n*-electrodes after upside-down transfer of the lifted-off microtube

LED array structure on foreign substrates. (f) Tilted SEM images of ZnO microtube arrays and (g) GaN/$In_xGa_{1-x}N$/ZnO microtube LED arrays on *n*-GaN/*c*-Al_2O_3 substrates.

The procedure for making metal-cored coaxial microtube LEDs is illustrated in Figure 4.18. First, we prepared coaxial GaN/$In_xGa_{1-x}N$/ZnO microtube arrays on *n*-GaN-coated aluminum oxide (*c*-Al_2O_3) substrates. SA-MOVPE was used to grow both position- and size-controlled ZnO microtube arrays on the *n*-GaN/*c*-Al_2O_3 substrates. The substrates were coated with 100 nm thick silicon dioxide (SiO_2) growth mask layers patterned with holes, which are schematically illustrated in Figure 4.18(b). The corresponding tilted scanning electron microscopy (SEM) image in Figure 4.18(f) shows that the diameter, height, and period of the regular hexagonal ZnO microtube arrays are 1.0, 5.5, and 4.0 μm, respectively. Here, the ZnO microtubes and SiO2 mask layer acted as sacrificial layers, which were later selectively etched after the epitaxial growth and device fabrication of GaN/$In_xGa_{1-x}N$ coaxial microtube LEDs. After the preparation of the ZnO microtube arrays, the ZnO microtubes were heteroepitaxially coated with Mg-doped *p*-GaN, *u*-$In_xGa_{1-x}N$/*u*-GaN multiple quantum wells (MQWs), and Si-doped *n*-GaN layers. The regular arrays of GaN/$In_xGa_{1-x}N$/ZnO microtubes have clearly defined hexagonal facets, as shown in the SEM image in Figure 4.18(g). After being coated, the diameter of the microtubes increased to 3 μm. To activate the Mg acceptors in the *p*-type semiconductor layers, the samples were rapidly annealed at 650 ℃ for 5 min in a N_2 atmosphere to activate Mg acceptors in the *p*-type layers.

The GaN/$In_xGa_{1-x}N$/ZnO microtube LED arrays were fabricated by forming ohmic metal contacts between the coaxial microtubes, as illustrated schematically in

Figure 4.18(c). To form continuous *p*-electrodes and spatially isolate the *p*- and *n*-electrodes, the gaps between the microtubes were filled by coating the entire structure with a 3 μm thick polyimide layer and curing it at 300 °C in a N_2 atmosphere. To expose the top *p*-GaN surface of the microtubes to the air, oxygen plasma was used to remove the polyimide coated on the top surface of the microtubes. The *p*-contact electrodes were made by depositing semitransparent Ni/Au (10/10 nm) layers with a pad size of 50 × 50 μm^2 onto the top surface of the *p*-GaN, which covered 160 microtube LEDs. The *n*-contact electrodes were made by depositing Ti/Au (30/40 nm) contacts onto an *n*-GaN layer that had been exposed to the air by removing the SiO_2 masking layer with a buffered oxide etchant (BOE). The device characteristics were enhanced by reducing the Ohmic contact resistances by post-annealing the LEDs in air for 5 min at 400°C. More detailed descriptions of how to prepare the materials[49, 63] and make the LEDs can be found elsewhere.[26]

To enable the inner shell of the metal-cored microtube LEDs to be filled, the GaN/$In_xGa_{1-x}N$/ZnO microtube LED arrays were lifted-off the original substrate and transferred upside-down onto a carbon-tape-coated polyimide film. Before the lift off, we deposited Ni/Au (10/10 nm) onto the entire top surface of the devices and rapidly annealed the metal layers for *p*-contact electrodes. Then, a micrometer-thick layer of Ag was electrochemically deposited onto the Ni/Au electrodes, as shown in Figure 4.18(d). To strengthen the adhesion between the electroplated Ag layer and the microtube LEDs, the LEDs were annealed in air at 400 °C for 5 min. The devices were then immersed in BOE to remove the underlying sacrificial ZnO microtubes and SiO_2 layer. After a few hours, the ZnO microtubes and SiO_2 layer were completely removed and it was clear that the entire structure had lifted-off from the *n*-GaN/*c*-Al_2O_3 substrate. After the structures were rinsed in deionized water, they were transferred upside-down onto a polyimide film coated with carbon tape.

In the final step, we made the metal cores, which were contained by the nitride semiconductor microtubes. Before making the metal core electrodes, we visualized the upside-down flipped surface of microtube LEDs embedded in a polyimide layer from above using SEM. The resulting image is shown in Figure 4.19(a). We can clearly see the cylindrical inner shells of the GaN/$In_xGa_{1-x}N$ microtubes, which had a diameter of 1 μm. We then deposited semitransparent Ti/Au (2/2 nm) layers inside the nitride tubes to form the metal core. An electron-beam evaporator was used for the deposition. The Ti/Au layers were coated with a 1 μm indium tin oxide (ITO) layer, which was made by RF magnetron sputtering deposition. A pad size of the Ti/Au/ITO electrodes was 50 × 50 μm^2. The *n*-contact electrodes were then annealed in air at 300 °C for 5 min to reduce the Ohmic contact resistance. The transmittance of annealed Ti/Au (2/2 nm) layers was greater than 80% for the wavelength range of 370−570 nm. Figure 4.19(b) shows the surface morphology of the flipped microtubes after the deposition of the Ti/Au/ITO layers. Comparison of Figure 4.19(a,b) shows that the diameter of the inner shell decreased from 1.0 to 0.4 μm, indicating the formation of a metallic core inside the nitride semiconductor microtubes.

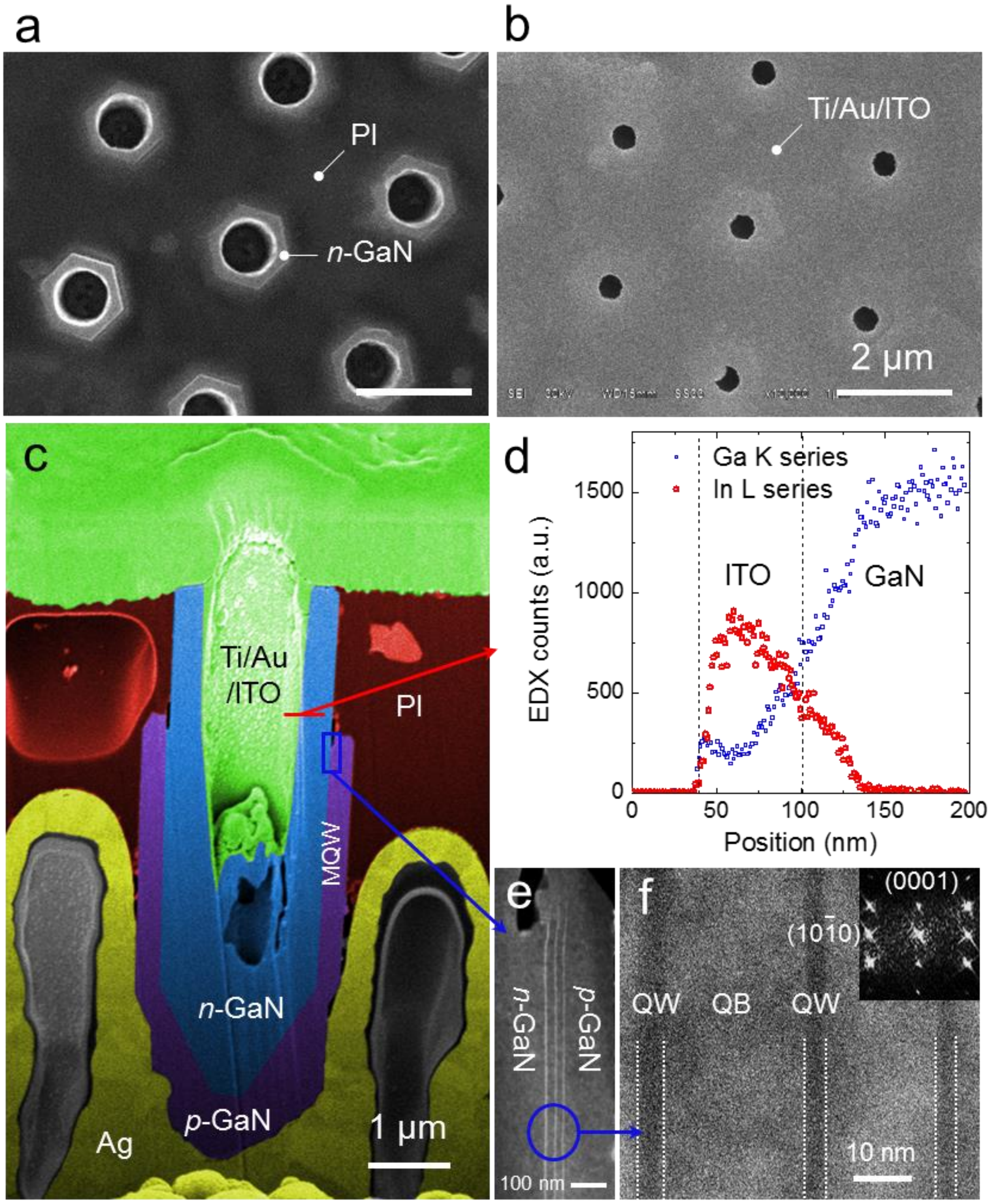

Figure 4.19. SEM image from above of the light emitting diode array after it has been transferred upside-down on foreign substrates (a) before and (b) after the deposition of the Ti/Au/ITO layers. Cross-sectional structure of the metal-cored microtube LED structure shown (c) by a false-colored SEM image, with the SEM configured in the backscattered electron detector mode to show the ITO, polyimide (PI), *n*-GaN, *p*-GaN, and Ag layers indicated with green, red, blue, purple, and yellow, respectively. (d) Energy-dispersive X-ray spectroscopy line profile showing the In and Ga composition on the inner shell of the metal-cored

microtube LED. The In and Ga composition represent ITO and GaN, respectively. The scanned region is indicated by a solid red line in (c). (e) Scanning transmission electron microscopy image near the $p{-}n$ junction of the upright sidewall of a microtube LED, which is the region marked by a circle in (c). (f) High-resolution TEM image of an MQW taken along a direction of $[\bar{1}2\bar{1}0]$. The inset shows the fast Fourier transform pattern of a wurtzite GaN crystal obtained from (f).

To confirm that the structure of the metal core had been formed as expected, its cross section was analyzed by SEM. The SEM was configured in backscattered electron detector mode to enable us to distinguish materials with different atomic numbers, meaning that the ITO, *n*-GaN, *p*-GaN, polyimide, and Ag layers could be distinguished. These are colored in green, blue, purple, red, and yellow, respectively, in Figure 4.19(c). From this SEM image, it is clear that the metal core has been successfully deposited in the inner shell of the *n*-GaN microtube. Additionally, we can see that the polyimide spacer has filled the gaps between the *n*- and *p*-electrodes.

The chemical composition and crystal quality of the metal-cored GaN/$In_xGa_{1-x}N$ microtube LEDs were further analyzed using an energy-dispersive X-ray spectroscopy equipped scanning transmission electron microscopy system (EDX-STEM) and high-resolution TEM (HR-TEM). To directly confirm the presence of the metal core inside the microtube LEDs, the EDX line profile near the inner shell of the microtube LEDs was measured. The scanning position is marked with a solid red line in Figure 4.19(a). The EDX line profile in Figure 4.19(d) indicates indium L characteristics, revealing the ITO layer inside the inner shell of the microtube. The thickness of the topmost parts of the sputter-deposited ITO layers was 1 μm, but at the position indicated, the thickness of the ITO layers deposited inside the microtube was only 50 nm. The thickness of the ITO layer gradually decreased as the distance from the open end of the tube increased; near the opening, it was 100 nm, whereas near the bottom, the thickness had reduced to 4 nm.

Scanning TEM and HR-TEM images, shown in Figures 4.19(c) and (d) were also used to analyze the coaxial LED structure. The STEM image in Figure 4.19(e) shows well-defined three-period MQWs between the *p*- and *n*-type GaN layers. As shown in the HRTEM image in Figure 4.19(f), the MQW layers consisted of 5 nm $In_xGa_{1-x}N$ quantum wells and GaN quantum barriers that were 25 nm thick. EDX point analysis estimated the x value to be 0.07. The STEM images also revealed that the thickness of *n*- and *p*-GaN layers coated on the sidewalls was 300 and 140 nm, respectively. The fast Fourier transform pattern obtained from the HR-TEM image in the inset of Figure 4.19(f) shows the high crystallinity of a wurtzite GaN crystal.

The $In_xGa_{1-x}N$/GaN MQW layers were sharply defined and clearly visible along the entire sidewalls of the microtube, but the layers became blurred near the end of the *p*–*n* junction, as shown in Figure 4.19(e). The unclear formation of MQW layers at this position indicates that the layers with different chemical composition could not be clearly distinguished; thus, the quality of the *p*–*n* junction cannot be ensured in this region. As such, this region is suspected as the dominant leakage current path in the microtube LEDs.

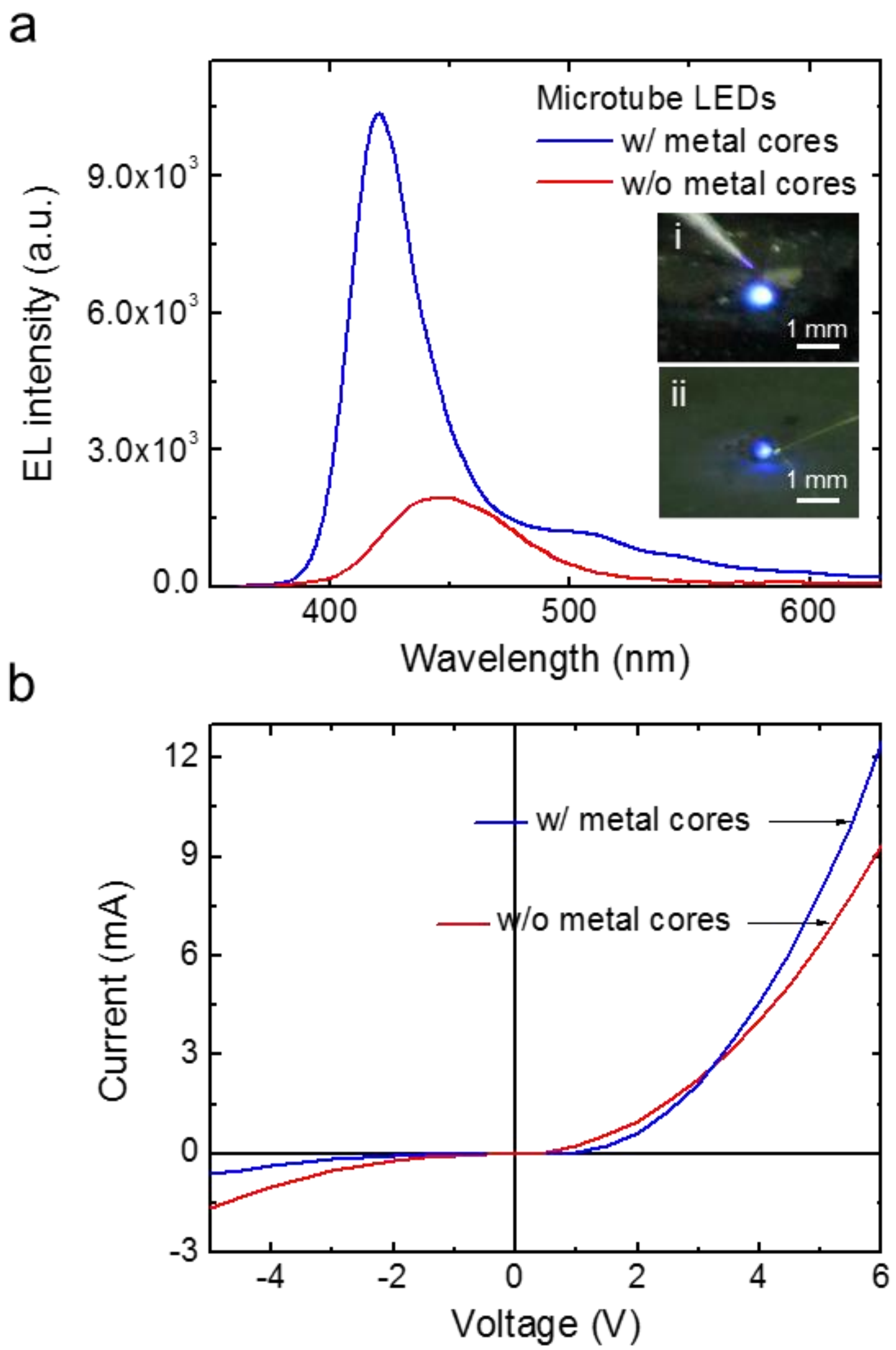

Figure 4.20. Characteristics of the standard and metal-cored microtube LEDs: (a) EL spectra and (b) current–voltage characteristic curves. The inset of (a) shows magnified EL images of (i) a metal-cored microtube LED array and (ii) a standard microtube LED array.

Comparison between the electroluminescence (EL) of the metal-cored (inset i) and standard (inset ii) LED arrays is shown in Figure 4.20. The visible blue light emitted by the LEDs was bright enough to be seen by the unaided eye under normal room illumination. In both cases, the EL spectra were obtained using a bias voltage of 8.0 V. The intensity of the EL emissions of the metal-cored microtube LEDs was nearly 4 times larger than that of the standard microtube LEDs. The increase in output power may be attributed to the improved current spreading characteristics arising from the presence of the metal core. The electroplated Ag *p*-electrode layer and Ti/Au/ITO *n*-electrode layers may improve the reliability of the electrodes, which would contribute to an increase in the intensity of the EL emissions.

In the EL spectrum of the standard microtube LEDs (before they were lifted-off from the substrates), there was a single emission peak at 446 nm, with a full width at half-maximum (fwhm) value of 64 nm. The EL spectrum of the metal-cored microtube LED had a dominant emission peak at 420 nm, with a fwhm of 35 nm. There was also a broad shoulder near 500 nm, covering a spectral range from 400 to 600 nm. This change in the EL spectrum indicates that the insertion of the metal core modified the current-spreading characteristics of the LED array, and that more MQW regions were used for light emission. We base this speculation on the fact that the indium composition of 3D nanostructured LEDs typically varies spatially over the GaN/$In_xGa_{1-x}N$ MQWs,[68] leading to different EL color emissions on each segment.[3, 61] The current spreading in LEDs with a range of architectures, with and without metal cores, will be discussed in detail with computational models in Figure 4.21.

In addition to the EL characteristics, we compared the current−voltage ($I-V$) characteristic curves of the devices in Figure 4.20(b). To plot these results, averages from five different devices are used. Clear improvements in the $I-V$ characteristics of the microtube LEDs were made by the addition of the metal cores. These include better rectifying behavior at 2.5 V, a larger forward bias current for voltages above 3.0 V, and reduced reverse bias leakage current. The average resistance of the metal-cored LEDs decreased from 400 to 220 Ω. The metal-cored microtube LEDs were 2.8 times more efficient than the microtube LED without metal cores.

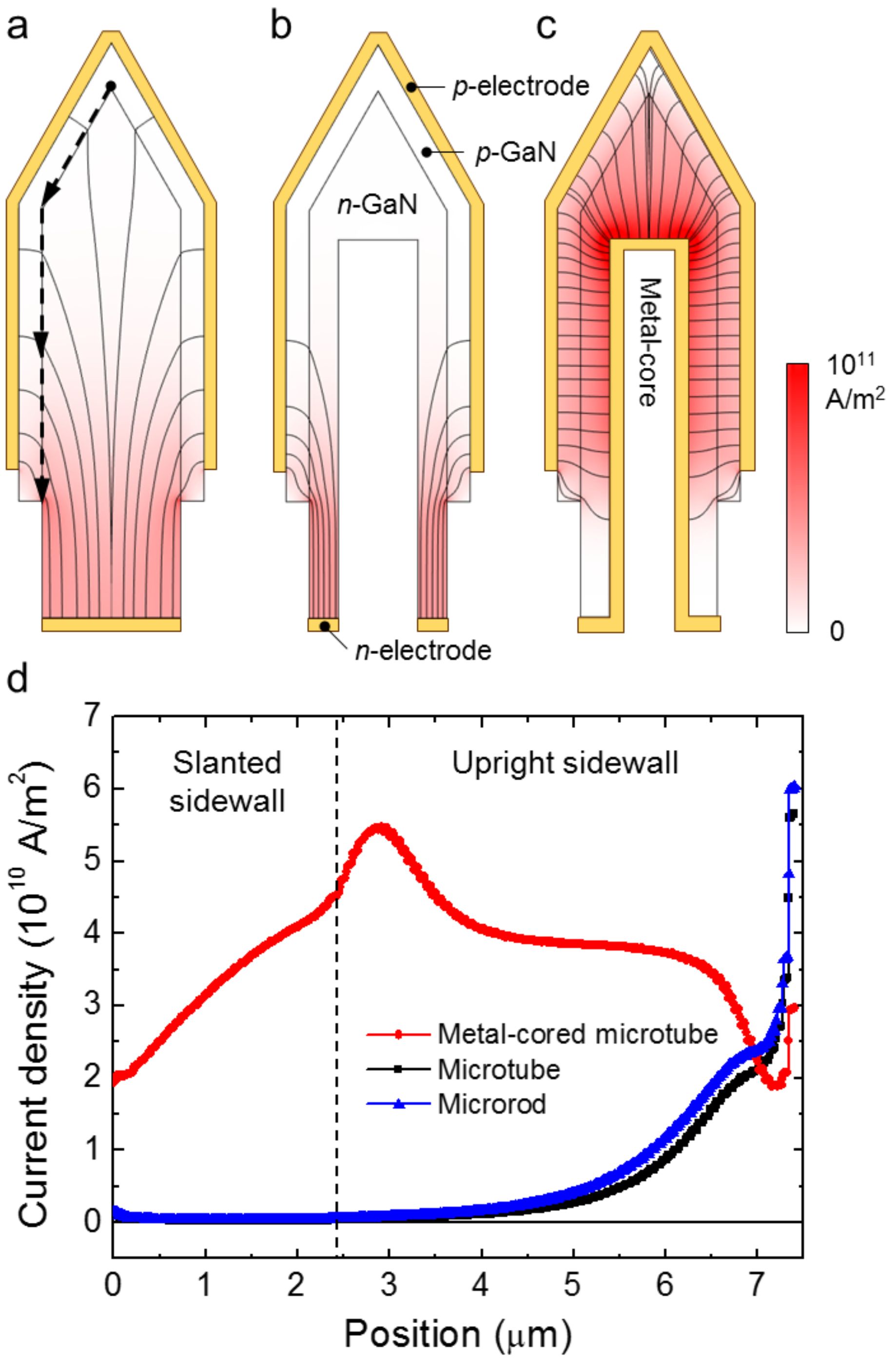

Figure 4.21. Current-spreading characteristics of a coaxial *p*−*n* junction with microrod and microtube, with and without metal-core architectures. The spatial distribution of the current density inside the (a) microrod, (b) microtube without a metal core, and (c) microtube with a metal core. The intensity of the red color represents the current density, increasing as the current density increases. The *p*- and *n*-type ohmic electrodes around the microrods and microtubes are indicated with the yellow color. (d) Current density at the *p*−*n* junction as a function of distance, starting from the tip of the structure.

We used computational modeling techniques to investigate the cause of the improved LED characteristics described above. We modeled the current-spreading characteristics of coaxial *p*−*n* junction GaN microrods and microtubes with and without metal cores. Figures 4.21(a−c) shows the electric current flow through the cross section of a coaxial *p*−*n* junction GaN microrod, microtube, and metal-cored microtube architectures, respectively. The streamlines in the figures represent the current flow, and the intensity of the red color is proportional to the current density. The yellow colored areas indicate ohmic metal electrodes around the microrod and microtube, which are forward biased at 5.0 V. Additionally, the current density passing through the *p*−*n* junction in each case, indicated by the dotted line in Figure 4.21(a), is plotted against the position along the structure in Figure 4.21(d).

First, we examined the current-spreading characteristics of microrods and microtubes without metal cores. As shown in Figures 4.21(a), (b), and (d), the current density decreased along the length of the structure. This result indicates that, although the active areas for light emission are larger in 3D nanostructure LEDs than in thin film LEDs, not all of the active area is used for light emission. The current injection area can be slightly increased by either increasing the conductivity of the *n*-GaN or decreasing the conductivity of the *p*-GaN. However, further investigations, shown in Figure 4.22, indicated that the current-spreading characteristics of the microrod and microtube could not be significantly modified by varying the conductivity of the *n*-GaN and *p*-GaN. The presence of the metal core significantly altered the current-spreading characteristics of the coaxial $p-n$ junction GaN microtubes. The current density increased 2-fold, increasing the current level along the entire length of the microtube, as can be seen in Figures 4.21(c) and ,(d). The enhancement in the current flowing through the metal-cored microtubes can be attributed to the increased use of the active $p-n$ junction area and the decreased spatial separation between *p*- and *n*-electrodes.

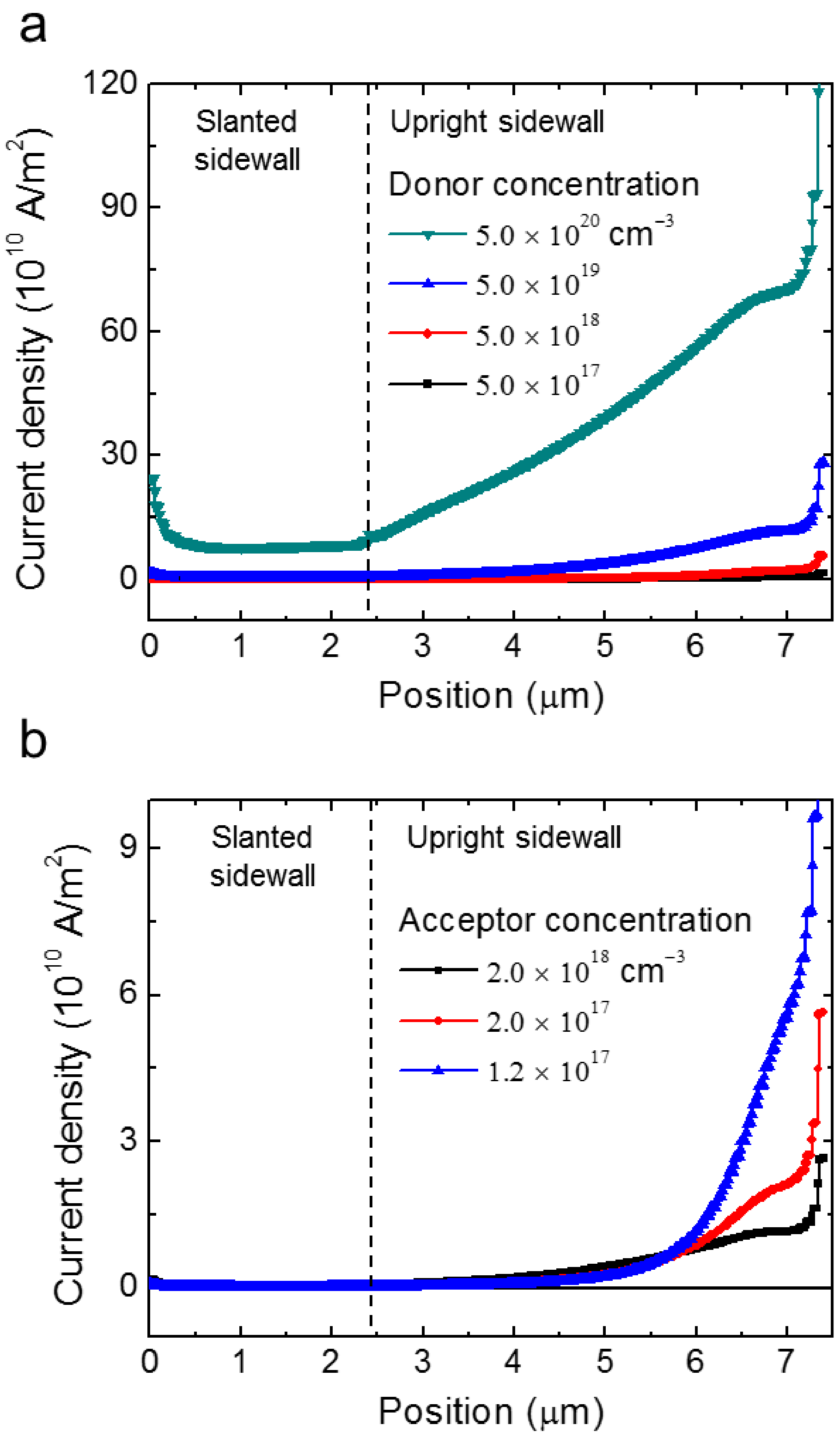

Figure 4.22. Carrier concentration dependence of the current spreading characteristics in a coaxial *p*−*n* junction microtube without metal core. The current density at the *p*−*n* junction as a function of distance depending on a) the donor concentration of *n*-GaN microtube and b) the acceptor concentration of *p*-

GaN shell layer.

Based on the current-spreading model of the microtubes, we present a possible explanation with regard to the difference in the leakage current levels between the metal-cored and standard microtube LEDs (see Figure 4.21(b)). As shown in Figure 4.21(d), the microtube LEDs without metal cores had the highest current density near the end of the $p-n$ junction, the region of the suspected leakage current path. When metal cores were inserted inside the microtube LEDs, the current density increased along the entire sidewalls but decreased only near the end of the $p-n$ junction. Because the current passing through the suspected leakage current path decreased, metal-cored microtube LEDs showed leakage current levels lower than those of standard microtube LEDs. This leakage current path also produced a difference in the turn-on voltages of the two devices. Through the leakage current path located near the end of the $p-n$ junction, current flowed from the lower bias voltage that was below the turn-on voltage of the other well defined $p-n$ junction in the sidewalls. Hence, the turn-on voltage of standard microtube LEDs appeared lower than that of metal-cored microtube LEDs.

The improved EL property of metal-cored microtube LEDs (see Figure 4.20(a)) can be attributed to the significant increase in the use of the active regions for light emission, as demonstrated by the current-spreading model in Figure 4.21. Additionally, we think that the modified distribution of current density in the metal-cored microtubes also played a critical role in enhanced EL characteristics, assuming the existence of a leakage current path at the end of the $p-n$ junction in the microtube LED; in this region of the microtube LED, the $p-n$ junction end appeared to be of relatively low quality, as indicated by the unclear formation of MQW layers. Accordingly, in addition to the leakage current issue here, poor EL characteristics can be expected in this region, as well. For metal-cored microtube LEDs, the current density increased along the well-formed $p-n$ junction in the sidewalls but decreased only in the low-quality region near the $p-n$ junction end; thus, enhanced EL characteristics were observed.

We demonstrated that the addition of metal cores to microtube GaN/$In_xGa_{1-x}N$ LED arrays enhances their performance. The results were obtained experimentally and then investigated in more detail using computational modeling. In comparison to the unmodified GaN/$In_xGa_{1-x}N$/ZnO microtube LED arrays, the devices with metal cores emitted light more brightly and had a higher forward bias current and a lower reverse bias leakage current. By inserting metal cores inside the 3D LED nanoarchitectures and understanding their current-spreading characteristics, we can create devices that have a larger active area for light emission and higher efficiency.

4.6. Summary

In summary, ultrathin and individually addressable nanorod device arrays were demonstrated using position- and morphology-controlled ZnO nanorod arrays grown on large-area graphene layers. It was possible to individual address each nanorod device in the array and measure their electrical characteristics. Furthermore, the ultrathin nanorod device array on graphene layers operated reliably in freestanding and flexible form without observable degradation of the device characteristics. Based on this device concept, high-spatial-resolution nanorod UV photodetector and pressure sensor applications were also demonstrated as well. Moreover, blue LED was demonstrated using position- and morphology controlled GaN/ZnO coaxial nanorod heterostructure arrays on CVD graphene layers. Metal-cored GaN microtube LED was demonstrated as one practical solution to significantly improve the performance of the nanostructured LEDs. More generally, we believe that this approach provides a general and rational route for developing many different ultimate-density inorganic electronics and optoelectronics in ultrathin and ultraflexible forms.

Microstructure light-emitting diode arrays on graphene substrate for display applications

5

5.1. Introduction

Semiconductor microstructures, such as micro-thin films, microdisks and micropyramids, based devices are expected to be realized in more foreseeable future than semiconductor nanostructures based devices, since the physical properties of semiconductor microstructures are more similar to conventional thin films than those of nanostructures and well-established semiconductor processing technologies can be directly applied to the microstructures.[69] By integrating semiconductor microstructures on graphene layers, as shown in Figure 5.1, the advantages of each material would be synergistically combined, thereby high performance, flexible, and transferrable electronic and optoelectronic devices can be realized.[16, 37]

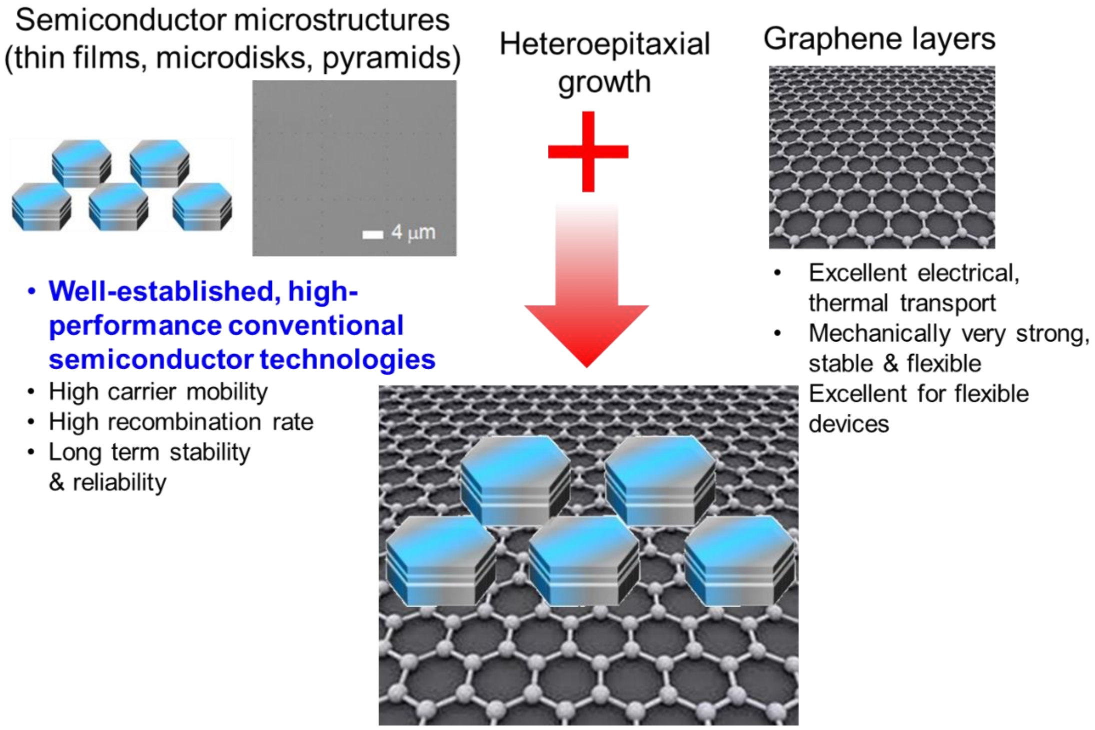

Figure 5.1. Schematic illustration of semiconductor microstructures

heteroepitaxially grown on graphene layers.

This chapter will present the micro-LED and microdisplay applications of semiconductor microstructures. Ultrathin and flexible microdisplay will be demonstrated using GaN microdisk LED arrays grown on graphene microdots. For the full-color microdisplay applications, variable color LEDs are also demonstrated using multifacetted GaN microdonuts and micropyramids.

5.2. GaN microdisk light-emitting diode display fabricated on graphene

Microdisplay with high resolution, brightness, and efficiency with long-term stability and reliability are highly required for advanced display technologies.[70] Inorganic semiconductors LEDs best suits this purpose because they can emit very high density of light from a small area and they have very high efficiency and long-term stability.[71, 72] To use inorganic LEDs for display applications, various lift-off and transfer techniques of inorganic thin films grown on single crystal substrates, such as sapphire or Si, were developed.[69] However, achieving display devices using inorganic semiconductor thin films is still very challenging because of the limited size and high manufacturing cost of the single crystal substrates, as well as the complicated processes required for lift-off and assembly. To resolve this problem, growths of inorganic semiconductor nanostructures and thin films on graphene substrates have recently been proposed, since graphene has great scalability and extremely thin layered hexagonal lattice structure as an excellent substrate for GaN growth.[16] Moreover, the inorganic semiconductors prepared on large-area graphene can be transferred easily to or grown on elastic substrates to meet the flexibility demand.[73]In this chapter, we suggest a method of fabricating ultrathin, high-resolution inorganic microdisplay based on individually addressable GaN microdisk LED arrays grown on graphene dots. Most of the GaN microdisks prepared by epitaxial lateral overgrowth on patterned graphene microdots were single-crystalline.[37] Furthermore, the discrete and small microdisk LED arrays in the microdisplay also ensured that stress and strain were minimal under various bending conditions, thereby providing excellent flexibility. Here, we report on the fabrication and EL characteristics of ultrathin and individually addressable GaN microdisk LED arrays grown on graphene dots for microdisplay applications.

5.2.1. Device structure

GaN microdisks were prepared by epitaxial lateral overgrowth on patterned graphene microdots on SiO_2/Si substrates using MOVPE. After preparing the GaN microdisk arrays, *p*-GaN and *u*-$In_xGa_{1-x}N$/GaN multiple quantum well, and *n*-GaN layers were heteroepitaxially grown on the surface of the GaN microdisks.[37] Ultrathin layers composed of GaN microdisk LED arrays on graphene dot were prepared by coating a polyimide layer and lifting-off the entire layers from the substrate. Then, single-walled carbon nanorods (SWCNTs)/Ni/Au and SWCNTs/Ti/Au multiple electrode lines were formed on the top and bottom surface of GaN microdisk arrays in an aligned manner and crossing each other as shown in Figures 5.2(a) and (b). As shown in the SEM image in Figure 5.2(b), the bottom electrode lines were visible through the ultrathin PI films, and the top and bottom electrode lines crossed each other at each microdisk. The SWCNTs embedded metal electrodes were created by dispersing the SWCNTs on both sides of the ultrathin layers, depositing microelectrodes, and patterning exposed SWCNTs by oxygen plasma ashing. SWCNTs were employed to make the electrodes to have better mechanical strength and reliability under stretching and bending of the device.

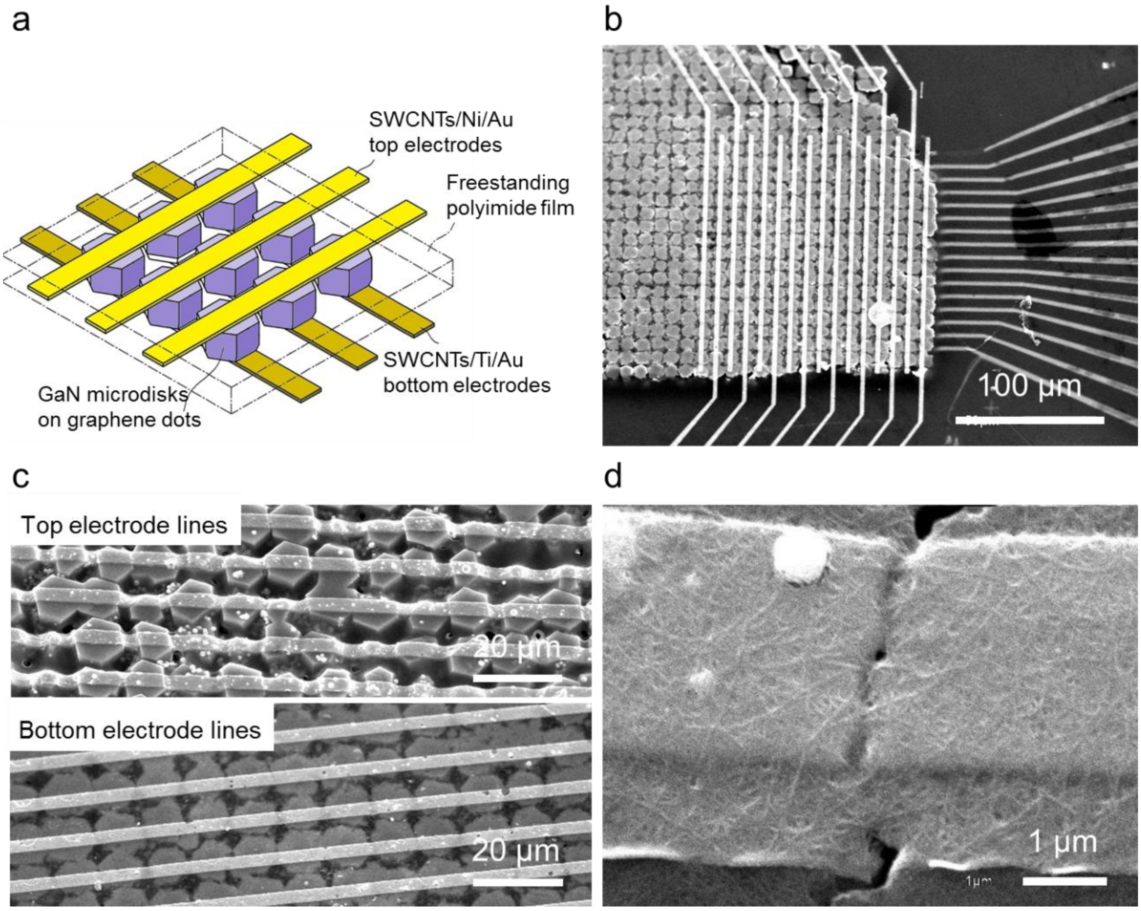

Figure 5.2. Device structure of the individually addressable GaN microdisk LED arrays. (a) Schematics illustration of the device structure. (b) SEM image of the individually addressable GaN microdisk LED crossbar array and (c) top SWCNTs/Ni/Au and bottom SWCNTs/Ti/Au electrode lines on and underneath the GaN microdisk LEDs. (d) SEM image of the SWCNTs embedded Ti/Au electrodes.

Higher magnification SEM images of the device structures are shown in Figures 5.2(c). The tilted SEM image in Figure 5.2(c) shows the top SWCNTs/Ni/Au and bottom SWCNTs/Ti/Au electrode lines formed on the *p*-GaN surface and the underlying *n*-GaN/graphene microdot of the GaN microdisks. Top and bottom electrode lines were precisely aligned with the center of GaN microdisks. As shown in the SEM images in Figure 5.2(d), which was taken before etching the SWCNTs, we can clearly see the SWCNT networks embedded underneath the metal electrodes. The SWCNTs played a critical role in improving the reliability of the electrode lines by bridging the nanoscale gaps or height different observed on the surface of the GaN microdisk arrays.

5.3.2. Device characteristics of individually addressable GaN microdisk LEDs

The 16 by 16 microdisk LED passive matrix array was tested to see whether each microdisk in the array is individually controllable, acting as a unit pixel of the microdisplay. Individual pixel, a microdisk LED, in the ultrathin microdisk array was measured by making 2-probe contact on the selected pair of top and bottom electrode lines and applying forward bias voltages to the LED. Bright blue light-emission from a single spot in the crossbar array was observed as shown in the magnified EL images in Figure 5.3. As shown in Figure 5.3(a), EL emission was only observed from the microdisk LED that was placed on the crossbar junction where the probed pair of top and bottom electrode lines crossed each other. Whenever the electrical voltage was applied to different pairs of top and bottom electrode lines, EL emission spot was observed from different position in the array. This clearly demonstrates that individual microdisk LED can be used as a pixel of the microdisplay. In the magnified EL images in Figure 5.3(b), some pixels showed additional EL emission spot near the intended position. This might be due to the merging between GaN crystals during the ELOG growth process or the defects in the device structures. We believe that these observed flaws of the device can be eliminated by improving the uniformity in material and device structures.

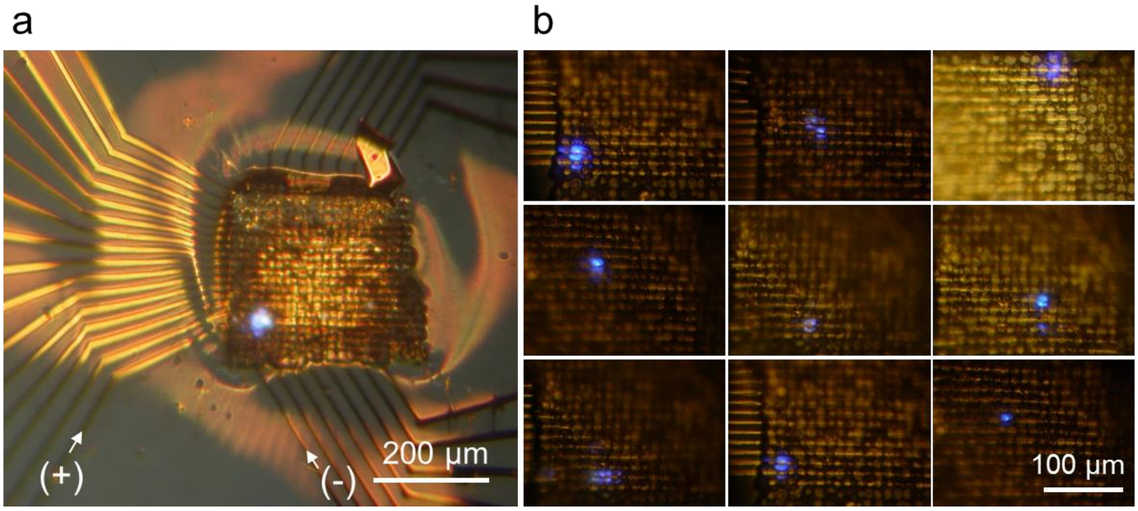

Figure 5.3. Magnified EL images of the individually addressable microdisk LED microarrays. (a) Lower and (b) higher magnification optical microscope EL image of the device under different probing positions

The electrical and optical characteristics of the individually addressable GaN microdisk array on graphene dots were investigated by measuring their *I*–*V* curves and EL characteristics. Figure 5.4 shows the *I*–*V* curve and integrated EL intensities of a single GaN microdisk LED in the microdisplay array. Above the turn-on voltage, the current began to increase rapidly with the bias voltage, resulting in increased light emission intensity.

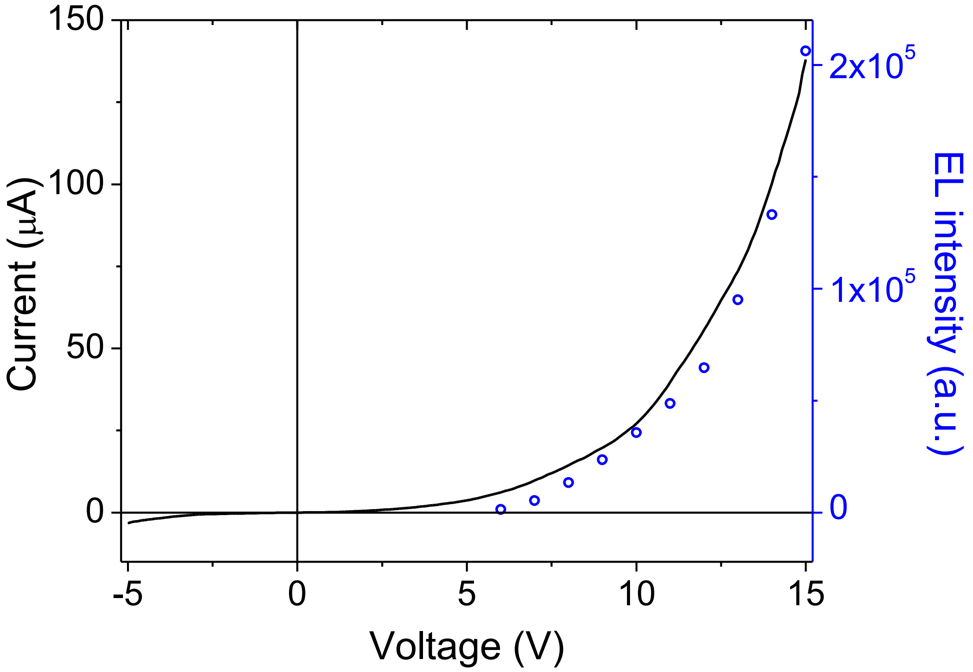

Figure 5.4. ***I*–*V* curve and voltage dependent EL intensity of a single GaN microdisk LED within the array.**

We further investigated the light emission characteristics of the microdisk LED by measuring their EL spectra at various bias voltages. As shown in Figure 5.5, dominant EL peak was observed near 440 nm. By increasing the bias voltage from 6 to 15 V, the dominant EL peak position changed from 459 to 439 nm. In addition to the dominant blue peak observed near 440 nm, long tail extended above 580 nm and small green EL peak was observed near 550 nm. The observed change in EL peak position and broad spectral EL emission observed from the microdisk LED may presumably result from non-uniform indium compositions and thicknesses of the MQW layers coated on the multifaceted GaN microdisks.[37]

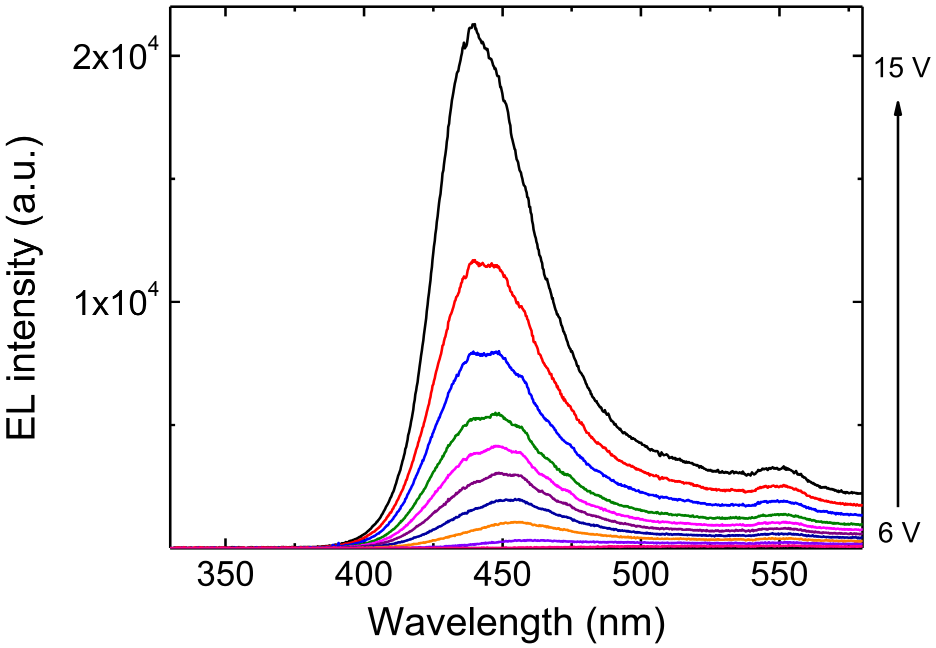

Figure 5.5. Power dependent EL spectra of a single GaN microdisk LED within the array.

The effect of bending on the microdisk LED array was further investigated by obtaining *I*–*V* and EL characteristics at various bending radii. Figure 5.6 shows photographs (see Figure 5.6(a)) and corresponding *I*–*V* curves (see Figure 5.6(b)) at bending radii of 10, 3, and 1 mm. The *I*–*V* curves obtained at different bending radii exhibited almost identical behavior regardless of the bending radii. This suggests that no serious mechanical stress, damage, or fracture occurred at the electrodes or the junctions between the GaN microdisks during the bending test. In addition to the *I*–*V* curves, EL spectrum of the microdisk LED was measured under different bending radii, as shown in Figure 5.6(c). Although the EL spectra measured at different bending radii showed similar shape, the overall EL intensity increased when the bending radius decreased. This observed change in EL intensity presumably originated from the change in tilt angle of the GaN microdisk LEDs during the ultrathin layer bending, since GaN microstructure LEDs typically have nonuniform angular distribution of EL intensity.

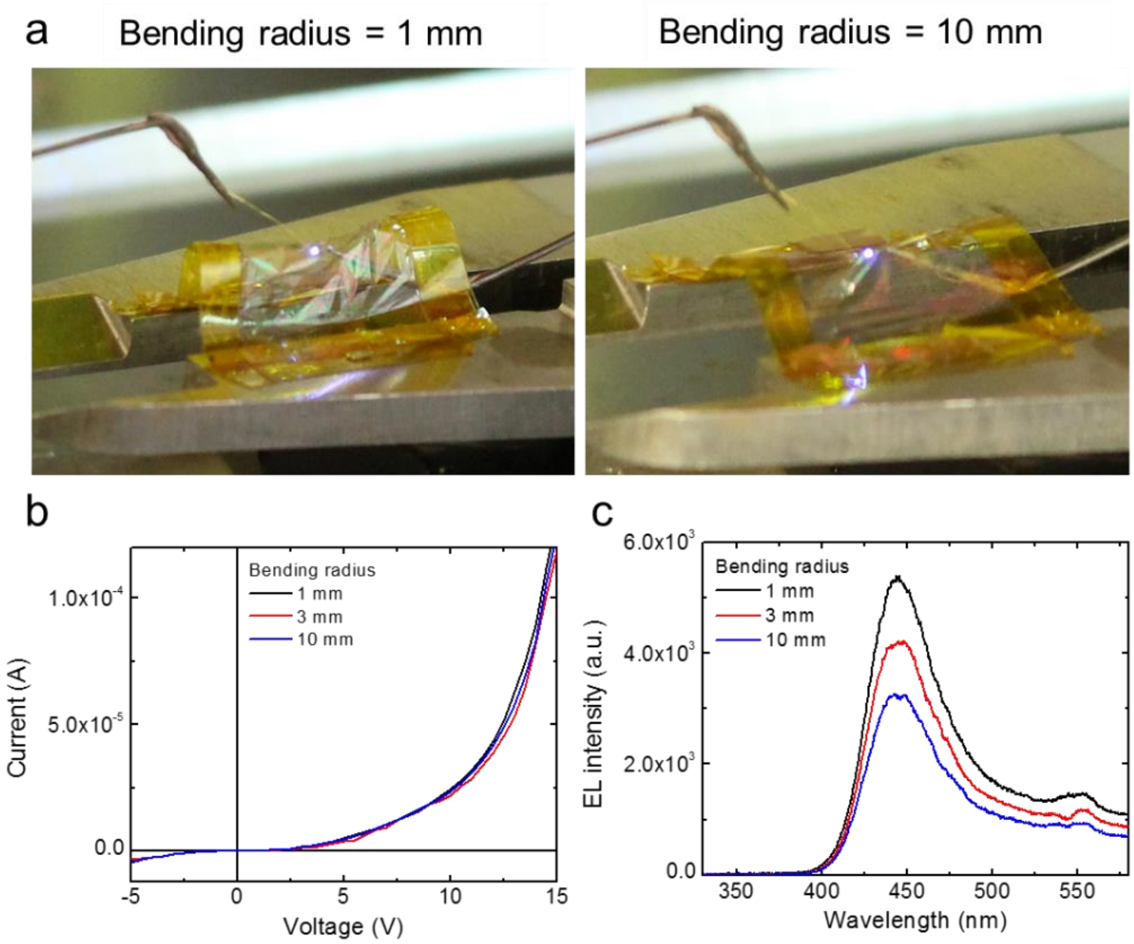

Figure 5.6. Flexibility of the device under various bending radius.

The reliability of the microdisk LED display under continuous operation mode was also investigated. Figure 5.7 shows the current level and integrated EL intensity of the single pixel of the microdisk LED array recorded for 300 s under continuous operation mode. As we can see in this figure, there were no obvious degradation in current level or EL intensity in the device. We believe that this continuous mode operation was possible because the single microdisk LED, that had a size under 9 × 9 μm^2, would consume small power and generate small amount of heat. The SWCNT networks, which are known to have high thermal conductivity, would probably helped the ultrathin device distribute heat generated from a small point.

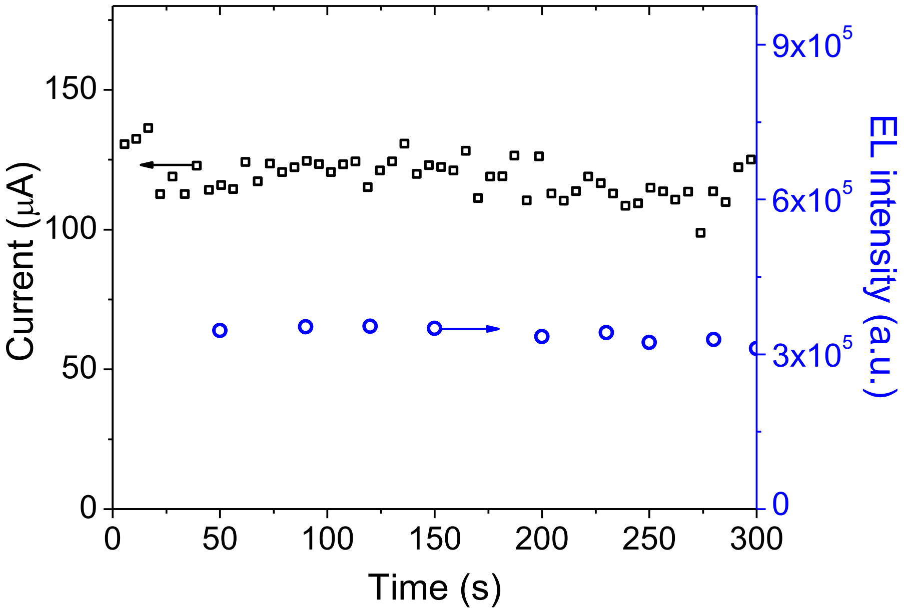

Figure 5.7. Current level and EL intensity of the device measured under continuous mode operation.

5.3. Morphology-controlled GaN nanoarchitecture LED arrays for full-color microdisplay applications

5.2.1. Monolithic multicolor GaN micropyramid LED array

Multiple color LEDs with tunable brightness, monolithically integrated on a single substrate, would enable the fabrication of high-resolution full-color light emitters with high brightness and low power consumption for next-generation mobile device displays.[64, 71, 74-76] Although organic LEDs are already on the market as full color displays, inorganic LEDs generally show much higher light-emitting efficiency and long-term stability and reliability.[72, 77, 78] Nevertheless, little attention has been paid to inorganic LEDs for display applications because it has been very difficult to fabricate inorganic LEDs that emit multiple colors on a single substrate. This problem results mainly from uniform thicknesses and homogeneous compositions of light-emitting quantum well layers for conventional thin film LEDs. Recently, to overcome these problems and to fabricate multicolor inorganic LEDs on a single substrate, three-dimensional multifaceted GaN nano- and micro-structures have been suggested.[61-63] For these structures, $In_xGa_{1-x}N$ layers coated on each facet showed distinct photoluminescence (PL) and electroluminescence (EL) colors, due to the difference in $In_xGa_{1-x}N$ layer thickness and chemical composition.[3, 61] Most of these works achieved these characteristics using the difference in diffusivity and bonding probability of In and Ga adatoms on polar, semipolar, and nonpolar GaN microfacets. This difference created $In_xGa_{1-x}N$/GaN quantum wells with different In composition and $In_xGa_{1-x}N$ quantum well layer thickness on each type of microfacets. However, monolithic multicolor LEDs based on purely semipolar multifaceted nano- and microstructures were not demonstrated so far. GaN LEDs grown on semipolar crystal plane have advantages over conventional LEDs grown on *c*-plane due to the reduced quantum-confined Stark effect (QCSE) which deteriorate the internal quantum efficiency and result in blue shift at a high current injection level.[51] Here, we demonstrate multicolor emission using position and size-controlled semipolar micropyramid GaN LED arrays grown on a single substrate. The GaN nano- and micro-structures were composed of truncated pyramid structures with smaller nanopyramids on their top surface. The origin of the multicolor emissions of the micropyramid LEDs was also investigated using electroluminescence (EL) spectroscopy and scanning transmission electron microscopy (STEM).

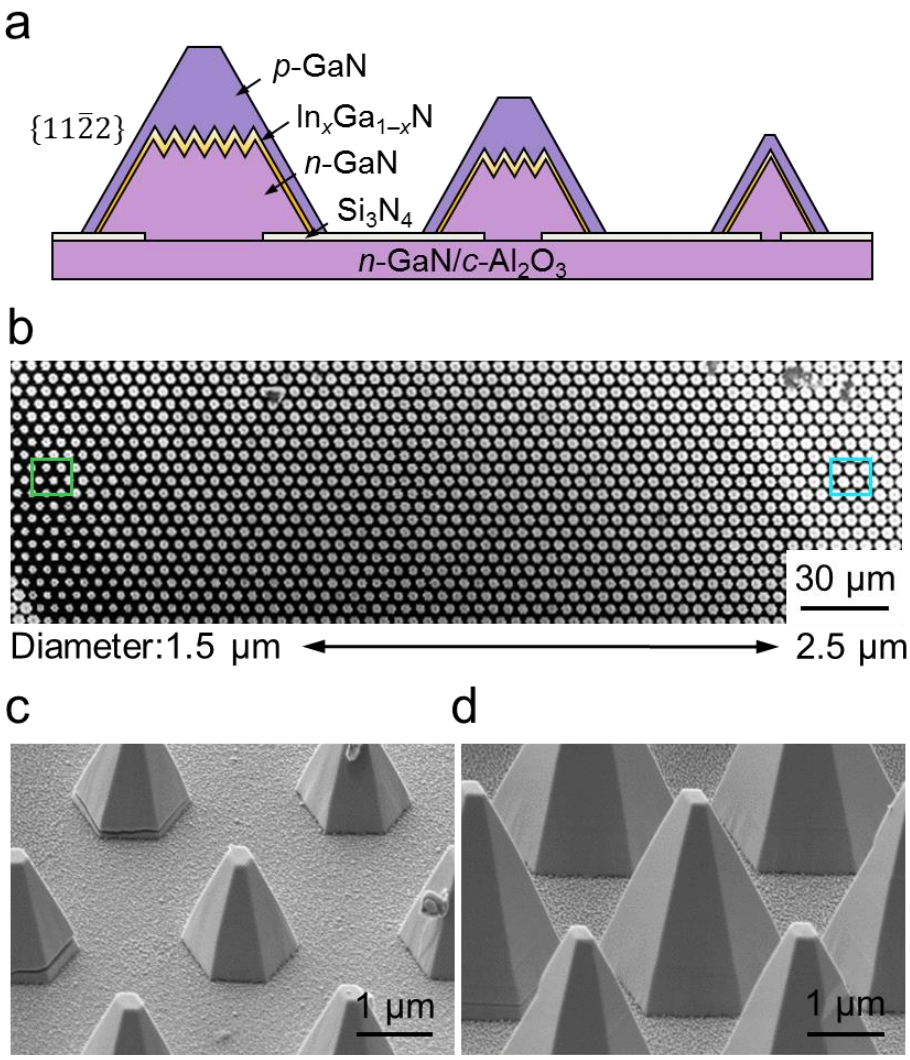

Figure 5.8. Schematics and FE-SEM images of the micropyramids. (a) Schematics of the cross-sectional structure of the micropyramid LEDs. FE-SEM images of the micropyramid LEDs with (b) 1.4 and (c) 2.4 μm diameters. Top-vew FE-SEM image of the micropyramid LED arrays with different sizes ranging from 1.4 to 2.4 μm in diameters.

SA-MOVPE was used to grow both position- and size-controlled semipolar *n*-GaN micropyramid structures on *c*-Al_2O_3 substrates coated with a 5-im-thick *n*-GaN layer. For the selective growth of the GaN microstructures, a Si_3N_4 mask layer with various sizes of holes was prepared on the substrates by conventional *e*-beam lithography and then *n*-GaN microstructures were grown by SA-MOVPE. After the preparation of the GaN microstructure arrays, Mg-doped *p*-GaN, *u*-$In_xGa_{1-x}N$, and Si-doped *n*-GaN layers were heteroepitaxially grown on the entire surface of the *n*-GaN microstructures, as schematically illustrated in Figure 5.8(a). Samples were then rapidly annealed at 650°C for 5 min in a N_2 atmosphere to activate Mg acceptors in the *p*-type layers. The surface morphology of semipolar $In_xGa_{1-x}N$/GaN microstructure LEDs with various sizes are shown using scanning electron microscopy (SEM) images in Figures 5.8(b−d). The diameters of the micropyramid LEDs ranged from 1.5 to 2.5 μm with 4 μm period, whose sizes were determined by the growth mask patterns. Comparing the final diameters of GaN microstructures with the original diameters of hole openings on the Si_3N_4 growth mask, we can know that the microstructure LEDs were laterally overgrown by 0.5 μm.

We investigated the optical characteristics of each size of semipolar microstructure LEDs in a visible range. Figure 5.9(a) shows a magnified photograph of light emission from micropyramid LED arrays. We measured each sizes of microstructure LEDs separately with *p*-electrodes covering $20 \times 50\ \mu m^2$, which typically consist of sixty microstructure LEDs. As shown in Figure 5.9(a), under the same 7 V bias voltage, the micropyramid LEDs with a small diameter of 1.5 μm showed green emission, while the micropyramid LEDs with a bigger diameter of 2.2 μm showed blue light emission. All other micropyramid LEDs, whose diameters ranging from 1.5 to 2.5 μm, showed gradual emission color change from green to blue as the size of the micropyramid LEDs increases.

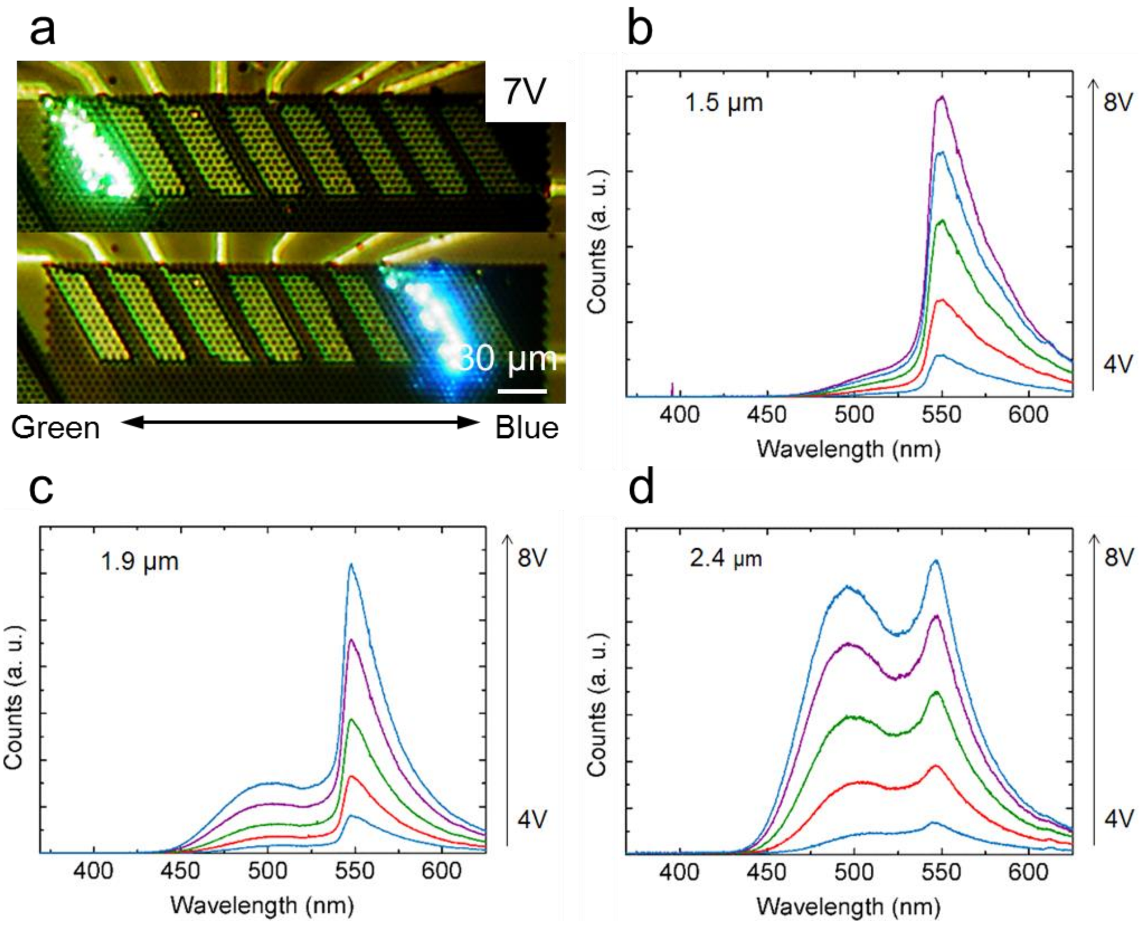

Figure 5.9. EL images of the device. (a) Measured each sizes of micropyramid LEDs with 20 × 50 µm^2 electrodes under 7 V bias voltage. EL spectra of the micropyramid LEDs with different diameters. (b) 1.5 µm (c) 1.9 µm (d) 2.4 µm, respectively. Each EL spectrum curve corresponds to each voltage from 4V to 8V.

The light emission of LEDs were further investigated by measuring their EL spectra at various bias voltages. Figure 5.9 shows EL spectra measured different bias voltages ranging from 4 to 8 V for three different sizes of micropyramid LEDs, each having diameters of 1.5, 1.9, and 2.4 µm, respectively. From theses EL spectra, we can see that micropyramid LEDs have two dominant EL peaks at 490 nm and 550 nm. The smaller micropyramid LEDs with 1.5 µm diameter in Figure 5.9(b) have a single 550 nm dominant EL peak and a small 490 nm peak only as a shoulder. However, as the diameter of the micropyramid LEDs increases to 1.9 μm, we can see a relatively broad 490 nm EL peak which became considerably large as shown in Figure 5.9(b). The micropyramid LEDs with 2.4 μm diameter in Figure 5.9(d) have even larger 490 nm EL peak and their intensity became comparable to the 550 nm EL peak. To summarize, as the size of the micropyramid LEDs increased, the intensity of the broader 490 nm EL peak became relatively larger compared to narrower 550 nm EL peak. From these results, we can now see that the EL color difference between different sizes of micropyramid LEDs occurred because the relative brightness of 550 nm green and 490 nm blue color was different for each size of GaN microstructures. One more thing to note here is that for each size of microstructure LEDs, the shape of the EL spectra did not changed with increasing power, which can be attributed to the reduced QCSE in semipolar facet GaN LEDs. This is different from other multifaceted LEDs that consist of *c*-plane where the shape and color of the EL spectra typically changed with increasing power. In short, each size of microstructure LEDs had a unique color with tunable brightness, which is a highly desirable characteristics of RGB display pixel.

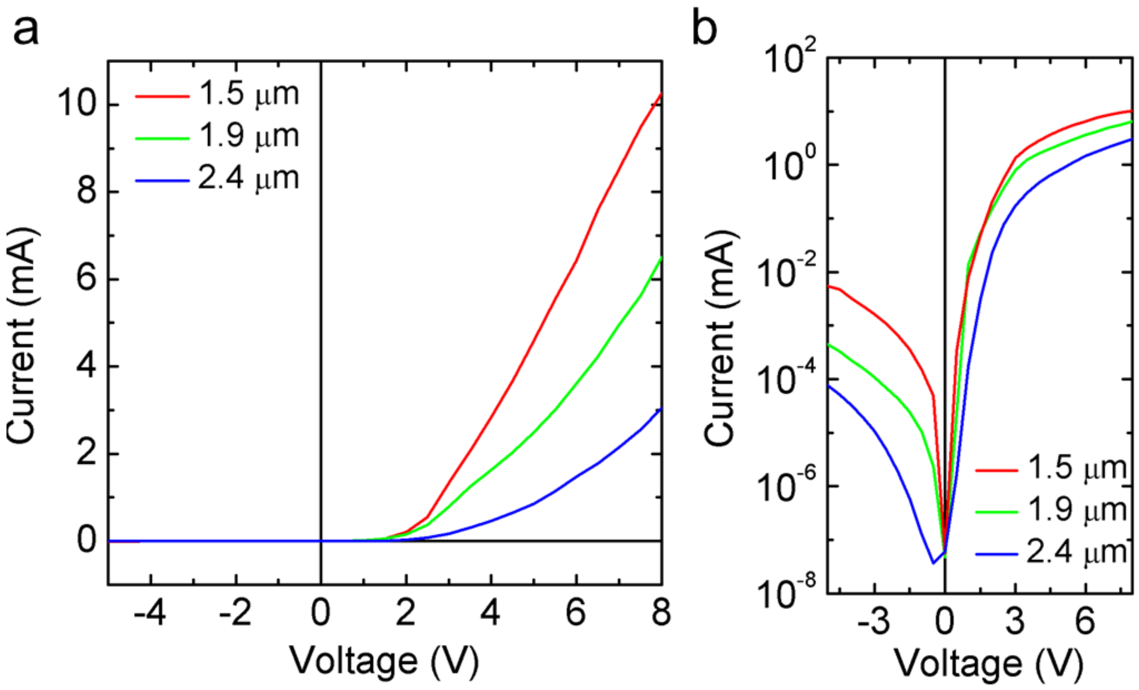

Figure 5.10. *I–V* characteristic of the micropyramid LEDs with different sizes. (a) Linear and (b) log scale plot of the *I–V* curves.

In addition to the optical characteristics, we also measured the current–voltage (*I–V*) characteristic curves of the LEDs to investigate the electrical characteristics of the micropyramid LEDs. The *I–V* characteristics of three different sizes of microstructure LEDs are shown in Figure 5.10. In the *I–V* curves in Figure 5.10(a), all sizes of LEDs showed similar turn-on voltages around 2.5 V. However, bigger micropyramid LEDs showed lower slope which indicates higher resistance of the bigger micropyramid LEDs. Figure 5.10(b) shows the same *I–V* curve of Figure 5.10(a) in logarithmic scale. From this graph, we can see that under 8 V forward bias voltage, the current levels of all sizes of micro LEDs were within the same order, but at –5 V reverse bias voltage, the reverse bias leakage current levels were in clearly different orders. To compare the leakage current levels of different LEDs, we defined a quantity L_{5V} as a ratio of current at +5 V to –5 V. We observed that the biggest 2.4

µm micropyramid LEDs had largest $\boldsymbol{L_{5V}}$ value of 11,000, which means that their current at −5V was 11,000 times smaller than the current flowing at +5V. Other smaller pyramid LEDs with 1.5 µm and 1.9 µm diameter had $\boldsymbol{L_{5V}}$ value of 860 and 5,600, respectively. This means that the bigger micropyramid LEDs with thicker *p*-GaN layer had lower reverse bias leakage current. In comparison, the conventional $In_xGa_{1-x}N$/GaN thin film LED on sapphire fabricated in the same manner showed $\boldsymbol{L_{5V}}$ value of 3,200, which is lower value than our micropyramid LEDs. From this result, we demonstrated for the first time that the leakage current level of nanostructure LEDs can be comparable or even smaller than the conventional thin film LED. For the reverse bias leakage current characteristics, this result is advanced from the previous reports on nanostructure LEDs where they showed $\boldsymbol{L_{5V}}$ values around or below 100.[26, 63, 79]

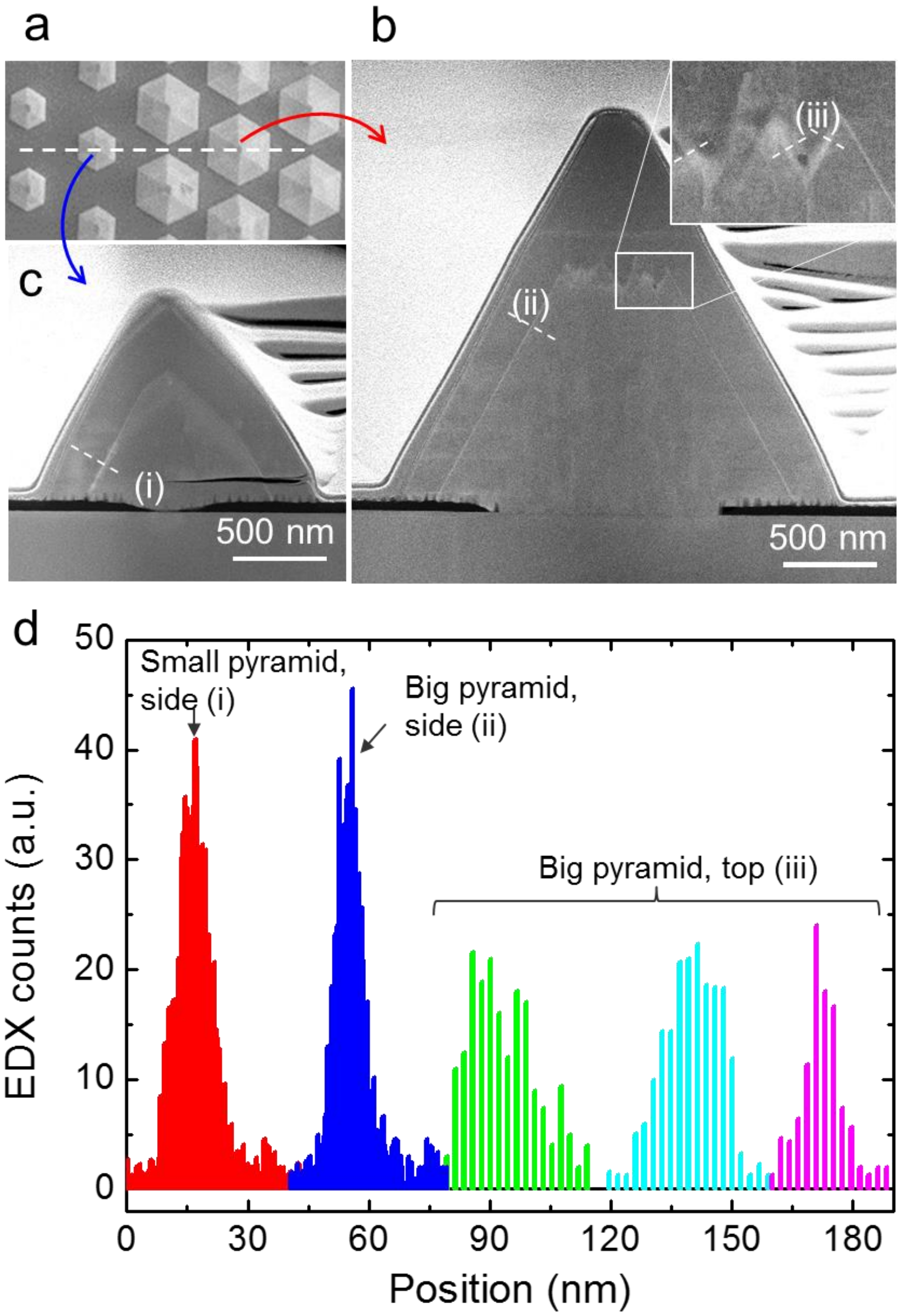

Figure 5.11. STEM-EDS analysis of the chemical composition of $In_xGa_{1-x}N$ layers in two different sizes of micropyramid LEDs. (a) Sampling position indicated by the dotted line in top view SEM image of the GaN micropyramid LED structures with diameters of 1.5 and 2.5 µm. Cross-sectional BF TEM images of the GaN micropyramids with diameter of (b) 2.5 and (c) 1.5 µm, respectively. (d) EDX line profiles of the indium L characteristic along the dotted lines indicated in figures (b) and (c).

To find the origin of the multiple color emission from different sizes of micropyramid LEDs, we investigated the chemical composition and thickness of $In_xGa_{1-x}N$ quantum well layers coated on their nano- and micro-facets in Figure 5.11. For scanning transmission electron microscopy (STEM) characterization, cross-section of two different sizes of micropyramid LEDs was prepared from the position marked with dotted line in Figure 5.11(a). Figures 5.11(b) and (c) shows the cross-sectional STEM images of micropyramid LEDs having diameters of 1.5 and 2.5 μm, respectively. Bright layers observed in both the images correspond to $In_xGa_{1-x}N$ single quantum well (SQW). For larger size micropyramid LED, two types of $In_xGa_{1-x}N$ layer was observed; $In_xGa_{1-x}N$ layer on slanted sidewall and topmost saw-like layers (see Figure 5.11(b)). On the other hand, for smaller size micropyramid LED, only one type of $In_xGa_{1-x}N$ layer was observed; $In_xGa_{1-x}N$ layer on slanted sidewall (see Figure 5.11(c)). Further compositional analysis was performed by energy-dispersive X-ray spectroscopy (EDX) to determine the indium content of the $In_xGa_{1-x}N$ layers formed on the topmost saw-like layer and slanted sidewall of two different sizes of micropyramid LEDs. This EDX analysis estimated that the In composition of the $In_xGa_{1-x}N$ layer on the slanted sidewall for two different sizes of pyramids was similar. However, much lower In composition with larger variation was observed from the $In_xGa_{1-x}N$ formed on the topmost saw-like layer. The large variation in In composition is the result coming from the difference in In and Ga adatom diffusion length and the geometrical effect of the randomly formed nanopyramids on the topmost layer. These In composition measured on the slanted sidewall and the topmost saw-like $In_xGa_{1-x}N$ layer can be related with the EL characteristics of the device. For all sizes of micropyramid LEDs, 550 nm EL peak was observed and we believe that this came from the $In_xGa_{1-x}N$ layer coated on the slanted sidewall. However, as the size of the micropyramid LEDs increased, additional 490 nm EL peak with broader spectra was observed, which might be related with the $In_xGa_{1-x}N$ layer formed on the saw-like topmost surface that had large variation in In composition.

In summary, we fabricated multicolor semipolar microstructure LEDs on a single substrate using different sizes of micropyramid LED arrays. We observed two dominant EL peaks at 490 and 550 nm, and, by controlling the size of the micropyramid LEDs, we were able to tune the emission color by controlling the relative intensity of these two EL peaks. Additionally, semipolar micropyramid LEDs did not showed any EL peak shift with increasing power, so the emission color were unique for each cell. We believe that the EL color did not changed with increasing power because the $In_xGa_{1-x}N$ layers were only coated on the semipolar facets, which are known to have reduced QCSE. These features, each size of LEDs having a unique color with tunable brightness, strongly suggest that these devices can be used as a pixel for fullcolor display applications. Finally, one important thing to note here is that these nanostructure LEDs showed even smaller reverse bias leakage current than a conventional $In_xGa_{1-x}N$/GaN thin film LED.

5.2.2. Variable color GaN microdonut LED array

In the previous section, size-controlled micropyramid LED arrays were investigated for monolithic, multicolor LED applications. In this section, the fabrication and characteristics of GaN microdonut LEDs with multiple facets and a variable-color LED application will be described. As shown in Figure 5.12, microdonut LEDs have additional inner sidewall facets which did not exist for other typical three-dimensional structures including nanopyramids[2] and nanorods[1], and that $In_xGa_{1-x}N$ SQW formed on the inner sidewall facets had unique thickness and chemical composition, which generated additional EL color. Moreover, all microdonut LEDs in an array showed reliable and reproducible operation, strongly suggesting that the microdonut LEDs can be used as individual light emitters for display applications. The origin of the multicolor emissions of microdonut LEDs was also investigated using electroluminescence (EL) spectroscopy and scanning transmission electron microscopy (STEM).

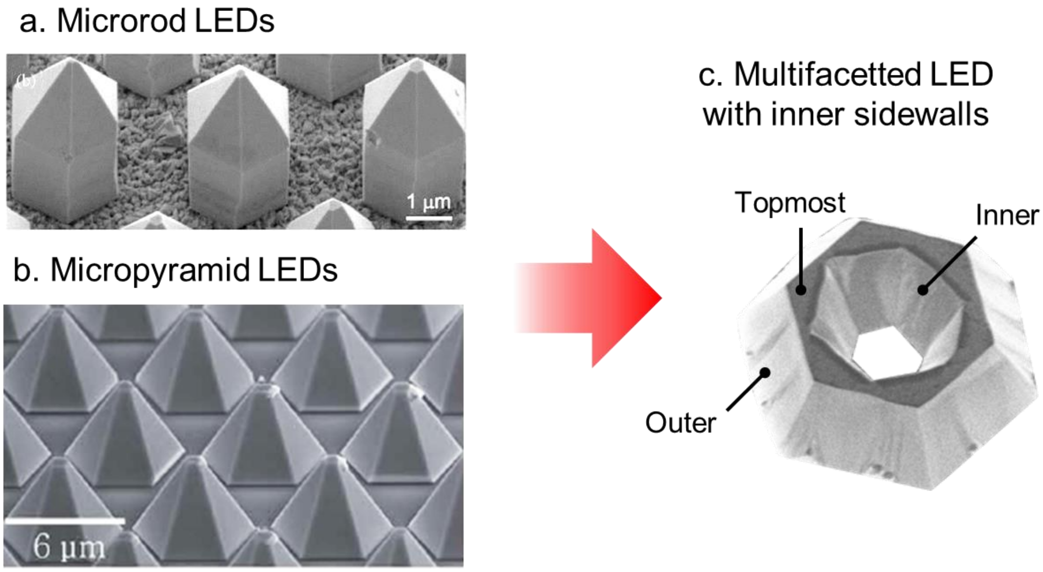

Figure 5.12. Multifacetted LED structures. Tilted SEM images of (a) microrods[1], (b) micropyramids[2], and (c) microdonut LED structures[3].

The general surface morphology of microdonut LED structures having inner and outer multiple facets is evident in the SEM image of Figure 5.13(b). The diameter, width, and period of the microdonuts having inner and outer hexagonal facets were 4, 2, and 8 μm, respectively. The top-view image in Figure 5.13(c) also shows that the crystal planes of the inner and outer sidewalls of the microdonuts were twisted by 30°, similar to the previous reports.[80] Although the widths of the microdonuts were larger than those of the original hexagonal ring patterns because of lateral overgrowth, the width could be controlled by the growth time of the nitride thin film layers. Additionally, the diameter and period of the microdonut LEDs could be determined by designed hexagonal ring patterns.

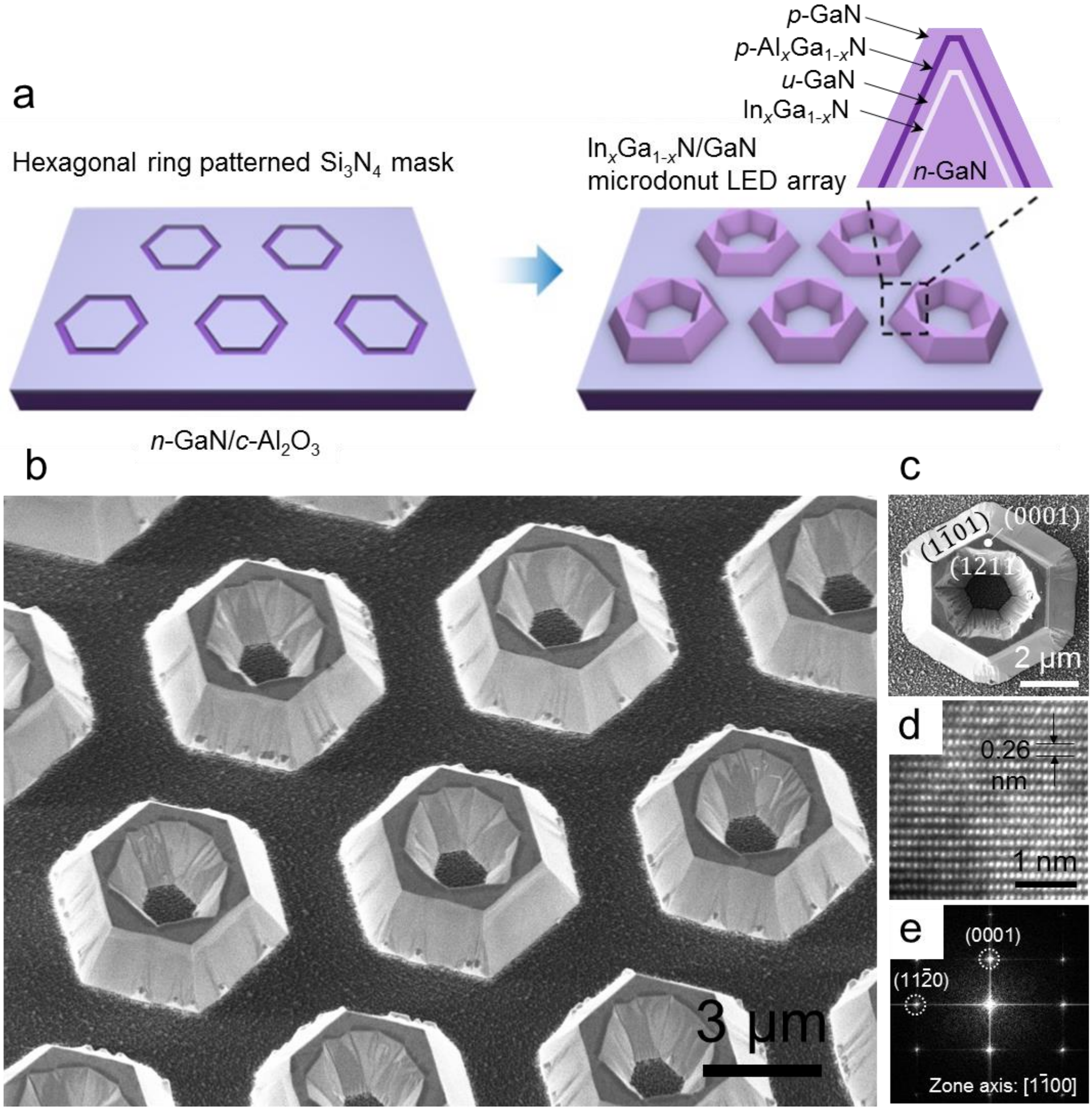

Figure 5.13. Fabrication of microdonut LEDs and electron microscope images. (a) Schematic of SA-MOVPE growth of *n*-GaN microdonut arrays with *p*-GaN/*p*-$Al_xGa_{1-x}N$/*u*-GaN/*u*-$In_xGa_{1-x}N$ layers on *n*-GaN/Al_2O_3 substrates. (b) Bird's-eye view SEM image of the microdonut LED array. (c) Top-view SEM image of a single microdonut LED. (d) HR-TEM image of the single-crystalline GaN microdonut. (e) Diffraction patterns of the HR-TEM image obtained via FFT.

The structural characteristics of the laterally overgrown *n*-GaN microdonuts were investigated using high-resolution transmission electron microscopy (HR-TEM). The HR-TEM image in Figure 5.13(d) clearly shows that the GaN microdonuts are single-crystalline. The lattice spacing between adjacent planes is 0.26 nm, corresponding to the *d*-spacing of GaN(0002) planes. The diffraction pattern in Figure 5.13(e) was obtained through fast Fourier transform (FFT) of the HR-TEM image in Figure 5.13(d), which also indicates that the single-crystalline GaN microdonuts grew along the *c*-axis of wurtzite.

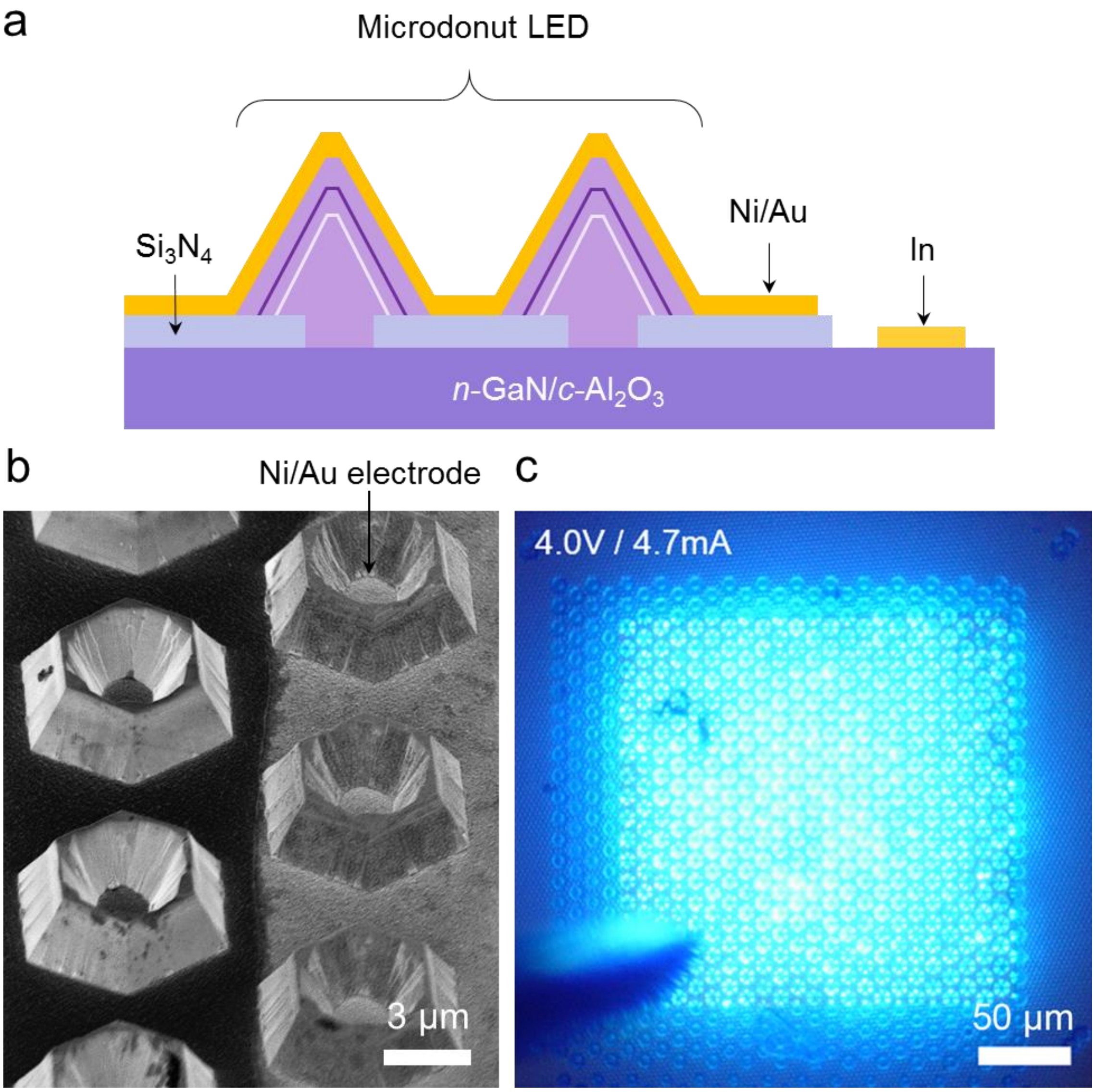

Figure 5.14. Device structure and light emission of microdonut LEDs. (a) Microdonut LEDs fabricated by making ohmic contacts on both the outermost *p*-GaN surface and the underlying *n*-GaN layer. (b) SEM image showing a conformally deposited Ni/Au *p*-contact electrode on the microdonut LEDs. (c) EL image of the microdonut LED array. There is bright and uniform blue light emission from all of the microdonut LEDs inside the semi-transparent 200 × 200

μm^2 metal pad.

We fabricated microdonut LEDs by making ohmic metal contacts on the top surface of the *p*-GaN and the underlying *n*-GaN layer of the microdonut arrays. A cross-sectional diagram of the LED structure is shown in Figure 5.14(a). For *p*-contact electrodes, semi-transparent Ni/Au (10/10 nm) layers with a pad size of 200 × 200 μm^2 were deposited on the top surface of the *p*-GaN. The tilted SEM image in Figure 5.14(b) clearly shows that the Ni/Au layers were conformally deposited on the entire surface of the microdonut LEDs. Then, to form *n*-contact electrodes, the underlying *n*-GaN layer was exposed to air by removing the Si_3N_4 masking layer with buffered oxide etch (BOE), and indium contacts were made on the *n*-GaN. Post-annealing of the LEDs at 400℃ for 5 min in air reduced ohmic contact resistances and enhanced the device characteristics.

Figure 5.14(c) shows a magnified photograph of light emission from a microdonut LED array that consisted of 20 × 30 microdonut LEDs. The LED array emitted visible blue light at an applied current of 4.7 mA at 4.0 V. The light emission was bright enough to be seen with the unaided eye under normal room illumination. Furthermore, all the LEDs exhibited donut-shaped light emission clearly and individually. The reliable and reproducible operation of the microdonut LED array strongly suggests that the microdonut LEDs can be used as individual light emitters for display applications.

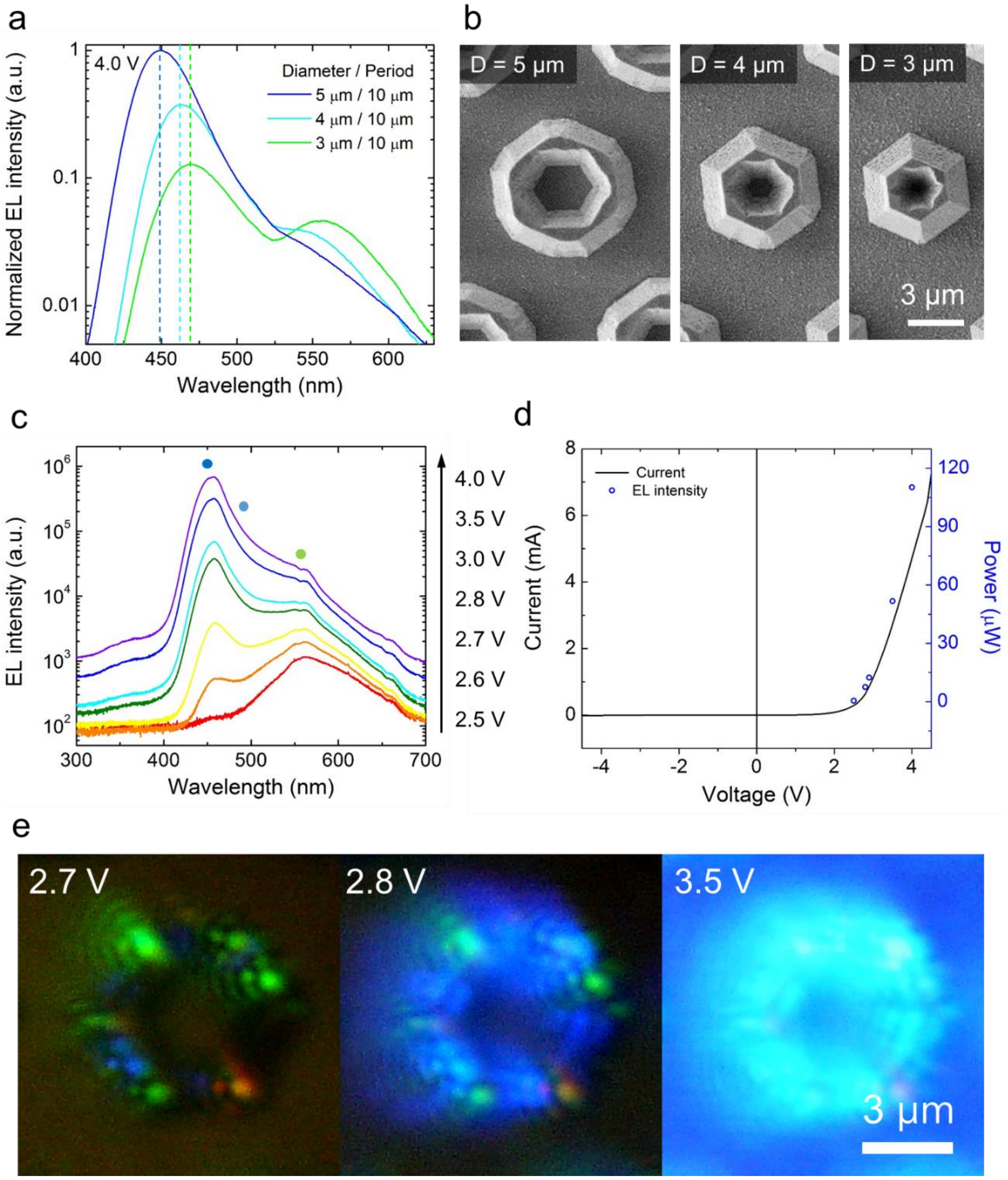

Figure 5.15. Variable-color emission from microdonut LEDs. (a) Normalized EL spectra of microdonut LEDs with diameters of 3, 4, and 5 μm. The dotted lines indicate the respective blue EL peak positions for each size of the microdonut LEDs. (b) SEM images of microdonut LEDs with diameters of 3, 4, and 5 μm. a.u., arbitrary units. (c) EL spectra of microdonut LEDs taken at various voltage levels from 2.5 to 4.0 V. Two dominant peaks centered near 460 nm (blue) and 560 nm (green) are observed. (d) *I*–*V* characteristic curve of the LED (black solid line) and a plot of the output power of light (blue open circles) as a function of

the applied bias voltage. (e) Magnified EL images from a single microdonut LED taken at various levels of applied voltage.

The EL spectra of the microdonut LEDs with different diameters were measured in order to see if their EL colors can be tuned by changing the geometric parameter of microdonut LED arrays. Figures 5.15(a) and (b) show EL spectra and corresponding SEM images of microdonut LEDs with diameters of 3, 4, and 5 μm. The EL spectra given here are displayed by dividing EL intensities measured at an applied voltage of 4.0 V with the electrical input power. Each EL spectra show a dominant emission peak around 460 nm and a relatively weak emission peak around 550 nm, corresponding to blue and green emission, respectively. However, the ratio of green to blue EL peak intensities increased with decreasing diameter of microdonut LEDs. In addition, the dominant blue emission peak was gradually shifted from 450 nm to 470 nm by changing the diameter of the microdonut from 5 to 3um. This result strongly suggests that the relative EL intensities and wavelengths can be tuned by the geometrical factor of microdonut LEDs.

We further investigated the light emission characteristics of the LEDs by measuring their EL spectra at various bias voltages. Figure 5.15(c) shows the voltage dependent EL spectra of a microdonut LED array with a diameter of 5 μm. Under an applied bias voltage of 2.5 V, the dominant EL emission was at 560 nm, corresponding to the color green. Increasing the bias voltage to 2.6 V caused another EL peak to appear, centered at 460 nm, which dominated above 3 V. As confirmed by the EL image (not shown here), EL color from the LEDs also changed from green to blue as the bias voltage increased from 2.5 to 4.0 V, consistent with the EL spectral results.

We also measured the *I*–*V* characteristic curves of the microdonut LEDs with a diameter of 5 μm to investigate the electrical characteristics. Figure 5.15(d) shows that the *I*–*V* characteristic curve had typical rectifying behavior with a turn-on voltage of 2.5 V and a leakage current of 1.2×10^{-5} A at –4.5 V. Above the turn-on voltage, the current began to increase rapidly with the bias voltage, resulting in increased light emission intensity. The forward current level was as high as 7.0 mA at 4.5 V. The low leakage current and high forward current levels for microdonut LEDs are comparable to or even better than those of previously reported nanostructure rod or pyramid LED arrays.[26, 81]

We could estimate the output power of the light emission from the microdonut LEDs by measuring the light intensities at applied electrical powers. The output power, which is displayed at the right axis in Figure 5.15(d), show 110 μW at an applied current of 4.7 mA and a voltage of 4.0 V, corresponding to a wall plug efficiency (W/W) of 0.6%. The efficiency of microdonut LEDs is comparable to or several times higher than those of micropyramid and microrod LEDs.[82, 83] Although the internal quantum efficiency of the GaN microdonut structures is comparable to or even higher than that of the thin film structures,[84] the wall plug efficiency of the microstructure and nanostructure LEDs is much lower than those of commercialized thin film LEDs. We believe that the LED efficiency could be significantly increased by optimizing the materials growth and device fabrication process parameters.

The origin of the green and blue color emissions from the microdonut LEDs was investigated using a spatially resolved, high-magnification EL imaging system. Figure 5.15(e) shows EL images of the single microdonut LED at various bias voltage levels. At 2.7 V, green-colored light can be clearly seen on the hexagonal edges and blue-colored light starts appearing on the outer sidewalls. Upon increasing the applied voltage to 2.8 V, the blue color intensifies and the inner sidewalls also start emitting blue light. Finally, at 3.5 V, almost the entire area of the microdonut LED emits blue light.

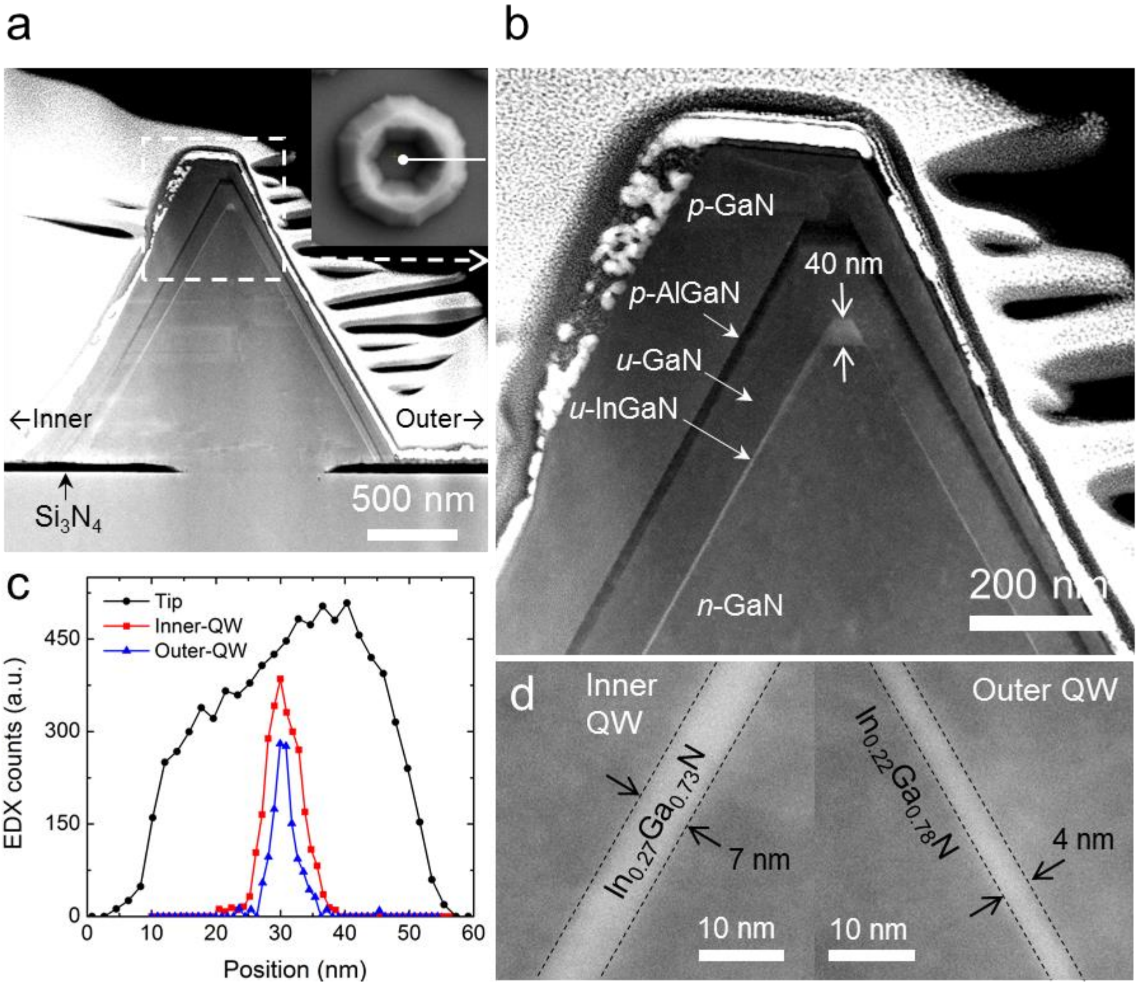

Figure 5.16. Microstructure of a microdonut LED. (a) Low-magnification cross-sectional STEM image of a microdonut LED. The inset SEM image shows the sampled region. (b) Magnified STEM image showing the microstructure of the microdonut LED. The bright and dark layers correspond to $In_xGa_{1-x}N$ and $Al_xGa_{1-x}N$ layers, respectively. (c) EDX line profiles of the indium L characteristic along the topmost, inner, and outer sidewalls. (d) High-magnification STEM images showing the $In_xGa_{1-x}N$ SQW coated on the inner (left) and outer (right) sidewalls of the microdonut LED.

We investigated the spatial distribution of the thickness and composition of the $In_xGa_{1-x}N$ layer coated on the GaN microdonut surfaces, which may be related to the inhomogeneous color light emission observed from the microdonut LEDs. Figure 5.16(a) and b show cross-sectional STEM images of the GaN microdonut taken near the $[12\bar{1}0]$ zone axis. Bright and dark layers observed in both the images correspond to $In_xGa_{1-x}N$ and $Al_xGa_{1-x}N$, respectively. Figure 5.16(b) and (d) show that the thicknesses of the $In_xGa_{1-x}N$ layer on the topmost, inner, and outer sidewall facets were about 40, 7, and 4 nm, respectively. In particular, the magnified STEM images in Figure 5.16(d) show the abrupt and clean interfaces between the GaN and $In_xGa_{1-x}N$ single quantum well (SQW) layer with no structural defects such as dislocations.

Further compositional analysis was performed by energy-dispersive X-ray spectroscopy (EDX) to determine the indium content of the $In_xGa_{1-x}N$ layers formed on the topmost plane and the inner and outer sidewall. The EDX analysis estimated the x values for $In_xGa_{1-x}N$ SQW on the topmost, inner, and outer sidewall facets to be 0.36 ± 0.03, 0.27 ± 0.01, and 0.22 ± 0.01, respectively. Additionally, Figure 5.16(c) shows that the EDX line profiles of the indium L characteristic had full width at half maximum (FWHM) values of 37, 6, and 3 nm for the topmost, inner, and outer sidewalls of the $In_xGa_{1-x}N$ SQW layers, respectively. These FWHM values are consistent with the thicknesses of the $In_xGa_{1-x}N$ layers measured from STEM images. Based on the x value and the thickness of each $In_xGa_{1-x}N$ SQW, the calculated EL wavelengths were 560 ± 20, 490 ± 10, and 450 ± 10 nm for the topmost, inner, and outer sidewalls, respectively.[85, 86] The calculated EL colors from each facet are marked by dots above the EL curves in Figure 5.15(a). From these results, we suggest that the EL peak at 460 nm is a combination of the inner and outer sidewall colors and the peak at 560 nm comes from the topmost plane.

In conclusion, we demonstrated the fabrication and reliable operation of GaN/$In_xGa_{1-x}N$ SQW microdonut-shaped LED microarrays that emit various colors. Two dominant EL peaks at 460 and 560 nm were observed from different positions on the microdonut LEDs, which also depended on the applied voltage. As shown from spatially resolved EL measurements, different colors of light were emitted from the topmost, inner, and outer sidewalls of a single microdonut LED. In addition, the EL colors could be tuned by changing the diameters of the microdonut LEDs. We further confirmed from STEM-EDX measurements that the thicknesses and compositions of the $In_xGa_{1-x}N$ layers on the topmost, inner, and outer sidewalls were quite different. We believe that the anisotropic formation of $In_xGa_{1-x}N$ SQW layers on the different facets of GaN microdonuts plays a critical role in the variable-color emission of the microdonut LEDs.

5.4. Summary

Semiconductor microstructure arrays grown on graphene substrates were used to show their potential for microdisplay. GaN microdisk LED arrays grown on graphene dots were assembled in ultrathin and individually addressable crossbar array for flexible, high-resolution microdisplay. Furthermore, for full-color microdisplay, morphology-controlled GaN microdonut and micropyramid LEDs were used to demonstrate multicolor light-emitters. It was possible to tune the emission color of the multifacetted microstructured LED arrays by controlling the geometic parameters, which changed the thickness and chemical composition of $In_xGa_{1-x}N$/GaN quantum well layers.

Concluding remarks and outlooks

6

6.1. Summary

The goal of this dissertation was to provide ideal integrated device concept based on semiconductor nanoarchitectures grown on 2D layered nanomaterials for future electronic and optoelectronic devices. Ultrathin, flexible, and high-density nanorod devices was demonstrated using 1D+2D hybrid dimensional nanomaterials. Using this system, we were able to examine the individual electrical characteristics of single nanorod within the arrays. Additionally, based on the optoelectronic and piezoelectronic characteristics of ZnO nanorods, high-spatial-resolution photodetector and pressure sensor arrays were demonstrated. Moreover, GaN/ZnO coaxial nanorod heterostructure arrays were used to demonstrate LED applications. In addition to 1D+2D hybrid dimensional nanomaterials, semiconductor microstructure arrays grown on graphene substrates were used to show their potential for microdisplay. GaN microdisk LED arrays grown on graphene dots were assembled in ultrathin and individually addressable crossbar array for flexible, high-resolution microdisplay. Furthermore, for full-color microdisplay, morphology-controlled GaN microdonut and micropyramid LEDs were used to demonstrate variable-color light-emitters.

6.2. Suggestions for future works

This dissertation experimentally demonstrated device concept of individually addressable 1D nanomaterial device arrays on 2D layered nanomaterials. Using this device concept, it would be possible to fabricate ultrahigh density device with rich functionalities since the diameter of the nanorod can be scaled down as small as a few nanometers and many functionalities can be integrated even in a single nanorod by making elaborate axial and coaxial heterostructures. Furthermore, other than graphene, there are varieties of available 2D nanomaterials such as hexagonal boron nitride, transition metal chalcogenides and many high-Tc materials, which are known to have very interesting unconventional physical properties. Only by making appropriate choices and combinations of 1D nanorod heterostructures and 2D nanomaterials, it would be possible to fabricate any kinds of high-density integrated electronic and optoelectronic devices.

Appendix A

Molecular beam epitaxy of semiconductor nanorods on graphene

A.1. Introduction

The use of inorganic semiconductors as an active material is desirable for flexible electronic and optoelectronic device applications,[5, 53, 55] due to the many potential advantages over organic semiconductors in terms of lifetime and efficiency.[71] However, continuous, rigid inorganic semiconductor thin films have no tolerance for mechanical deformation. To address this issue, direct growth of semiconductor nanorods on graphene which has high mechanical strength and flexibility was demonstrated recently mainly using metal-organic chemical vapor deposition (MOCVD);[15, 35, 55] *e.g.*, flexible light-emitting diodes and solar cells using MOCVD-grown GaN and $In_xGa_{1-x}As$ nanorods on graphene.[11, 46, 87, 88] Nevertheless, molecular beam epitaxy (MBE) can provide accurate control over the growth parameters for high-quality nanorod heterostructures with very clean and sharp interfaces using various *in situ* monitoring techniques, such as reflection high electron energy diffraction (RHEED).[89, 90] Realizing the advantage of MBE growth method, Zhuang *et al.* demonstrated In droplet-assisted growth of InAs nanorods on mechanically exfoliated graphite flakes using MBE.[42] However, it is important to develop catalyst-free MBE growth method of nanorods on graphene since this growth method is known to be the best method to produce ultrapure nanorods with homogeneous composition, which are essential building block for future nanorod based devices.[91] Here, we demonstrate the growth of high-quality $InAs/In_xGa_{1-x}As$ coaxial nanorod heterostructures on graphene layers using MBE, with a clean interface. Both transmission electron microscopy (TEM) and *in situ* RHEED were used to investigate the structural properties and growth mechanism of the nanorod heterostructures

A.2. Catalyst-free molecular beam epitaxy (MBE) of III-As coaxial semiconductor nanorod heterostructures on graphene

A.2.1. Growth method and general morphology of InAs/In$_x$Ga$_{1-x}$As nanorods on graphene

In this study, we used a two-step MBE process: (i) high-temperature synthesis of ultrafine-core InAs nanorods, and (ii) subsequent low-temperature coating of In$_x$Ga$_{1-x}$As shell layers on the InAs core nanorods for fabrication of InAs/In$_x$Ga$_{1-x}$As coaxial nanorod heterostructures on graphene layers. This two-step MBE growth method was employed to produce In$_x$Ga$_{1-x}$As shell layers with precisely controlled chemical composition and thickness, which resulted in highly controlled nanorod heterostructures with clean interface compared to spontaneous phase separated MOCVD grown InAs core and In$_x$Ga$_{1-x}$As shell nanowires.[41] Inside of a cryogenically cooled UHV growth chamber (RIBER 32P), InAs nanorods were grown at 530℃ for 1 h, by supplying high-purity indium (In) and uncracked arsenic (As$_4$) molecular beams from Knudsen cells. The beam-equivalent pressures (BEPs) of In and As$_4$ were 6×10^{-8} and 7×10^{-5} Torr, respectively. For catalyst-free growth of InAs nanorods, we supplied As$_4$ to the substrates for 10 min before supplying In to prevent In droplet formation on the graphene layers, which resulted in quite different nucleation and crystal growth behavior from vapor–liquid–solid (VLS) growth.[36, 42]

After the preparation of InAs nanorods, InAs/$In_xGa_{1-x}As$ coaxial nanorod heterostructures were subsequently synthesized by heteroepitaxial growth of an $In_xGa_{1-x}As$ thin layer on InAs core nanorods. Deposition of $In_xGa_{1-x}As$ coaxial shell layers was performed at 380℃ for 1 h by the addition of a Ga molecular beam, resulting in an $In_xGa_{1-x}As$ layer coating over the entire InAs nanorod surface. For the growth of $In_xGa_{1-x}As$ coaxial shell layers, In, Ga, and As_4 BEPs that we used were 6×10^{-8}, 1×10^{-8}, and 2×10^{-6} Torr, respectively. Because the molecular beam fluxes were strongly one-directional, the vertically well-aligned nanorods were placed on rotating substrates to allow uniform exposure to all sides of the nanorods by the molecular beam fluxes; this resulted in homogeneous, uniform film formation, in terms of thickness and composition of the coaxial shell layers.

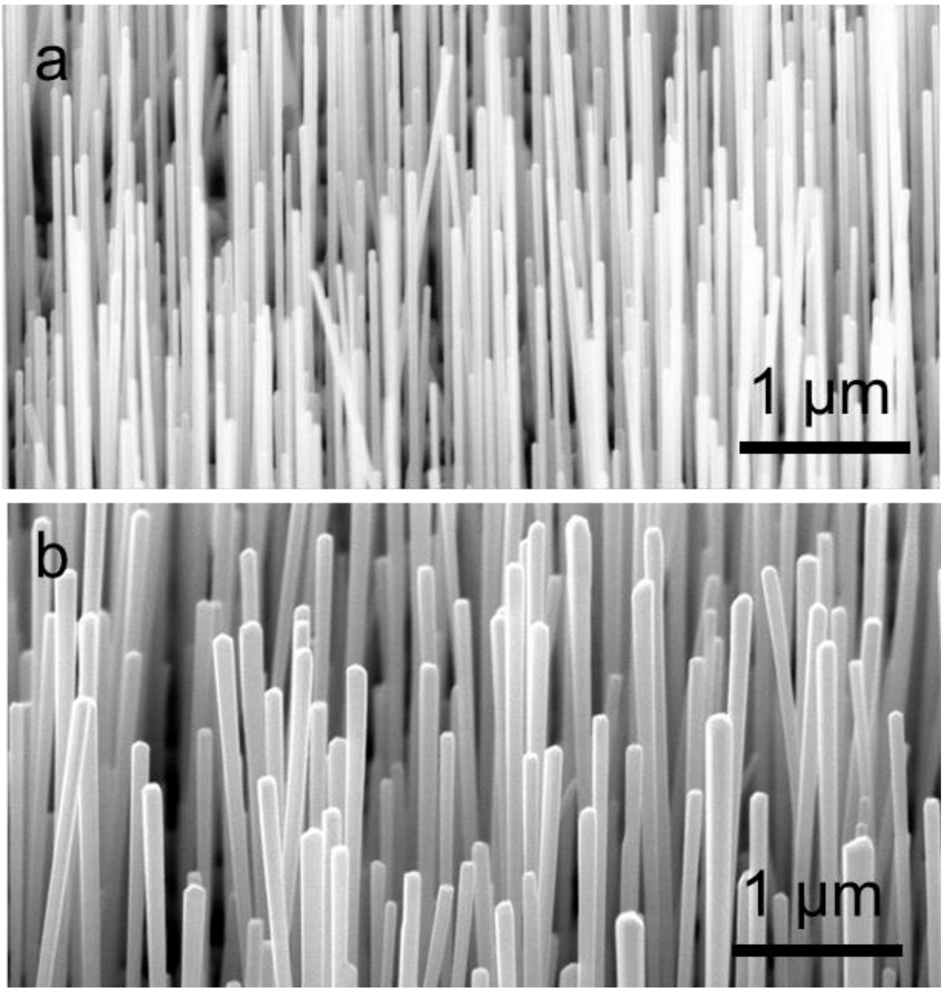

Figure A.1. SEM tilted images of (a) InAs nanorods grown on CVD graphene layers and (b) InAs/In$_x$Ga$_{1-x}$As coaxial nanorod heterostructures grown on CVD graphene layers.

The surface morphologies of InAs nanorods and InAs/In$_x$Ga$_{1-x}$As coaxial nanorod heterostructures grown on CVD graphene layers were investigated using scanning electron microscopy (SEM). The tilted SEM image in Figure A.1(a) shows that the high-density InAs nanorods were vertically well-aligned on the graphene layers. The mean diameter, height, and density of the InAs nanorods were 70 nm, 10 μm, and 5×10^{8} cm^{-2}, respectively. Meanwhile, Figure A.1(b) shows a tilted SEM image of InAs/In$_x$Ga$_{1-x}$As coaxial nanorod heterostructures on CVD graphene layers. After coaxial coating of the In$_x$Ga$_{1-x}$As shell layer, the mean diameter of nanorods increased to 110 nm, indicating that the average thickness and growth rate of the $In_xGa_{1-x}As$ shell layer was 20 nm and 0.06 Å s^{-1}, respectively. Non-tapered morphology was also observed, indicating that the thickness of the $In_xGa_{1-x}As$ shell layer was uniform over the entire surface. The surface morphology of the shell layer depended critically on the As_4 BEP; while the uniform coating of the shell layer shown in Figure A.1(b) was achieved for an As_4 BEP of 2×10^{-6} Torr, inverse-tapered shapes were observed for a higher As_4 BEP of 5×10^{-6} Torr or above.

The surface morphology of the $In_xGa_{1-x}As$ shell layer depended critically on the As_4 beam equivalent pressure (BEP). When the $In_xGa_{1-x}As$ shell layer was coated under As_4 BEP of 5×10^{-6} Torr or higher, inverse-tapered tips of the nanorods were observed, as shown in Figure A.2, i.e., the diameter near the upper part of $InAs/In_xGa_{1-x}As$ coaxial nanorod heterostructures was larger compared to other parts of the nanorods.

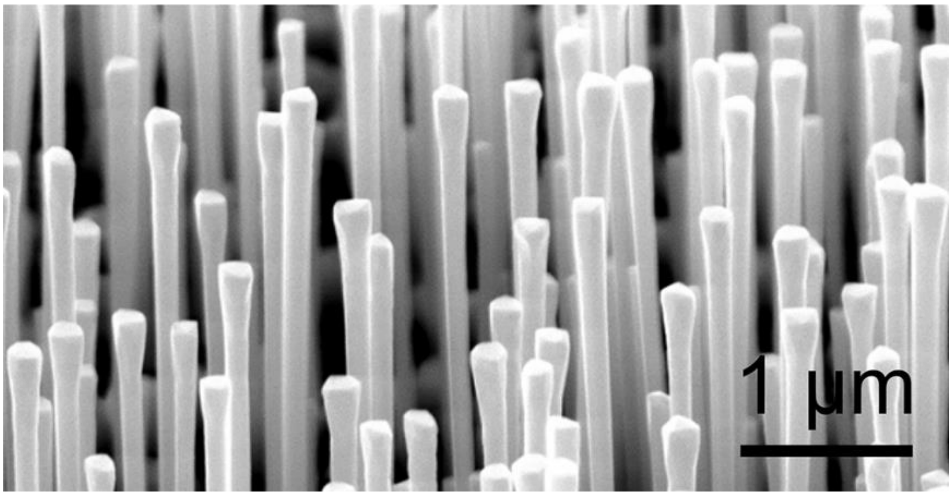

Figure A.2. Surface morphology of $InAs/In_xGa_{1-x}As$ coaxial nanorod heterostructures with an $In_xGa_{1-x}As$ coaxial shell-layer coated under a high As_4 BEPs of 5×10^{-6} Torr.

We also investigated the critical growth parameters that affected the dimension and density of InAs nanorods. The diameter of the nanorods generally increased with

In BEP and the height of the nanorods depended on both As_4 BEP and growth temperatures. S. Hertenberger *et al.* explained that, either at high As/In ratio near the InAs nanorod tip or at high growth temperature, diffusion length of In adatom increases and the probability for incorporation at the InAs nanorod growth front is enhanced compared to that at the lateral sidewalls.[92] Meanwhile, the density of the InAs nanorods depended on both molecular fluxes and growth temperature, since these factors strongly affect the surface migration lengths of adatoms.[92, 93]

A.2.2. Effect of growth temperature

The growth temperature also strongly affected the dimension and density of InAs nanorods grown on CVD graphene layers, as shown in Figure A.3. We varied the growth temperature from 330 to 580℃ with 50℃ intervals while fixing other growth parameters, including growth time, In BEP, and As_4 BEP to 30 min, 6×10^{-8}, and 3×10^{-5} torr, respectively. From the tilted SEM images in Figure A.3(a), we can see longer InAs nanorods at higher temperature, while high density of shorter InAs nanorods can be observed at lower temperature. To compare the differences in detail, the dimension and density of InAs nanorods were plotted as a function of growth temperature in Figures A.3(b) and (c). We can see that the height of nanorods increased as the growth temperature increased from 380 to 530℃, but decreased at higher temperature of 580℃. Additionally, we observed that the density of InAs nanorods monotonically decreased with growth temperature and the density of nanoislands was minimum at 480℃.

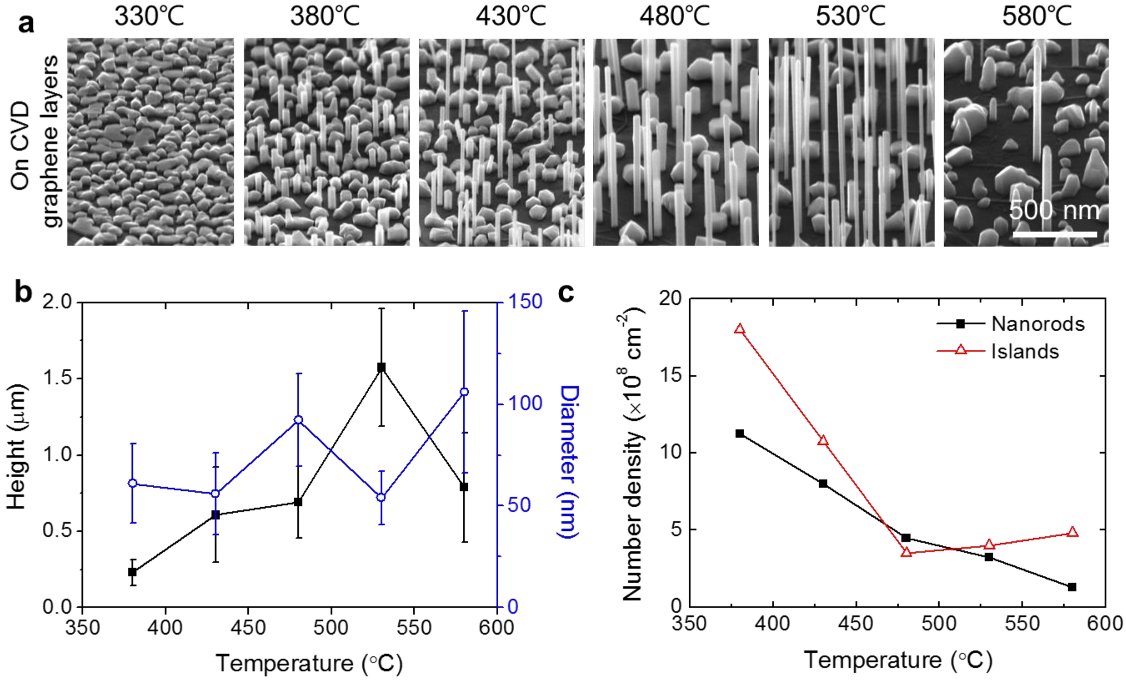

Figure A.3. Effect of growth-temperature-dependent surface morphology of MBE-grown InAs nanorods on CVD graphene layers. Series of tilted SEM images of MBE-grown InAs nanorods grown at 330, 380, 430, 480, 530, and 580°C on CVD graphene layers. The growth temperatures of each sample are indicated above each SEM image. The corresponding plot of (c) dimension of nanorods and (d) number density of nanorods and nanoislands on CVD graphene layers as a function of the growth temperature.

A.2.3. Effect of beam equivalent fluxes

The effect of In and As_4 BEPs on the surface morphology of InAs nanorods grown on chemical vapor deposited (CVD) graphene layers is investigated in Figure A.4. To investigate the effect of In BEP only, In BEP was varied while other growth parameters were fixed; the growth temperature, time, and As_4 BEP were set to 530°C, 30 min, and 3×10^{-5} Torr, respectively. Series of tilted scanning electron microscopy (SEM) images in Figure A.4(a) show InAs nanorods grown on CVD graphene layers using In BEP of 1.2, 2.4, 12, and 24×10^{-8} Torr, and the corresponding plots of dimension and density of InAs nanorods are shown in Figures A.4(b) and (c), respectively. We can see that the diameter of nanorods increased with In BEP but the height of nanorods was not considerably affected by In BEP. The number density of InAs nanorods significantly increased with In BEP until 1.2×10^{-7} Torr. However, for even higher In BEP of 2.4×10^{-7} Torr, InAs nanorods and nanoislands merged with each other and the number density rather decreased.

Next, the effect of As_4 BEP was investigated by varying As_4 BEP and fixing other growth parameters; the growth temperature, time, and In BEP were set to 530℃, 30 min, and 6×10^{-8} Torr, respectively. Series of tilted SEM images in Figure a.4(d) show InAs nanorods grown on CVD graphene layers using As_4 BEP of 1.5, 2.2, 3.7, and 4.5×10^{-5} Torr, and the corresponding plots of dimension and density of InAs nanorods are shown in Figures A.4(e) and (f), respectively. Above As_4 BEP of 2.2×10^{-5} Torr, the height of nanorods increased proportionally with As_4 BEP. However, below this value, for As_4 BEP between 1×10^{-5} and 2.2×10^{-5} Torr, the height of InAs nanorods was similar. The diameter of nanorods generally decreased with increasing As_4 BEP, suggesting that InAs nanorods with higher aspect ratio can be grown under higher As_4 BEP. Meanwhile, the density of nanorods showed a maximum at As_4 BEP of 2.2×10^{-5} Torr.

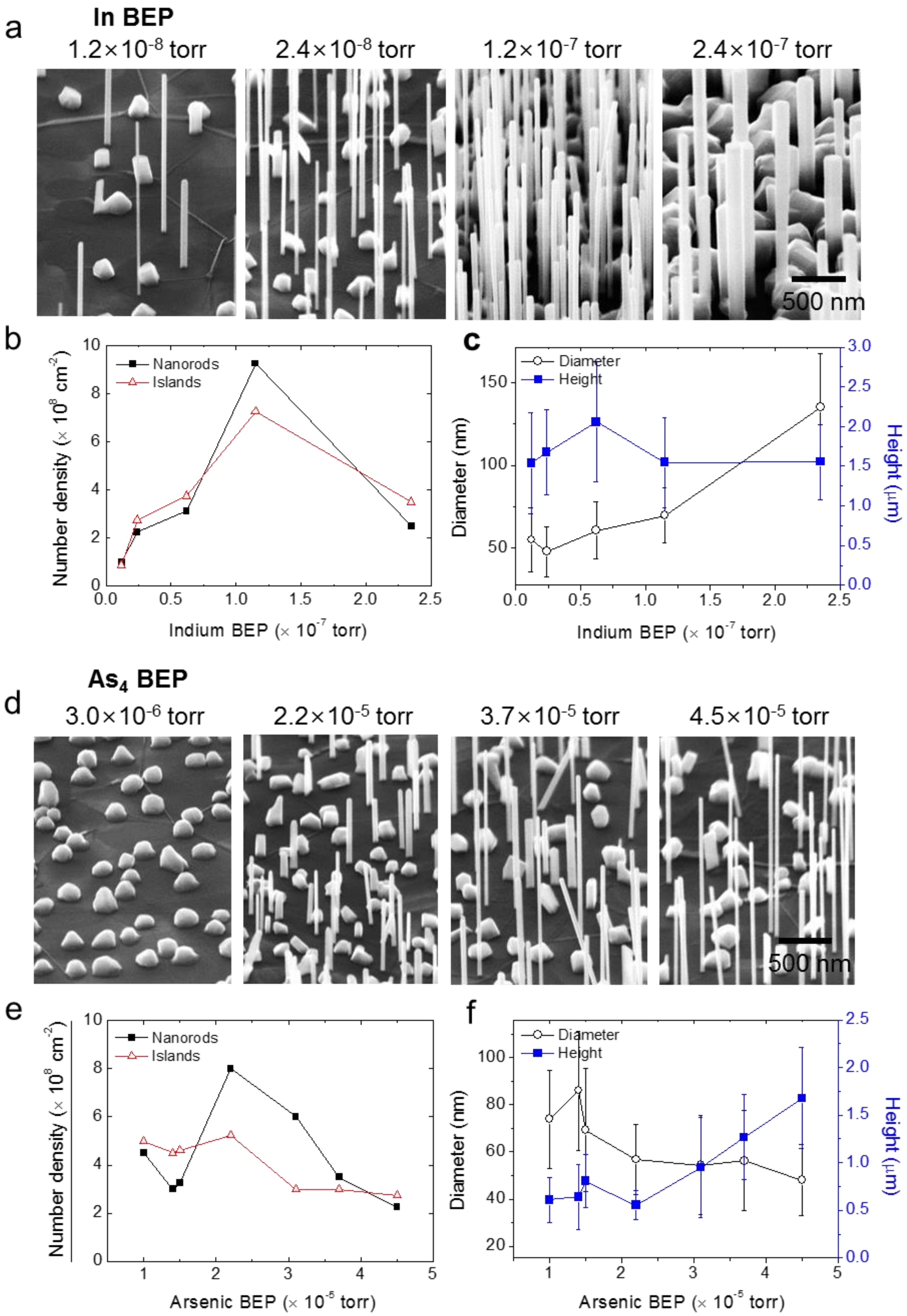

Figure A.4. Effect of In and As_4 BEPs on the surface morphology of InAs nanorods grown on CVD graphene layers. (a) Series of tilted SEM images of InAs nanorods grown on CVD graphene layers using an In BEP of 1.2, 2.4, 12, and

24×10^{-8} Torr, and the corresponding plots of (b) dimension of nanorods and (c) number density of the nanorods and nanoislands. (d) Series of tilted SEM images of InAs nanorods grown on CVD graphene layers at As_4 BEP of 1.5, 2.2, 3.7, and 4.5×10^{-5} Torr, and the corresponding plots of (e) dimension of nanorods and (f) number density of nanorods and nanoislands. The numbers above each SEM image indicate the In or As_4 BEPs used to grow each sample.

A.3. In-situ characterization using reflection high energy electron diffraction (RHEED)

The entire growth procedure was monitored *in situ* via RHEED (electron beam energy: 22.2 keV; spot size: 0.2 mm). The length of the electron-beam irradiated area along the beam trajectory was 15 mm, indicating a 1° incident angle of the electron beam with respect to the substrate surface. Real-time video of the RHEED patterns was acquired using a commercial digital single-lens reflex camera; the time resolution of the video was 0.04 s. The lattice parameters of the InAs nanorods and CVD graphene layers were estimated by comparing the spacing between RHEED patterns with that of Si(111) substrates as a reference. RHEED images during the coaxial shell-layer growth were acquired by temporarily stopping the growth by closing In and Ga shutters and rotation of the substrates.

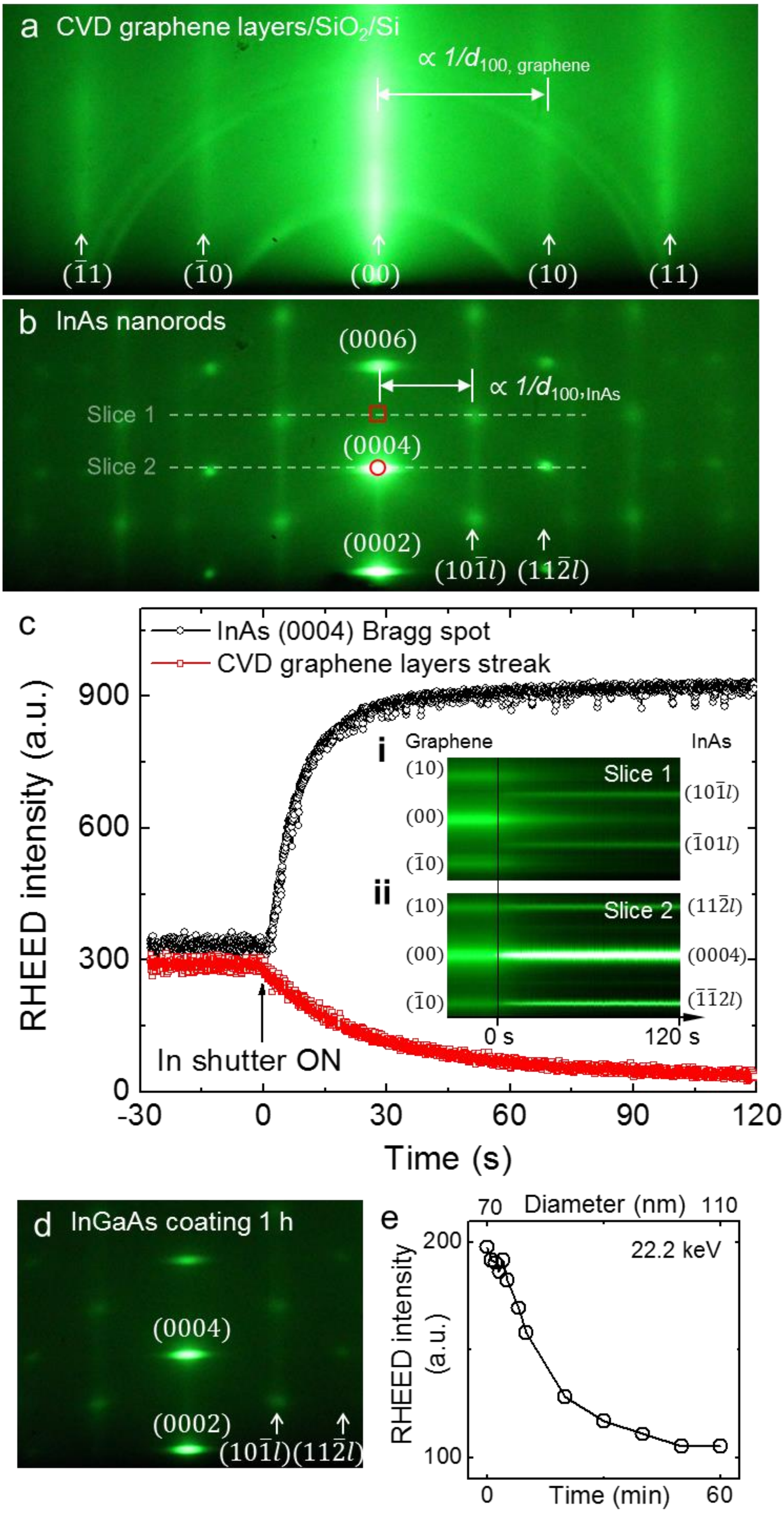
a CVD graphene layers/SiO2/Si
∝ 1/d100, graphene
(1̄1)
(1̄0)
(00)
(10)
(11)
b InAs nanorods
(0006)
∝ 1/d100,InAs
Slice 1
(0004)
Slice 2
(0002)
(101̄l)
(112̄l)
c
InAs (0004) Bragg spot
CVD graphene layers streak
RHEED intensity (a.u.)
900
600
300
0
In shutter ON
-30
0
30
60
90
120
Time (s)
i
Graphene
InAs
(10)
(00)
(1̄0)
Slice 1
(101̄l)
(1̄01l)
ii
(10)
(00)
(1̄0)
Slice 2
(112̄l)
(0004)
(1̄1̄2l)
0 s
120 s
d InGaAs coating 1 h
(0004)
(0002)
(101̄l)(112̄l)
e
70
Diameter (nm)
110
22.2 keV
200
100
RHEED intensity (a.u.)
0
Time (min)
60

Figure A.5. RHEED patterns during InAs/In$_x$Ga$_{1-x}$As coaxial nanorod heterostructure growth on CVD graphene layers. RHEED patterns of (a) CVD graphene layers transferred onto SiO$_2$/Si substrates and (b) InAs nanorods grown on CVD graphene layers/SiO$_2$/Si. (c) Integrated RHEED intensities of (0004) InAs Bragg spots (red circle in figure (b)) and (00) streak from CVD graphene layers (red box in figure (b)) as a function of time. The inset shows the evolution of RHEED intensities along the dotted lines (i) slice 1 and (ii) slice 2 in figure (b), plotted as a function of time. (d) RHEED patterns of InAs/In$_x$Ga$_{1-x}$As coaxial nanorod heterostructures on CVD graphene layers, after growing 20-nm-thick In$_x$Ga$_{1-x}$As coaxial shell layers. (e) Integrated RHEED intensity of (0004) InAs Bragg spot during the coaxial coating of In$_x$Ga$_{1-x}$As shell layers.

In this study, MBE-grown InAs nanorods on CVD graphene layers was monitored *in situ* in the initial growth stage using RHEED. Before the nanorod growth, as shown in Figure A.5(a), a streaky RHEED pattern was observed from CVD graphene layers transferred onto a SiO$_2$/Si substrate. The streaky RHEED patterns of CVD graphene layers remained unchanged, regardless of the azimuthal rotation angles, strongly suggests that the hexagonal graphitic layers were aligned in the (001) direction and the in-plane orientations of each grain were random. When the nanorod growth was initiated (t = 0), the streaky RHEED pattern of CVD graphene layers (Figure A.5(a)) was changed to bright Bragg spots corresponding to InAs nanorods (Figure A.5(b)) within a few seconds of In shutter opening. The appearance of these spots indicated an abrupt change from 2D RHEED patterns to 3D Bragg diffraction patterns.[92]

To further examine the abrupt change in RHEED patterns, the integrated RHEED intensities of the InAs Bragg spot (circle in Figure A.5(b)) and the streak from CVD graphene layers (rectangular box in Figure A.5(b)) were plotted as a function of time in Figure A.5(c). An abrupt rise in the integrated RHEED intensity of the InAs (0004) Bragg spot was observed without delay (within 1 s), as shown in Figure A.5(c). The instantaneous, monotonic increase in the Bragg spot intensity, not observed typically for metal-catalyst-assisted VLS growth mode,[90, 92] strongly suggests the direct formation of catalyst-free InAs nanorod crystal growth on CVD graphene layers.

Additionally, the lattice parameters of the CVD graphene layers and InAs nanorods were estimated by comparing the spacing between the RHEED patterns, as indicated in Figures A.5(a) and (b). The d_{100} interplanar spacing of CVD graphene layers and wurtzite InAs nanorods were 2.1 and 3.7 Å, respectively, which agree with previously reported values.[94, 95] To examine the change in the lattice parameters during the initial growth stage, the evolution of RHEED intensities along the dotted lines in Figure A.5(b) was plotted as a function of time in the combined images shown in the inset of Figure A.5(c). Inset (i) of Figure A.5(c) clearly shows the $(10\bar{1}l)$ Bragg spots of InAs that appeared abruptly with the initiation of growth (t = 0); the position of these spots did not change as growth progressed, implying that unstrained InAs nanorod crystals formed directly on CVD graphene layers, without a strain relaxation step. Inset (ii) of Figure A.5(c) shows that the position of the (10) streak from CVD graphene layers was aligned indistinguishably with that of $(11\bar{2}l)$ InAs Bragg spots, implying a possible in-plane, lattice-matching configuration of InAs crystals and graphene layers.[36, 96]

For longer growth times approaching 1 h and InAs nanorod lengths reaching 10 μm, sharp spots were clearly visible in the RHEED patterns (Figure A.5(b)) thanks to the transmission mode of RHEED.[97] For all azimuthal rotation angles, the RHEED patterns from the InAs nanorods were the same, indicating that the nanorods were vertically well-aligned along $[0002]_{WZ}$ and $[111]_{ZB}$, but their in-plane orientations were random; these results were attributed to in-plane misorientations of grains in the CVD graphene layers.[96, 98]

RHEED also enabled us to investigate the growth of $In_xGa_{1-x}As$ coaxial shell layers as well as InAs nanorods. For $In_xGa_{1-x}As$ coaxial-shell layer growth, although the RHEED intensity decreased with growth time as the nanorod thickness increased, no significant change in the RHEED pattern was observed, as shown in Figures A.5(d) and €. From the fact that the RHEED patterns maintained the same shape during coaxial shell-layer growth, we suggest that the $In_xGa_{1-x}As$ coaxial shell layer grew epitaxially on the InAs nanorods; this was later confirmed by cross-sectional TEM analysis.

A.4. Ex-situ characterization using transmission electron microscopy (TEM)

For detailed structural analysis, the cross-section of the InAs/$In_xGa_{1-x}As$ coaxial nanorod heterostructures was prepared by dual-beam focused ion beam milling (FIB) and analyzed using TEM. The chemical composition was analyzed by high-angle annular dark-field scanning TEM (STEM) equipped with energy dispersive X-ray spectroscopy (STEM-EDS) capabilities. Additionally, the InAs/$In_xGa_{1-x}As$ coaxial nanorod heterostructure crystallinity was investigated by bright-field (BF) and high-resolution (HR) TEM.

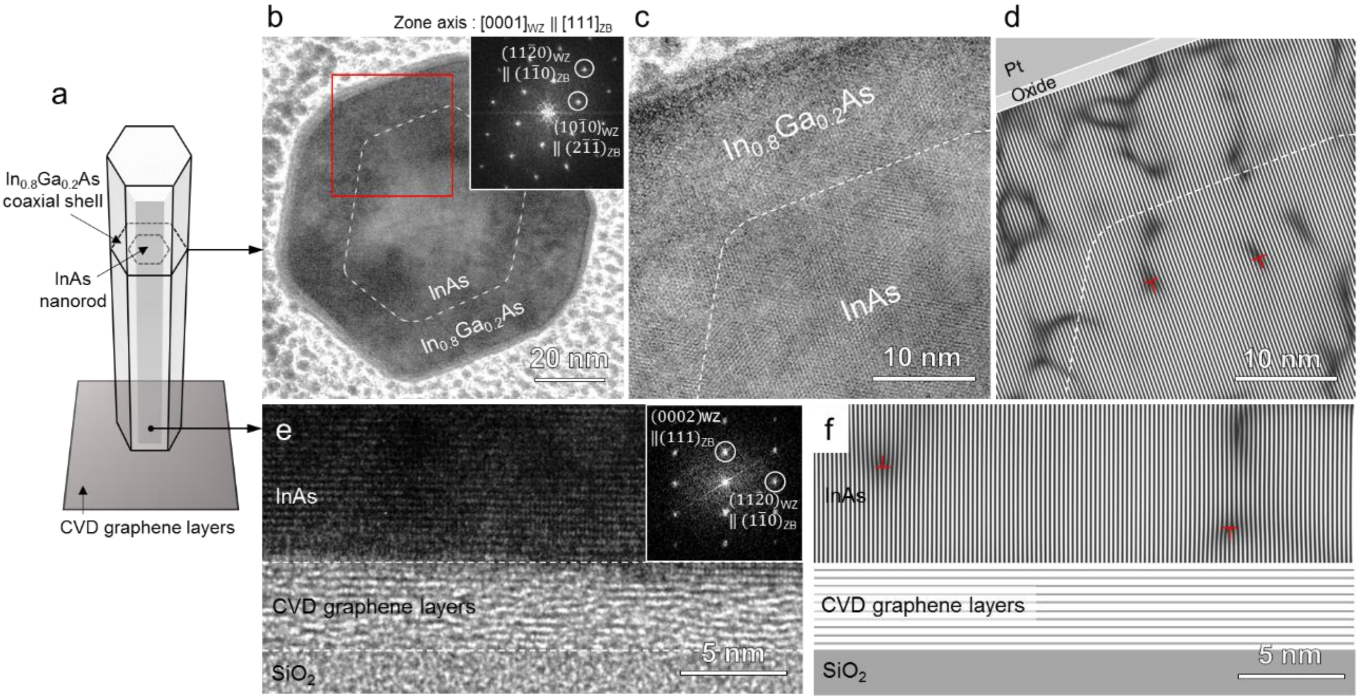

Figure A.6. Microstructure of InAs/In$_x$Ga$_{1-x}$As coaxial nanorod heterostructures on CVD graphene layers. (a) Schematic diagram of the TEM sampling positions and the corresponding plan-view (b) BF-TEM, (c) HR-TEM, and (d) Fourier filtered images of InAs/In$_x$Ga$_{1-x}$As coaxial nanorod heterostructures. The inset diffraction patterns in figure (b) are obtained via FFT of the HR-TEM images in figure (c). The areas of oxide layer formed on the nanorod surface and Pt-protection layer are marked in figure (d). Cross-sectional (e) HR-TEM and (f) Fourier-filtered images of the interface between InAs and CVD graphene layers. The inset diffraction patterns in figure (e) were obtained via FFT of the corresponding HR-TEM image. The locations of misfit dislocations estimated by Fourier filtered images are indicated by T.

The structural characteristics of InAs/In$_x$Ga$_{1-x}$As coaxial nanorod heterostructures were investigated using TEM. As indicated in the schematic diagram, cross-sectional TEM samples were prepared using FIB. Figure A.6(b) shows a cross-sectional BF image of InAs/In$_x$Ga$_{1-x}$As nanorods, exposing the (0001) surface. Since the interface between the In$_x$Ga$_{1-x}$As and InAs layers was indistinguishable in the BF image without performing chemical analysis, the interface between the In$_x$Ga$_{1-x}$As shell layer and InAs nanorod core is indicated by dotted hexagonal lines in the figure by comparing STEM image and STEM-EDS mapping results, which will be later shown in Figure A.7. Both the $In_xGa_{1-x}As$ shell layer and the InAs core exhibited well-developed $\{11\bar{2}0\}$ facets, as opposed to $\{10\bar{1}0\}$ facets, verified exclusively by the fast Fourier transform (FFT) pattern in the inset of Figure A.6(b). This single type of facets were identically observed for ten randomly selected nanorods. Previous TEM studies showed that both $\{10\bar{1}0\}$ and $\{11\bar{2}0\}$ side facets were present in the InAs nanorod system.[99, 100] However, formations of the only $\{11\bar{2}0\}$ facets for $In_xGa_{1-x}As$ shell layer and InAs core may be associated with a smaller surface energy for the $\{11\bar{2}0\}$ side facet than that of the $\{10\bar{1}0\}$ side facet in the InAs nanorod.[91, 101] The epitaxial relationship and atomic structure of InAs/$In_xGa_{1-x}As$ coaxial nanorod heterostructures were investigated using HR-TEM. Figure A.6(c) shows a HR-TEM image of the region marked with a rectangular box in Figure A.6(b). Significant edge dislocations were not observed at the interface between InAs and $In_xGa_{1-x}As$ layers. The interface in the coaxial nanorod heterostructures was further examined in more detail by the Fourier-filtered image shown in Figure A.6(d), obtained by selecting the $(10\bar{1}0)$ FFT spots of both InAs and $In_xGa_{1-x}As$. The areas of oxide layer formed on the nanorod surface and Pt-protection layer are also marked in Figure A.6(d). The Fourier-filtered image in Figure A.6(d) shows fringe patterns were well-aligned at the heterointerfaces with few misfit dislocations. The locations of misfit dislocations estimated by Fourier filtered images are indicated by T. These TEM results strongly suggest that the growth of $In_xGa_{1-x}As$ on InAs is coherently epitaxial, which results presumably from small lattice mismatch (< 1%) between the InAs and $In_xGa_{1-x}As$

layers. Such an epitaxial relationship with a small lattice mismatch produced nearly overlapped FFT patterns in the inset of Figure A.6(b).

We also investigated the atomic arrangement of InAs at the interface between InAs and graphene using cross-sectional HR-TEM images. Figure A.6(e) shows a clean interface between the InAs nanorod and graphene layers without any interfacial layer. HR-TEM images of the InAs nanorod crystal in Figure A.6(e) revealed a well-aligned growth direction, parallel to the *c*-axis of CVD graphene, as indicated by FFT in the inset. Fourier filter analysis was also performed to investigate the microstructural characteristics of the InAs nanorod at the interface. Figure A.6(f) is a Fourier-filtered image of Figure A.6(e), obtained by selecting the $(11\bar{2}0)$ FFT spots of InAs. This image reveals that the dislocations were not concentrated close to the interface; this outcome would be attributed to the heteroepitaxial relationship between the graphene layers and InAs.

The crystal structure of InAs/$In_xGa_{1-x}As$ coaxial nanorod heterostructures was investigated by HR-TEM images near the zone axis of $(10\bar{1}0)_{WZ} \parallel (2\bar{1}\bar{1})_{ZB}$ that is perpendicular to the growth direction. To prepare this sample, InAs/$In_xGa_{1-x}As$ coaxial nanorod heterostructures with 5-nm-thick $In_xGa_{1-x}As$ layers were prepared, ultrasonically dispersed in ethanol anhydrous, and subsequently drop-casted and dried on TEM grids. The HR-TEM images in Figure A.8(a) and (b) clearly confirmed the existence of alternating zinc blende and wurtzite crystal phases both along the InAs nanorods and $In_xGa_{1-x}As$ shell layers.

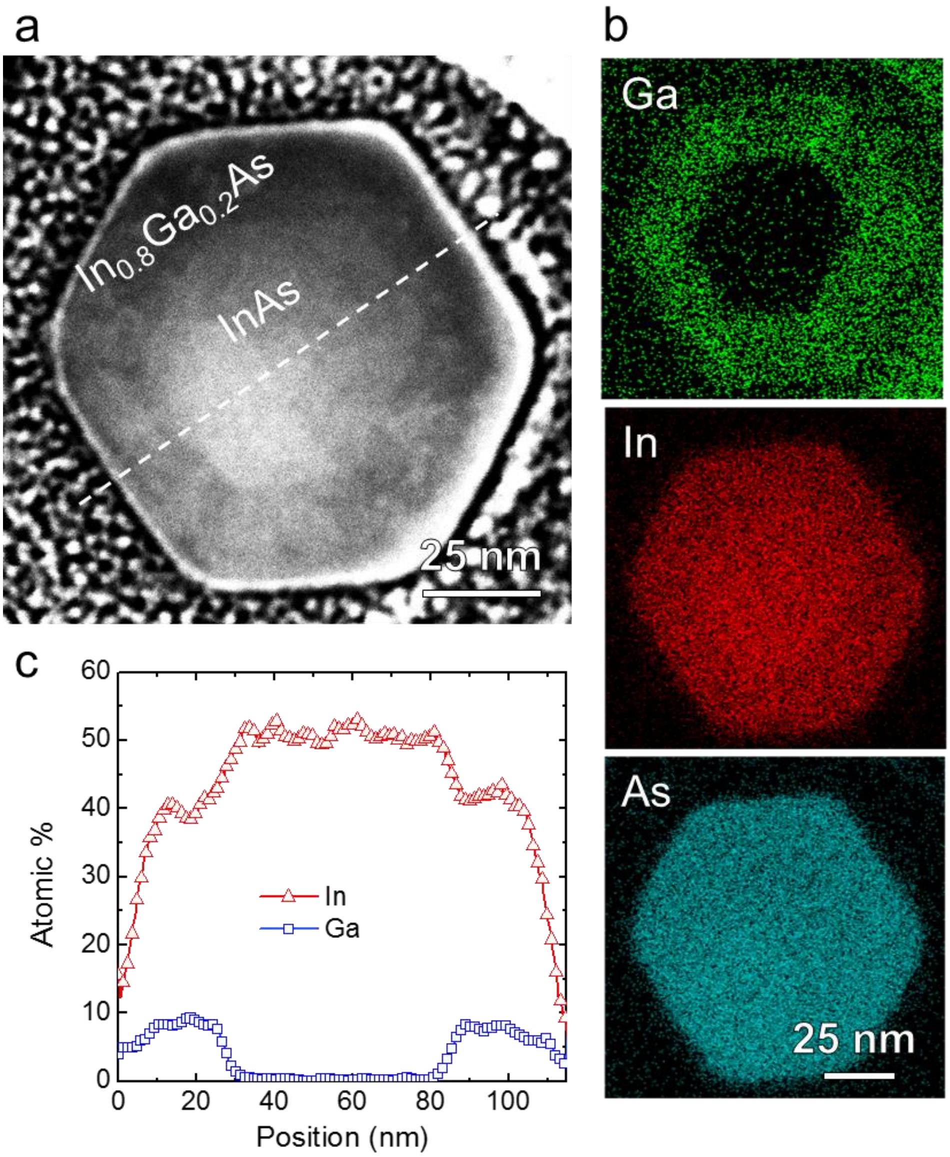

Figure A.7. Chemical composition of InAs/In$_x$Ga$_{1-x}$As coaxial nanorod heterostructures grown on CVD graphene layers. (a) Plan-view STEM image, (b) elemental mapping of Ga, In, and As using STEM-EDS, and (c) EDS line profiles of In and Ga along the dotted line in figure (a).

In addition to the structural analysis, the chemical composition of InAs/In$_x$Ga$_{1-x}$As coaxial nanorod heterostructures was investigated by STEM and EDS. As shown in Figure A.7(a), from the contrast change in cross-sectional STEM image of a (0001) surface of an InAs/In$_x$Ga$_{1-x}$As nanorod, which reflects difference in atomic mass of elements, hexagonal formation of InAs core was evidently observed in bright inner area, as well as the uniformly coated In$_x$Ga$_{1-x}$As shell layer in dark outer area, indicating that heavier Ga atoms were incorporated at the shell layers. The STEM-EDS mapping of each element in Figure A.7(b) clearly shows the spatial distribution of In, Ga, and As. Ga existed only in the hexagonal ring-shaped outer-shell region; In was detected over the entire nanorod while having a higher density in the inner hexagonal core; and As was detected uniformly over the entire nanorod structure.

To quantify the chemical composition of each layer, we measured the STEM-EDS line profile along the dotted line in Figure A.7(a), which is plotted graphically in Figure A.7(c). From this result, we confirmed the formation of the InAs/$In_xGa_{1-x}As$ coaxial nanorod heterostructure and chemical composition of the $In_xGa_{1-x}As$ shell layer. A larger amount of In atoms, four-fold over that of Ga, was detected; thus, the x value of $In_xGa_{1-x}As$ layer was 0.8 as estimated by STEM-EDS.

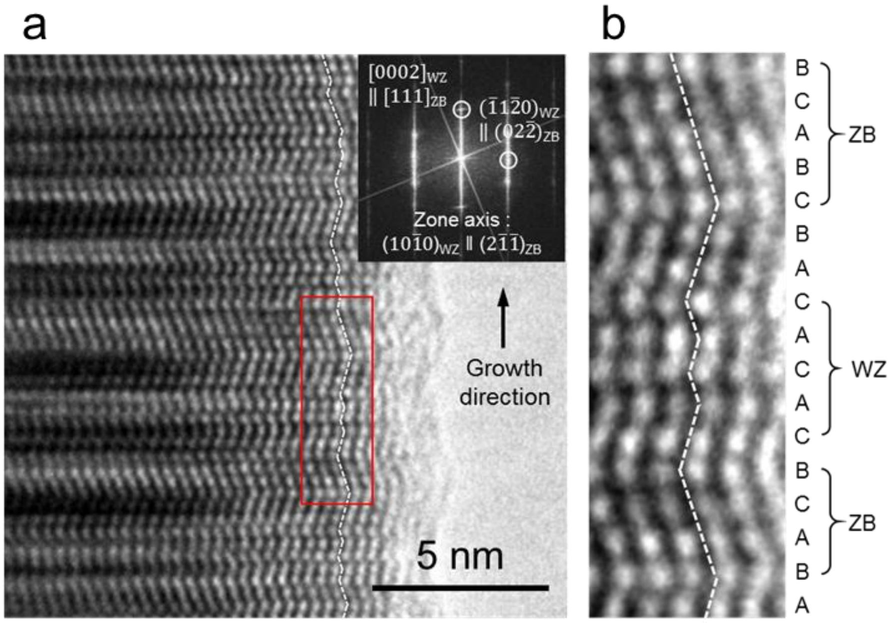

Figure A.8. Vertical TEM images of InAs/$In_xGa_{1-x}As$ coaxial nanorod heterostructures grown on CVD graphene layers taken near the zone axis of $(10\bar{1}0)_{WZ} \| (2\bar{1}\bar{1})_{ZB}$. (a) HR-TEM image and the corresponding streaky diffraction pattern in the inset clearly show mixed zinc blende/wurtzite (ZB/WZ)

crystal phases and stacking faults in the nanorod heterostructures. Alternating WZ and ZB crystal phases are indexed in (b) a magnified HR-TEM image of a region marked with a rectangular box in figure (a).

In conclusion, vertically well-aligned, high-quality InAs/$In_xGa_{1-x}As$ coaxial nanorod heterostructures were grown on CVD graphene layers using MBE. From *in situ* RHEED observation, we confirmed that the InAs nanorods grew on CVD graphene layers in a catalyst-free mode. The formation of InAs/$In_xGa_{1-x}As$ coaxial nanorod heterostructures was confirmed by STEM and EDS analysis, which showed a clearly defined InAs core and $In_xGa_{1-x}As$ shell layer with uniform composition and thickness. In addition, cross-sectional HR-TEM images demonstrated a clean interface between $In_xGa_{1-x}As$ and InAs. Our work would provide a novel and straightforward pathway for a monolithic integration of semiconductor coaxial nanorod heterostructures on two-dimensional layered materials, which is a key factor to exploit it for flexible electronics and optoelectronics.

Appendix B

Monolithic integration of wide and narrow band gap semiconductor nanorods on graphene substrate

B.1. Introduction

Monolithic integration of wide and narrow band gap semiconductors can broaden the spectral absorption range and improve the performance of solar cells.[102, 103] From the hybrid heterostructures, composed of wide and narrow band gap semiconductors, we can expect synergetic combination of the unique properties of each material. For these reasons, many studies have focused on direct growth methods of wide band gap semiconductors on narrow band gap semiconductors, despite of the large lattice mismatch that created defects and strain in crystals.[104, 105] Recently, many reports showed that various kinds of single crystalline 1D nanomaterials including ZnO, GaN, InAs, and GaAs nanostructures can be grown vertically on 2D nanomaterials such as graphene or hexagonal boron nitride.[15, 35, 36, 41] In these hybrid dimensional nanomaterials, the periodic hexagonal atomic arrangement of 2D layered nanomaterials can provide various sizes of supercells, accommodating various materials with different lattice constants to be grown heteroepitaxially and vertically on its surface.[55] Remarkably, Hong *et al.* recently demonstrated that both sides of suspended single layer graphene can act as a van der Waals epitaxial substrate for semiconductor growth, and showed double heterostructures composed of InAs/graphene/InAs.[96] In this work, we report the monolithic integration of InAs and ZnO nanorods by growing them vertically on each surface of the same graphene layers.

Additionally, we investigated the electrical characteristics of the InAs/graphene layers/ZnO nanorods hybrid heterostructures.

B.2. ZnO nanorods/graphene layers/InAs nanorods heterostructures

B.2.1. Growth and structural characteristics

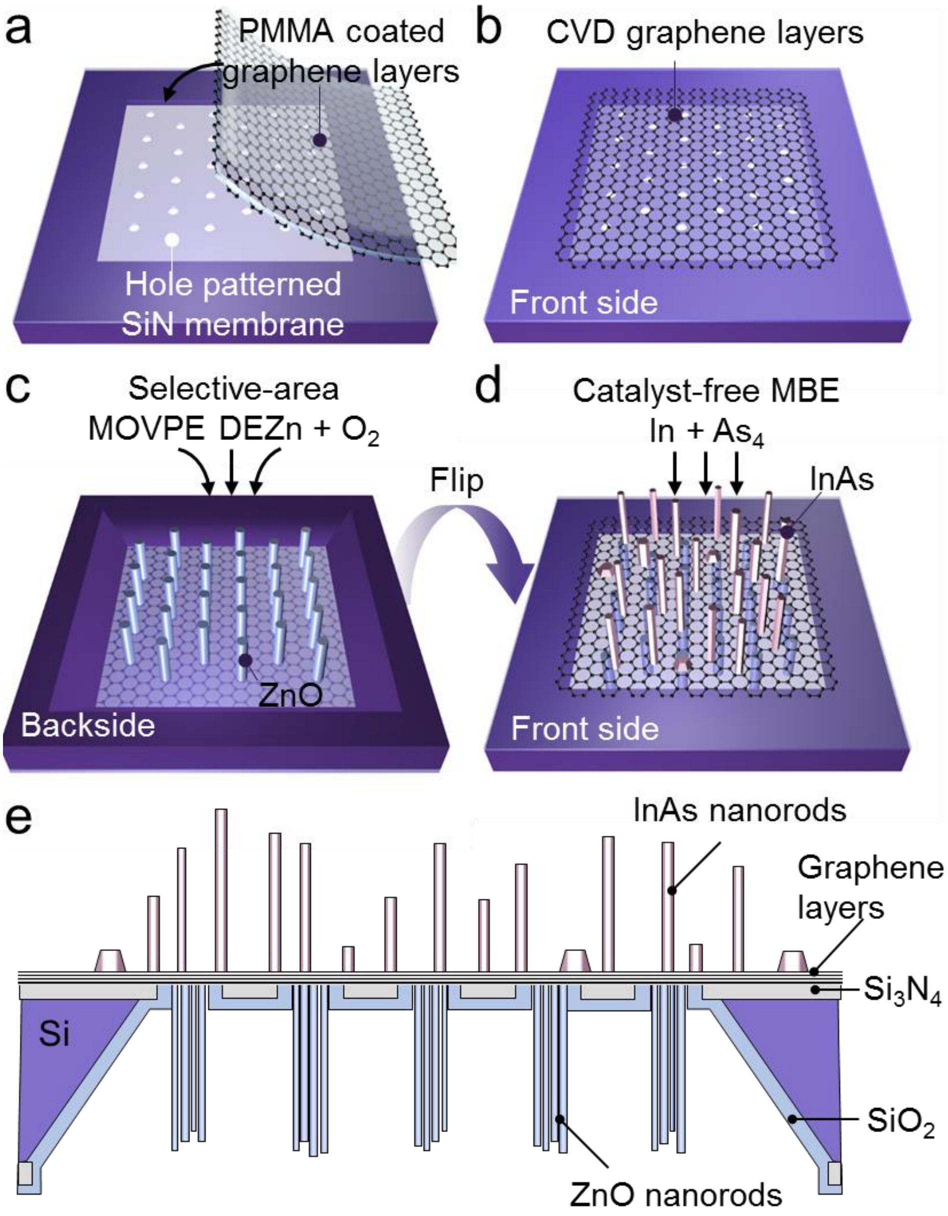

Figure B.1. The schematics of the fabrication processes of InAs nanorods/graphene layers/ZnO nanorods hybrid dimensional nanomaterials. (a) Transfer of PMMA coated CVD graphene layers on a hole patterned SiO_2/Si_3N_4

membrane. (b) CVD graphene layers transferred on SiO_2/Si_3N_4 membrane. (c) ZnO nanorods array growth on the backside by SA-MOVPE. (d) Catalyst-free MBE growth of InAs nanorods on the front side. (e) Cross-sectional schematic structures of the InAs nanorods/graphene layers/ZnO nanorods hybrid dimensional nanomaterials.

The schematic structure and scanning electron microscope images of the monolithically integrated ZnO/graphene layers/InAs double heterostructures can be seen in Figure B.1. Vertically well aligned ZnO nanostructures were first grown on the backside of suspended, chemical vapor deposited (CVD) graphene layers transferred on hole patterned Si_3N_4 membrane by MOVPE system, as shown in Figure B.1(a). Prior to ZnO growth, to improve the growth selectivity of ZnO, 50-nm-thick SiO_2 layer was coated on the backside of Si_3N_4 membrane by PECVD. After growing ZnO, we flipped the samples, so that graphene layers are facing upside, and loaded them in III-As MBE chamber. In this configuration, the surface of CVD graphene layers/ZnO heterostructures were exposed to In and As_4 fluxes inside MBE. For the growth of InAs nanorods on graphene layers, As flux of 3×10^{-5} torr was supplied on the substrates at the temperature of 460°C. Growth of InAs nanorods was initiated by supplying In flux of 1×10^{-7} torr, and growth of InAs was carried out for 35 min. The detailed MBE growth method of InAs nanorods on graphene layers can be found elsewhere.[17]

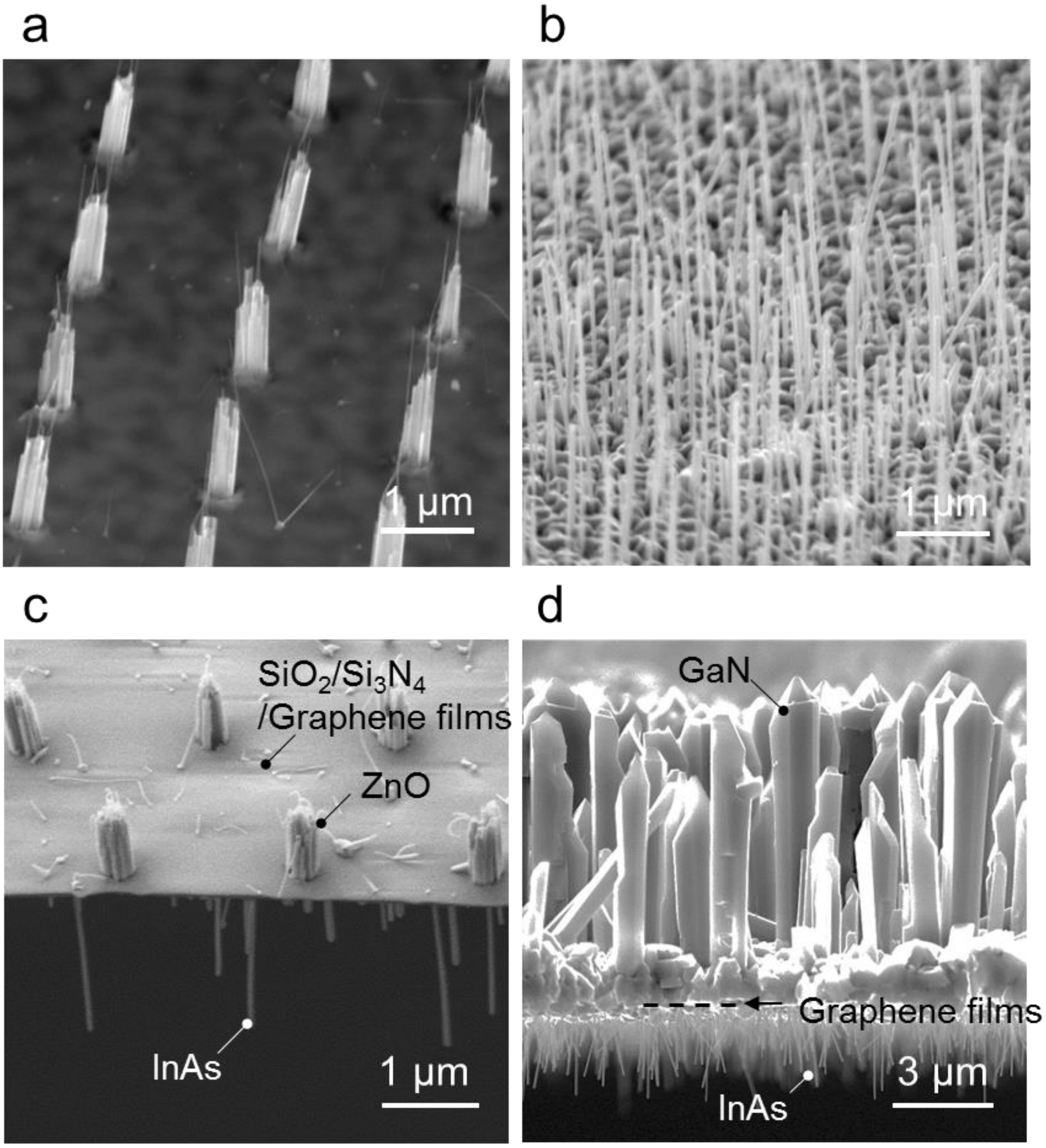

Figure B.2. Morphology of the InAs nanorods/graphene layers/ZnO nanorods hybrid dimensional nanomaterials. Tilted FE-SEM images of (a) ZnO nanostructure array on the front side, (b) InAs nanorods on the backside, and (c) the cross-section. (d) Side view FE-SEM image of the InAs nanorods/graphene layers/ZnO/GaN microrods.

The cross-sectional scanning electron microscope images of as-grown InAs/graphene layers/ZnO double heterostructure can be seen in the tilted SEM image in Figure B.2(c), and the tilted SEM image of the double heterostructure imaged from the ZnO side and InAs side of graphene layers can be seen in Figures B.2(a) and (b). From these SEM images we can see that vertically well-aligned ZnO and InAs nanostructures were grown on each side of freestanding graphene layers suspended on the hole patterned Si_3N_4 membrane. The ZnO nanostructures were selectively grown only on graphene layers and they were not nucleated on SiO_2/Si_3N_4 layers. We later confirmed that ZnO nanostructures were actually composed of nanowires and nanowalls which will be shown later in this paper by microstructural analysis. The InAs nanorods grown on the backside of the graphene layers/ZnO heterostructures had uniform density and they did not showed any difference in growth behavior over different regions. That is, during the growth, InAs did not seem to have interaction with the ZnO nanostructures nucleated on the opposite side. We suspect that the multilayer graphene (MLG) screened the interaction over its 5 nm thickness.

Besides the ZnO/MLG/InAs double heterostructures, we were able to demonstrate double heterostructure composed of GaN/MLG/InAs, as shown in Figure B.2(d). For the fabrication of this structure, GaN microrods were grown on CVD graphene layers/SiO_2/Si by MOVPE.[46] The GaN/MLG layers were lifted-off from the original substrate by chemically etching the underlying SiO_2 layers using buffered oxide etchant (BOE) and they were transferred in a suspended form on Si substrate with $300 \times 300\ \mu m^2$ square window openings. Due to the 1-μm-thick continuous GaN buffer layers, the GaN/MLG structure was successfully suspended without being broken on this square window. Loading this sample in a flipped manner, InAs nanorods were grown on the backside of the graphene layers/GaN heterostructures using the same MBE growth method described above. SEM image shown in Figure

B.2(d) shows that InAs nanorods and GaN microrods were vertically grown on each side of graphene layers in $(111)_{\mathrm{InAs}}$ and $(001)_{\mathrm{GaN}}$ directions.

The microstructural characteristics of InAs/MLG/ZnO double heterostructure were investigated by cross-sectional transmission electron microscopy (TEM) in Figure B.3. Bright-field (BF) cross-sectional TEM image in Figure B.3(a) clearly shows vertically grown ZnO nanostructures on graphene layers and vertical InAs nanorods and nanoislands grown under the graphene layers. To analyze the interface between InAs nanorods/MLG/ZnO nanostructure, we took high-resolution (HR) TEM images near the red bracket marked region in Figure B.3(a). HR-TEM images in Figures B.3(b) clearly show that InAs nanorods and ZnO nanostructures were heteroepitaxially grown in single crystal on each side of MLG without any interfacial layers or gap. The lattice spacing between adjacent planes were 0.26, 0.34 and 0.35 nm, corresponding to the *d*-spacing of ZnO(0002), graphene layers(0002) and InAs(111) planes.[17, 18] The diffraction patterns (DP) in Figures B.2(c-d) were obtained with a selective aperture size of 150 nm from ZnO, ZnO/MLG/InAs interface, and InAs nanorod, respectively. Figure B.3(c) shows DP of ZnO taken at the zone axis near $[2\bar{1}10]$ direction, where we observed that single crystal ZnO were grown along the *c*-axis of wurtzite. The streaky DP shown in Figure B.3(e) were taken from the InAs nanorod near the zone axis of $[11\bar{2}0]_{\mathrm{WZ}}$, $[1\bar{1}0]_{\mathrm{ZB}}$, which indicates that InAs nanorods were grown along the (111) direction. The streaky DP indicates the typical stacking faults observed in InAs nanorods. From the DP taken near the interface of ZnO/MLG/InAs shown in Figure B.3(d), we can see the overlapped DP of ZnO and InAs crystal. From these DPs, we were able to see the epitaxial relation of InAs(111) || MLG(0002) || ZnO(0002) and InAs$[10\bar{1}0]$ || MLG$[10\bar{1}0]$ || ZnO$[10\bar{1}0]$.

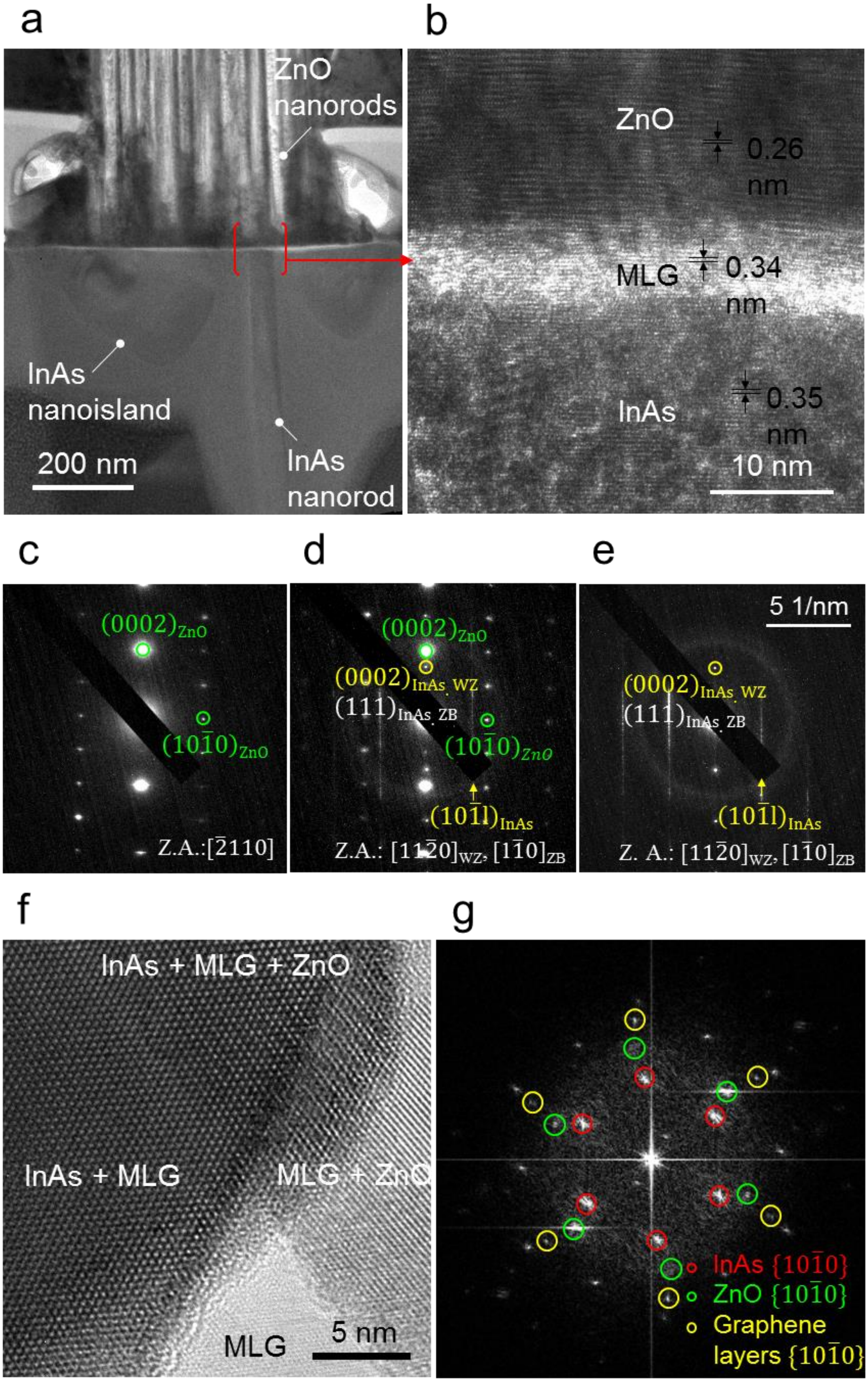
a
ZnO nanorods
InAs nanoisland
200 nm
InAs nanorod
b
ZnO
0.26 nm
MLG
0.34 nm
InAs
0.35 nm
10 nm
c
$(0002)_{ZnO}$
$(10\bar{1}0)_{ZnO}$
Z.A.:[$\bar{2}$110]
d
$(0002)_{ZnO}$
$(0002)_{InAs\_WZ}$
$(111)_{InAs\_ZB}$
$(10\bar{1}0)_{ZnO}$
$(10\bar{1}\bar{1})_{InAs}$
Z.A.: $[11\bar{2}0]_{WZ}$, $[1\bar{1}0]_{ZB}$
e
5 1/nm
$(0002)_{InAs\_WZ}$
$(111)_{InAs\_ZB}$
$(10\bar{1}\bar{1})_{InAs}$
Z. A.: $[11\bar{2}0]_{WZ}$, $[1\bar{1}0]_{ZB}$
f
InAs + MLG + ZnO
InAs + MLG
MLG + ZnO
MLG
5 nm
g
InAs {10$\bar{1}$0}
ZnO {10$\bar{1}$0}
Graphene layers {10$\bar{1}$0}

Figure B.3. Cross-sectional TEM analysis of the hybrid heterostructures. (a) Bright-field and (b) high-resolution TEM images of the hybrid heterostructures around ZnO nanorods/MLG/InAs nanorod interface. Diffraction pattern with a selective aperture size of 150 nm around the (c) ZnO nanorods, (d) ZnO/MLG/InAs interface, and (e) InAs nanorod. Plan view TEM structural analysis of the double heterostructures. (f) High-resolution plan view TEM image where an InAs nuclei overlapped ZnO nuclei. (g) The corresponding fast-Fourier transform of (f).

Furthermore, we measured plan view TEM of the InAs/MLG/ZnO double heterostructure to directly observe the in plane epitaxial relation between these crystals in Figure B.3. For plan view TEM observation, we prepared another double heterostructures with nanoscale ZnO and InAs nuclei. ZnO nuclei were grown only for 2 min and InAs nuclei were grown for 30 sec, so that the size of each nucleus were less than 50 nm. In here, the suspended graphene layers acted both as a growth substrate and as an electron beam transparent substrate.[96, 106] Figure B.3(a) shows the plan view HR-TEM image of the double heterostructure near the point of intersection of InAs, MLG, and ZnO single crystals. A hexagonal lattice arrays of InAs, ZnO, and MLG can be clearly seen in this HR-TEM image. On the upper side of the HR-TEM image, three different crystals, InAs/MLG/ZnO, were overlapped and on the left and right side of the image, InAs/MLG and MLG/ZnO can be seen, respectively. On the lower side of the HR-TEM image, we can observe the periodic lattice structure of MLG. The corresponding fast-Fourier transform (FFT) image of the HR-TEM image in Figure B.3(a) can be seen in Figure B.3(b), from which it became clear that ZnO, graphene layers, and InAs were grown heteroepitaxially integrated. We again confirmed the in plane epitaxial relationship of InAs $(10\bar{1}0)$ || MLG $(10\bar{1}0)$ || ZnO$(10\bar{1}0)$ from this FFT image.

To further confirm the monolithic integration of the double heterostructure, we performed compositional analysis by scanning TEM (STEM) equipped with energy-dispersive X-ray spectroscopy (EDX) as shown in Figure B.4. The STEM-EDX mapping analysis showed the clear formation and spatial separation between InAs and ZnO, as shown in Figures B.4(a-f). Additionally, Figure B.4(j) shows the EDX line profiles, measured from the red line normal to the graphene layers in the STEM image of Figure B.4(a). The chemical composition of GaN/MLG/InAs double heterostructure was also investigated as well in the STEM and STEM-EDS mapping images in Figures B.4(g-i). We observed a clearly separated nitride and arsenic semiconductor layers on each sides of thin MLG. Because the MLG was thin and considerable amount of carbon contaminations were formed on the sample during TEM sampling, it was difficult to characterize the graphene layers in the STEM-EDX mapping analysis in this magnification.

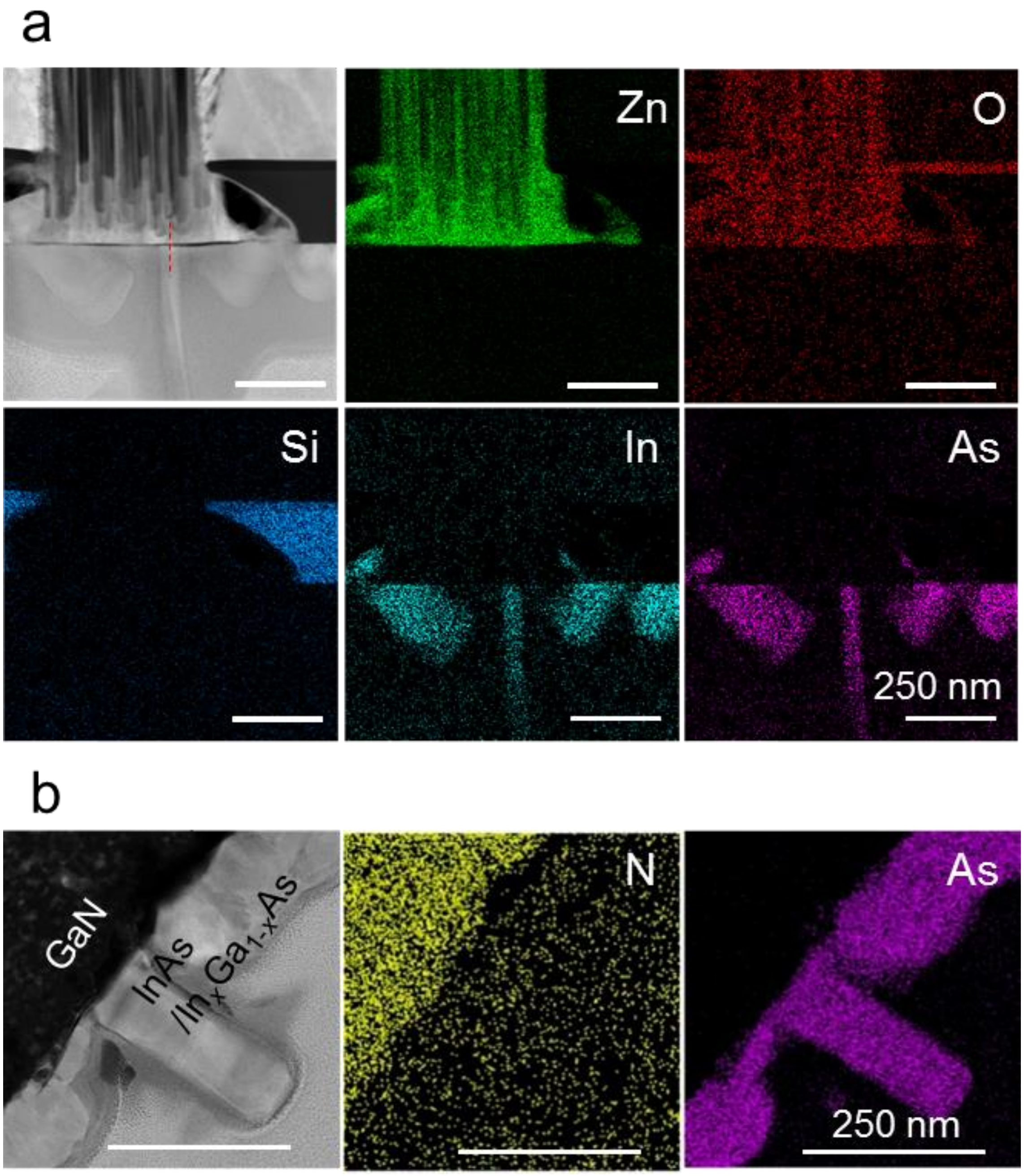

Figure B.4. Chemical analysis of the double heterostructure. (a) Scanning TEM (STEM) image of ZnO/MLG/InAs double heterostructure and the corresponding STEM-EDS mapping images of (b) Zn, (c) O, (d) Si, (e) In, and (f) As. (g) STEM image of GaN/ZnO/MLG/InAs double heterostructure and the corresponding STEM-EDS mapping images of (h) N and (i) As. (j) STEM-EDS line profile of Zn, O, In, and As taken along the dotted line in (a).

B.2.2. Dual wavelength photodetector device characteristics

Optoelectronic characteristics of these new material system were investigated by fabricating photodetector device using ZnO nanorods/graphene layers/InAs nanorods hybrid heterostructures and measuring their device characteristics. The schematic illustration of the structure of photodetector is shown in Figure B.5. PI layers were filled on both surfaces of the graphene films and the surface of PI layers were etched by oxygen plasma to expose the tips of ZnO and InAs nanorods. Semitransparent Au electrodes as Schottky contact with thickness of 20 and 50 nm was deposited on ZnO and InAs nanorods, respectively. Ohmic contact was formed on CVD graphene layers using silver paste. The $I-V$ characteristic curves between these three electrodes were measured as shown in Figure B.5(b). Schottky diode characteristics with clear rectifying behavior and turn-on voltage near 0.2 V was observed for $I-V$ characteristic curve in Au-ZnO nanorods-MLG device. For the Au-InAs nanorods-MLG device, although the device showed asymmetric $I-V$ curve, due to the small band gap of InAs, non-ideal diode characteristics with considerably high current level at reverse bias voltages were observed. When measuring the $I-V$ characteristic curve between Au-ZnO-MLG-InAs-Au, $I-V$ curve displayed as if the above two $I-V$ curves were connected in series; the overall resistance increased and Schottky diode characteristics were observed.

The spectral response of the Schottky photodiodes were investigated as shown in Figures B.5(c) and (d). Figure B.5(c) shows the spectral response of Au-InAs-MLG device measured by Fourier-transform infrared spectroscopy (FT-IR) at 77 K. The device generated photocurrent above 0.5 eV and their peak responsivity was observed near 0.6 eV. Figure B.5(d) shows the typical spectral response of Au-ZnO nanorods-MLG Schottky photodiode measured at room temperature. For the Au-ZnO-MLG Schottky photodiode, responsivity of the device rapidly increased above 3.0 eV, indicating clear spectral sensitivity to UV light. The measurement setup was not established yet to characterize the Au-ZnO-MLG device from the double heterostructure, so the typical spectral response from another ZnO nanorod arrays on CVD graphene layers/SiO_2/Si was presented in Figure B.5(d). The measurement setup would be improved and the spectral response of Au-ZnO nanorods-MLG will be measured directly from the double heterostructure. These results indicates that, using these double heterostructure composed of wide and narrow band gap semiconductor nanostructures, photocurrents can be generated at two distinct spectral ranges. This characteristics are highly desirable for broadband solar cell applications.

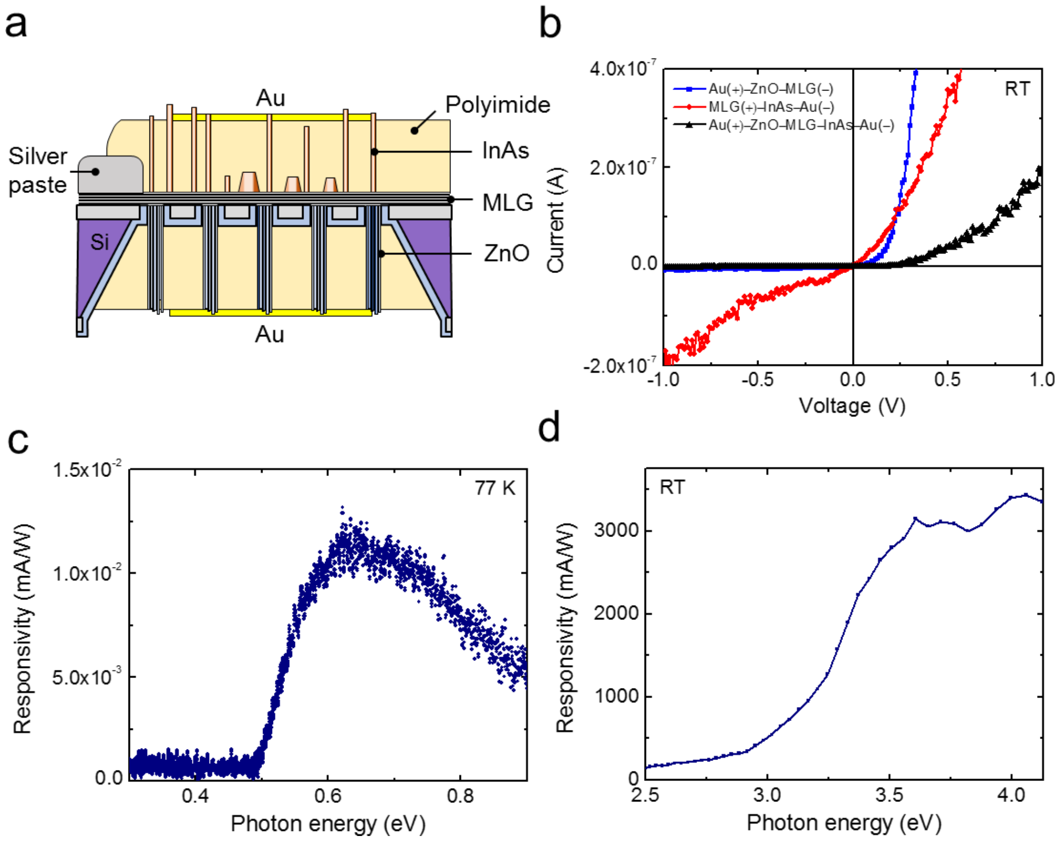

Figure B.5. Dual-wavelength photodetector device. (a) Schematics of the device structure (b) *I*−*V* characteristics. (c) Spectral photoresponse of InAs nanorod-graphene layers measured at 77 K in FT-IR. (d) Typical spectral response measured from another ZnO nanorods-graphene layers/SiO_2/Si (not from the double heterostructure) at room temperature.

B.3. Summary

In conclusion, we demonstrated the monolithic, epitaxial growth of single crystalline wide and narrow band gap semiconductors on and under graphene layers. We used catalyst-free direct growth method to integrate these materials on graphene layers, so there were neither interfacial layers nor gap observed in the interfacial layer. Cross-sectional and plan view TEM analysis showed the successful and heteroepitaxial integration of ZnO/MLG/InAs double heterostructure using the suspended graphene layers as a epitaxial substrate opened on both sides. The compositional analysis further confirmed the well-formed double heterostructures composed of ZnO/MLG/InAs as well as GaN/MLG/InAs. We showed that by using double-sided graphene layers as an epitaxial substrate for various types of semiconductors, it is possible to monolithically and epitaxially integrate high quality wide and narrow band gap semiconductors. Using this growth method described above, we can have more combination of semiconductors with different band gap energies, which can be used for advanced electronic and optoelectronic device application such as tandem cell and multicolor light emitters.

References

1. Lee, C.-H., Hong, Y. J., Kim, Y.-J., Yoo, J., Baek, H., Jeon, S.-R., Lee, S.-J., Yi, G.-C., GaN/ZnO nanotube heterostructure light-emitting diodes fabricated on Si, *IEEE Journal of Selected Topics in Quantum Electronics* **17**, 966-970 (2011).

2. Choi, J. H., Ahn, H. Y., Lee, Y. S., Park, K., Kim, T.-H., Cho, K. S., Baik, C. W., Kim, S. I., Yoo, H., Lee, E. H., GaN light-emitting diodes on glass substrates with enhanced electroluminescence, *Journal of Materials Chemistry* **22**, 22942-22948 (2012).

3. Tchoe, Y., Jo, J., Kim, M., Heo, J., Yoo, G., Sone, C., Yi, G.-C., Variable-Color Light-Emitting Diodes Using GaN Microdonut arrays, *Advanced Materials* **26**, 3019-3023 (2014).

4. Lu, W., Lieber, C. M., Nanoelectronics from the bottom up, *Nature materials* **6**, 841 (2007).

5. Yi, G.-C., *Semiconductor Nanostructures for Optoelectronic Devices: Processing, Characterization and Applications*, Springer Science & Business Media, (2012).

6. Zhang, A., Zheng, G., Lieber, C. M., *Nanowires*, Springer (2016).

7. Tomioka, K., Yoshimura, M., Fukui, T., A III-V nanowire channel on silicon for high-performance vertical transistors, *Nature* **488**, 189-192 (2012).

8. Krogstrup, P., Jørgensen, H. I., Heiss, M., Demichel, O., Holm, J. V., Aagesen, M., Nygard, J., i Morral, A. F., Single-nanowire solar cells beyond the Shockley-Queisser limit, *Nature Photonics* **7**, 306-310 (2013).

9. Park, J. B., Oh, H., Park, J., Kim, N.-J., Yoon, H., Yi, G.-C., Scalable ZnO nanotube arrays grown on CVD-graphene films, *APL Materials* **4**, 106104 (2016).

10. Lee, C.-H., Kim, Y. J., Hong, Y. J., Jeon, S. R., Bae, S., Hong, B. H., Yi, G.-C., Flexible Inorganic Nanostructure Light-Emitting Diodes Fabricated on Graphene Films, *Advanced materials* **23**, 4614-4619 (2011).

11. Mohseni, P. K., Behnam, A., Wood, J. D., Zhao, X., Yu, K. J., Wang, N. C., Rockett, A., Rogers, J. A., Lyding, J. W., Pop, E., Monolithic III-V nanowire solar cells on graphene via direct van der waals epitaxy, *Advanced Materials* **26**, 3755-3760 (2014).

12. Li, X., Cai, W., An, J., Kim, S., Nah, J., Yang, D., Piner, R., Velamakanni, A., Jung, I., Tutuc, E., Large-area synthesis of high-quality and uniform graphene films on copper foils, *Science* **324**, 1312-1314 (2009).

13. Kim, K. S., Zhao, Y., Jang, H., Lee, S. Y., Kim, J. M., Kim, K. S., Ahn, J.-H., Kim, P., Choi, J.-Y., Hong, B. H., Large-scale pattern growth of graphene films for stretchable transparent electrodes, *Nature* **457**, 706 (2009).

14. Bae, S., Kim, H., Lee, Y., Xu, X., Park, J.-S., Zheng, Y., Balakrishnan, J., Lei, T., Kim, H. R., Song, Y. I., Roll-to-roll production of 30-inch graphene films for transparent electrodes, *Nature nanotechnology* **5**, 574-578 (2010).

15. Kim, Y.-J., Lee, J.-H., Yi, G.-C., Vertically aligned ZnO nanostructures grown on graphene layers, *Applied Physics Letters* **95**, 213101 (2009).

16. Chung, K., Lee, C.-H., Yi, G.-C., Transferable GaN layers grown on ZnO-coated graphene layers for optoelectronic devices, *Science* **330**, 655-657 (2010).

17. Tchoe, Y., Jo, J., Kim, M., Yi, G.-C., Catalyst-free growth of InAs/InxGa1− xAs coaxial nanorod heterostructures on graphene layers using molecular beam epitaxy, *NPG Asia Materials* **7**, e206 (2015).

18. Kim, Y. J., Yoo, H., Lee, C.-H., Park, J. B., Baek, H., Kim, M., Yi, G.-C., Position- and Morphology-Controlled ZnO Nanostructures Grown on Graphene Layers, *Advanced Materials* **24**, 5565-5569 (2012).

19. Duan, X., Huang, Y., Cui, Y., Wang, J., Lieber, C. M., Indium phosphide nanowires as building blocks for nanoscale electronic and optoelectronic devices, *Nature* **409**, 66-69 (2001).

20. Park, W. I., Kim, J. S., Yi, G.-C., Lee, H. J., ZnO nanorod logic circuits, *Advanced materials* **17**, 1393-1397 (2005).

21. Qian, F., Gradecak, S., Li, Y., Wen, C.-Y., Lieber, C. M., Core/multishell nanowire heterostructures as multicolor, high-efficiency light-emitting diodes, *Nano letters* **5**, 2287-2291 (2005).

22. Zhong, Z., Wang, D., Cui, Y., Bockrath, M. W., Lieber, C. M., Nanowire crossbar arrays as address decoders for integrated nanosystems, *Science* **302**, 1377-1379 (2003).

23. Yao, J., Yan, H., Lieber, C. M., A nanoscale combing technique for the large-scale assembly of highly aligned nanowires, *Nature nanotechnology* **8**, 329 (2013).

24. Park, W. I., Kim, D. H., Jung, S.-W., Yi, G.-C., Metalorganic vapor-phase epitaxial growth of vertically well-aligned ZnO nanorods, *Applied Physics Letters* **80**, 4232-4234 (2002).

25. An, S. J., Yi, G.-C., Near ultraviolet light emitting diode composed of *n*-GaN/ ZnO coaxial nanorod heterostructures on a *p*-GaN layer, *Applied Physics Letters* **91**, 123109 (2007).

26. Lee, C.-H., Yoo, J., Hong, Y. J., Cho, J., Kim, Y. J., Jeon, S. R., Baek, J. H., Yi, G.-C., GaN/$In_{1-x}Ga_xN$/GaN/ZnO nanoarchitecture light emitting diode microarrays, *Applied Physics Letters* **94**, 213101 (2009).

27. Hong, Y. J., Jung, H. S., Yoo, J., Kim, Y. J., Lee, C.-H., Kim, M., Yi, G.-C., Shape-Controlled Nanoarchitectures Using Nanowalls, *Advanced Materials* **21**, 222-226 (2009).

28. Wu, W., Wen, X., Wang, Z. L., Taxel-addressable matrix of vertical-nanowire piezotronic transistors for active and adaptive tactile imaging, *Science* **340**, 952-957 (2013).

29. Liu, R., Chen, R., Elthakeb, A. T., Lee, S. H., Hinckley, S., Khraiche, M. L., Scott, J., Pre, D., Hwang, Y., Tanaka, A., High Density Individually Addressable Nanowire Arrays Record Intracellular Activity from Primary Rodent and Human Stem Cell Derived Neurons, *Nano Letters* **17**, 2757-2764 (2017).

30. Su, Y., Liu, C., Brittman, S., Tang, J., Fu, A., Kornienko, N., Kong, Q., Yang, P.,

Single-nanowire photoelectrochemistry, *Nature nanotechnology* **11**, 609 (2016).

31. Ma, D., Lee, C., Au, F., Tong, S., Lee, S., Small-diameter silicon nanowire surfaces, *Science* **299**, 1874-1877 (2003).

32. Cui, Y., Lauhon, L. J., Gudiksen, M. S., Wang, J., Lieber, C. M., Diameter-controlled synthesis of single-crystal silicon nanowires, *Applied Physics Letters* **78**, 2214-2216 (2001).

33. Li, Y., Qian, F., Xiang, J., Lieber, C. M., Nanowire electronic and optoelectronic devices, *Materials today* **9**, 18-27 (2006).

34. Heilmann, M., Sarau, G., Göbelt, M., Latzel, M., Sadhujan, S., Tessarek, C., Christiansen, S., Growth of GaN Micro-and Nanorods on Graphene-Covered Sapphire: Enabling Conductivity to Semiconductor Nanostructures on Insulating Substrates, *Crystal Growth & Design* **15**, 2079-2086 (2015).

35. Hong, Y. J., Fukui, T., Controlled van der Waals heteroepitaxy of InAs nanowires on carbon honeycomb lattices, *ACS nano* **5**, 7576-7584 (2011).

36. Munshi, A. M., Dheeraj, D. L., Fauske, V. T., Kim, D.-C., van Helvoort, A. T., Fimland, B.-O., Weman, H., Vertically aligned GaAs nanowires on graphite and few-layer graphene: generic model and epitaxial growth, *Nano letters* **12**, 4570-4576 (2012).

37. Chung, K., Yoo, H., Hyun, J. K., Oh, H., Tchoe, Y., Lee, K., Baek, H., Kim, M., Yi, G.-C., Flexible GaN Light-Emitting Diodes Using GaN Microdisks Epitaxial Laterally Overgrown on Graphene Dots, *Advanced Materials* **28**, 7688-7694 (2016).

38. Yokota, T., Zalar, P., Kaltenbrunner, M., Jinno, H., Matsuhisa, N., Kitanosako, H., Tachibana, Y., Yukita, W., Koizumi, M., Someya, T., Ultraflexible organic photonic skin, *Science advances* **2**, e1501856 (2016).

39. Park, S.-I., Xiong, Y., Kim, R.-H., Elvikis, P., Meitl, M., Kim, D.-H., Wu, J., Yoon, J., Yu, C.-J., Liu, Z., Printed assemblies of inorganic light-emitting diodes for deformable and semitransparent displays, *Science* **325**, 977-981 (2009).

40. Tchoe, Y., Lee, C.-H., Park, J. B., Baek, H., Chung, K., Jo, J., Kim, M., Yi, G.-C., Microtube Light-Emitting Diode Arrays with Metal Cores, *ACS nano* **10**, 3114-3120 (2016).

41. Mohseni, P. K., Behnam, A., Wood, J. D., English, C. D., Lyding, J. W., Pop, E., Li, X., $In_xGa_{1-x}As$ Nanowire Growth on Graphene: van der Waals Epitaxy Induced Phase Segregation, *Nano letters* **13**, 1153-1161 (2013).

42. Zhuang, Q. D., Anyebe, E. A., Sanchez, A. M., Rajpalke, M. K., Veal, T. D., Zhukov, A., Robinson, B. J., Anderson, F., Kolosov, O., Fal'ko, V., Graphitic platform for self-catalysed InAs nanowires growth by molecular beam epitaxy, *Nanoscale research letters* **9**, 1-7 (2014).

43. Park, W., Yi, G.-C., Kim, J.-W., Park, S.-M., Schottky nanocontacts on ZnO nanorod arrays, *Applied Physics Letters* **82**, 4358-4360 (2003).

44. Song, S. M., Park, J. K., Sul, O. J., Cho, B. J., Determination of work function of graphene under a metal electrode and its role in contact resistance, *Nano letters* **12**, 3887-3892 (2012).

45. Cho, B., Kim, T. W., Song, S., Ji, Y., Jo, M., Hwang, H., Jung, G. Y., Lee, T., Rewritable switching of one diode–one resistor nonvolatile organic memory devices, *Advanced Materials* **22**, 1228-1232 (2010).

46. Chung, K., Beak, H., Tchoe, Y., Oh, H., Yoo, H., Kim, M., Yi, G.-C., Growth and characterizations of GaN micro-rods on graphene films for flexible light emitting diodes, *Apl Materials* **2**, 092512 (2014).

47. Fan, Z., Razavi, H., Do, J.-w., Moriwaki, A., Ergen, O., Chueh, Y.-L., Leu, P. W., Ho, J. C., Takahashi, T., Reichertz, L. A., Three-dimensional nanopillar-array photovoltaics on low-cost and flexible substrates, *Nature materials* **8**, 648 (2009).

48. Wang, Z. L., Song, J., Piezoelectric nanogenerators based on zinc oxide nanowire arrays, *Science* **312**, 242-246 (2006).

49. Hong, Y. J., Jeon, J.-M., Kim, M., Jeon, S.-R., Park, K. H., Yi, G.-C., Structural and optical characteristics of GaN/ZnO coaxial nanotube heterostructure arrays

for light-emitting device applications, *New Journal of Physics* **11**, 125021 (2009).

50. Li, Q., Westlake, K. R., Crawford, M. H., Lee, S. R., Koleske, D. D., Figiel, J. J., Cross, K. C., Fathololoumi, S., Mi, Z., Wang, G. T., Optical performance of top-down fabricated InGaN/GaN nanorod light emitting diode arrays, *Optics express* **19**, 25528-25534 (2011).

51. Koester, R., Hwang, J.-S., Salomon, D., Chen, X., Bougerol, C., Barnes, J.-P., Dang, D. L. S., Rigutti, L., de Luna Bugallo, A., Jacopin, G., M-plane core–shell InGaN/GaN multiple-quantum-wells on GaN wires for electroluminescent devices, *Nano letters* **11**, 4839-4845 (2011).

52. Colby, R., Liang, Z., Wildeson, I. H., Ewoldt, D. A., Sands, T. D., García, R. E., Stach, E. A., Dislocation filtering in GaN nanostructures, *Nano letters* **10**, 1568-1573 (2010).

53. Kang, M. S., Lee, C.-H., Park, J. B., Yoo, H., Yi, G.-C., Gallium nitride nanostructures for light-emitting diode applications, *Nano energy* **1**, 391-400 (2012).

54. Joshi, R. K., Schneider, J. J., Assembly of one dimensional inorganic nanostructures into functional 2D and 3D architectures. Synthesis, arrangement and functionality, *Chemical Society Reviews* **41**, 5285-5312 (2012).

55. Mazid Munshi, A., Weman, H., Advances in semiconductor nanowire growth on graphene, *physica status solidi (RRL)-Rapid Research Letters* **7**, 713-726 (2013).

56. Lee, J. M., Choung, J. W., Yi, J., Lee, D. H., Samal, M., Yi, D. K., Lee, C.-H., Yi, G.-C., Paik, U., Rogers, J. A., Vertical pillar-superlattice array and graphene hybrid light emitting diodes, *Nano letters* **10**, 2783-2788 (2010).

57. Svensson, C. P. T., Mårtensson, T., Trägårdh, J., Larsson, C., Rask, M., Hessman, D., Samuelson, L., Ohlsson, J., Monolithic GaAs/InGaP nanowire light emitting diodes on silicon, *Nanotechnology* **19**, 305201 (2008).

58. Mohseni, P. K., Kim, S. H., Zhao, X., Balasundaram, K., Kim, J. D., Pan, L., Rogers, J. A., Coleman, J. J., Li, X., GaAs pillar array-based light emitting diodes

fabricated by metal-assisted chemical etching, *Journal of Applied Physics* **114**, 064909 (2013).

59. Tomioka, K., Motohisa, J., Hara, S., Hiruma, K., Fukui, T., GaAs/AlGaAs core multishell nanowire-based light-emitting diodes on Si, *Nano letters* **10**, 1639-1644 (2010).

60. Ra, Y.-H., Navamathavan, R., Park, J.-H., Lee, C.-R., Coaxial $In_xGa_{1-x}N$/GaN Multiple Quantum Well Nanowire Arrays on Si (111) Substrate for High-Performance Light-Emitting Diodes, *Nano letters* **13(8)**, 3506-3516 (2013).

61. Funato, M., Hayashi, K., Ueda, M., Kawakami, Y., Narukawa, Y., Mukai, T., Emission color tunable light-emitting diodes composed of InGaN multifacet quantum wells, *Applied Physics Letters* **93**, 021126 (2008).

62. Sekiguchi, H., Kishino, K., Kikuchi, A., Emission color control from blue to red with nanocolumn diameter of InGaN/GaN nanocolumn arrays grown on same substrate, *Applied Physics Letters* **96**, 231104 (2010).

63. Hong, Y. J., Lee, C.-H., Yoon, A., Kim, M., Seong, H. K., Chung, H. J., Sone, C., Park, Y. J., Yi, G.-C., Visible-Color-Tunable Light-Emitting Diodes, *Advanced Materials* **23**, 3284-3288 (2011).

64. Waltereit, P., Brandt, O., Trampert, A., Grahn, H., Menniger, J., Ramsteiner, M., Reiche, M., Ploog, K., Nitride semiconductors free of electrostatic fields for efficient white light-emitting diodes, *Nature* **406**, 865-868 (2000).

65. Kishino, K., Nagashima, K., Yamano, K., Monolithic Integration of InGaN-Based Nanocolumn Light-Emitting Diodes with Different Emission Colors, *Applied Physics Express* **6**, 012101 (2013).

66. Limbach, F., Hauswald, C., Lähnemann, J., Wölz, M., Brandt, O., Trampert, A., Hanke, M., Jahn, U., Calarco, R., Geelhaar, L., Current path in light emitting diodes based on nanowire ensembles, *Nanotechnology* **23**, 465301 (2012).

67. Li, C.-K., Yang, H.-C., Hsu, T.-C., Shen, Y.-J., Liu, A.-S., Wu, Y.-R., Three dimensional numerical study on the efficiency of a core-shell InGaN/GaN

multiple quantum well nanowire light-emitting diodes, *Journal of Applied Physics* **113**, 183104 (2013).

68. Ko, Y.-H., Song, J., Leung, B., Han, J., Cho, Y.-H., Multi-color broadband visible light source via GaN hexagonal annular structure, *Scientific reports* **4**, 5514 (2014).
69. Park, S. I., Xiong, Y. J., Kim, R. H., Elvikis, P., Meitl, M., Kim, D. H., Wu, J., Yoon, J., Yu, C. J., Liu, Z. J., Huang, Y. G., Hwang, K., Ferreira, P., Li, X. L., Choquette, K., Rogers, J. A., Printed Assemblies of Inorganic Light-Emitting Diodes for Deformable and Semitransparent Displays, *Science* **325**, 977-981 (2009).
70. Jiang, H., Jin, S., Li, J., Shakya, J., Lin, J., III-nitride blue microdisplays, *Applied Physics Letters* **78**, 1303-1305 (2001).
71. Ponce, F., Bour, D., Nitride-based semiconductors for blue and green light-emitting devices, *Nature* **386**, 351-359 (1997).
72. Nakamura, S., The roles of structural imperfections in InGaN-based blue light-emitting diodes and laser diodes, *Science* **281**, 956-961 (1998).
73. Chung, K., Park, S. I., Baek, H., Chung, J.-S., Yi, G.-C., High-quality GaN films grown on chemical vapor-deposited graphene films, *NPG Asia Materials* **4**, e24 (2012).
74. Schubert, E. F., Kim, J. K., Solid-state light sources getting smart, *Science* **308**, 1274-1278 (2005).
75. Schubert, E. F., Gessmann, T., Kim, J. K., *Light emitting diodes*, Wiley Online Library (2005).
76. Tsao, J. Y., Solid-state lighting: lamps, chips, and materials for tomorrow, *IEEE Circuits and Devices Magazine* **20**, 28-37 (2004).
77. Krames, M. R., Shchekin, O. B., Mueller-Mach, R., Mueller, G. O., Zhou, L., Harbers, G., Craford, M. G., Status and future of high-power light-emitting diodes for solid-state lighting, *Journal of display technology* **3**, 160-175 (2007).

78. Tsintzos, S., Pelekanos, N., Konstantinidis, G., Hatzopoulos, Z., Savvidis, P., A GaAs polariton light-emitting diode operating near room temperature, *Nature* **453**, 372 (2008).

79. Ko, Y. H., Kim, J. H., Jin, L. H., Ko, S. M., Kwon, B. J., Kim, J., Kim, T., Cho, Y. H., Electrically Driven Quantum Dot/Wire/Well Hybrid Light-Emitting Diodes, *Advanced Materials* **23**, 5364 (2011).

80. Leung, B., Sun, Q., Yerino, C. D., Han, J., Coltrin, M. E., Using the kinetic Wulff plot to design and control nonpolar and semipolar GaN heteroepitaxy, *Semiconductor Science and Technology* **27**, 141101 (2012).

81. Bae, S. Y., Kim, D. H., Lee, D. S., Lee, S. J., Baek, J. H., Highly Integrated InGaN/GaN Semipolar Micro-Pyramid Light-Emitting Diode Arrays by Confined Selective Area Growth, *Electrochemical and Solid State Letters* **15**, H47-H50 (2012).

82. Choi, J. H., Zoulkarneev, A., Kim, S. I., Baik, C. W., Yang, M. H., Park, S. S., Suh, H., Kim, U. J., Son, H. B., Lee, J. S., Nearly single-crystalline GaN light-emitting diodes on amorphous glass substrates, *Nature Photonics* **5**, 763-769 (2011).

83. Ra, Y. H., Navamathavan, R., Park, J. H., Lee, C. R., Coaxial $In_xGa_{1-x}N$/GaN Multiple Quantum Well Nanowire Arrays on Si(111) Substrate for High-Performance Light-Emitting Diodes, *Nano Letters* **13**, 3506-3516 (2013).

84. Baek, H., Lee, C.-H., Chung, K., Yi, G.-C., Epitaxial GaN Microdisk Lasers Grown on Graphene Microdots, *Nano Letters* **13**, 2782-2785 (2013).

85. Harrison, P., *Quantum wells, wires and dots: theoretical and computational physics of semiconductor nanostructures,* John Wiley & Sons (2005).

86. Christmas, U. M., Andreev, A., Faux, D., Calculation of electric field and optical transitions in $In_xGa_{1-x}N$ quantum wells, *Journal of applied physics* **98**, 073522-073522-073512 (2005).

87. Lee, C.-H., Kim, Y.-J., Hong, Y. J., Jeon, S. R., Bae, S., Hong, B. H., Yi, G.-C.,

Flexible inorganic nanostructure light-emitting diodes fabricated on graphene films, *Advanced Materials* **23**, 4614-4619 (2011).

88. Kim, Y.-J., Yoo, H., Lee, C.-H., Park, J. B., Baek, H., Kim, M., Yi, G.-C., Position-and morphology-controlled ZnO nanostructures grown on graphene layers, *Advanced Materials* **24**, 5565-5569 (2012).

89. Hertenberger, S., Rudolph, D., Bolte, S., Döblinger, M., Bichler, M., Spirkoska, D., Finley, J., Abstreiter, G., Koblmüller, G., Absence of vapor-liquid-solid growth during molecular beam epitaxy of self-induced InAs nanowires on Si, *Applied Physics Letters* **98**, 123114 (2011).

90. Rudolph, D., Hertenberger, S., Bolte, S., Paosangthong, W., Spirkoska, D., Döblinger, M., Bichler, M., Finley, J. J., Abstreiter, G., Koblmüller, G., Direct observation of a noncatalytic growth regime for GaAs nanowires, *Nano letters* **11**, 3848-3854 (2011).

91. Koblmüller, G., Abstreiter, G., Growth and properties of InGaAs nanowires on silicon, *physica status solidi (RRL)-Rapid Research Letters* **8**, 11-30 (2014).

92. Hertenberger, S., Rudolph, D., Becker, J., Bichler, M., Finley, J., Abstreiter, G., Koblmüller, G., Rate-limiting mechanisms in high-temperature growth of catalyst-free InAs nanowires with large thermal stability, *Nanotechnology* **23**, 235602 (2012).

93. Mandl, B., Stangl, J., Hilner, E., Zakharov, A. A., Hillerich, K., Dey, A. W., Samuelson, L., Bauer, G., Deppert, K., Mikkelsen, A., Growth Mechanism of Self-Catalyzed Group III– V Nanowires, *Nano letters* **10**, 4443-4449 (2010).

94. Hong, Y. J., Lee, W. H., Wu, Y., Ruoff, R. S., Fukui, T., van der Waals epitaxy of InAs nanowires vertically aligned on single-layer graphene, *Nano letters* **12**, 1431-1436 (2012).

95. Takahashi, K., Morizumi, T., Growth of InAs whiskers in wurtzite structure, *Japanese Journal of Applied Physics* **5**, 657 (1966).

96. Hong, Y. J., Yang, J. W., Lee, W. H., Ruoff, R. S., Kim, K. S., Fukui, T., Van der

Waals epitaxial double heterostructure: InAs/single-layer graphene/InAs, *Advanced Materials* **25**, 6847-6853 (2013).

97. Wang, G.-C., Lu, T.-M., in *RHEED Transmission Mode and Pole Figures*, Springer (2014).

98. Wu, Y., Hao, Y., Jeong, H. Y., Lee, Z., Chen, S., Jiang, W., Wu, Q., Piner, R. D., Kang, J., Ruoff, R. S., Crystal structure evolution of individual graphene islands during CVD growth on copper foil, *Advanced Materials* **25**, 6744-6751 (2013).

99. Johansson, J., Wacaser, B. A., Dick, K. A., Seifert, W., Growth related aspects of epitaxial nanowires, *Nanotechnology* **17**, S355 (2006).

100. Larsson, M. W., Wagner, J. B., Wallin, M., Håkansson, P., Fröberg, L. E., Samuelson, L., Wallenberg, L. R., Strain mapping in free-standing heterostructured wurtzite InAs/InP nanowires, *Nanotechnology* **18**, 015504 (2007).

101. Hilner, E., Håkanson, U., Fröberg, L. E., Karlsson, M., Kratzer, P., Lundgren, E., Samuelson, L., Mikkelsen, A., Direct atomic scale imaging of III− V nanowire surfaces, *Nano letters* **8**, 3978-3982 (2008).

102. Stringfellow, G. B., *Organometallic vapor-phase epitaxy: theory and practice*, Academic Press (1999).

103. Herman, M. A., Sitter, H., *Molecular beam epitaxy: fundamentals and current status*, Vol. 7, Springer Science & Business Media (2012).

104. Mizuta, M., Fujieda, S., Matsumoto, Y., Kawamura, T., Low temperature growth of GaN and AlN on GaAs utilizing metalorganics and hydrazine, *Japanese journal of applied physics* **25**, L945 (1986).

105. Ryu, Y., Zhu, S., Look, D. C., Wrobel, J., Jeong, H., White, H., Synthesis of *p*-type ZnO films, *Journal of Crystal Growth* **216**, 330-334 (2000).

106. Jo, J., Yoo, H., Park, S. I., Park, J. B., Yoon, S., Kim, M., Yi, G.-C., High-Resolution Observation of Nucleation and Growth Behavior of Nanomaterials Using a Graphene Template, *Advanced Materials* **26**, 2011-2015 (2014).

Abstract in Korean

1차원 반도체 나노막대는 매우 작은 크기를 가지고 있으면서도 높은 전자 이동도를 가지고 있으며, 도핑 및 이종구조 제어를 통해 자유자재로 밴드갭 엔지니어링이 가능하여 미래의 전자소자와 광전자소자의 핵심 구성요소로 각광을 받고 있다. 한편 그래핀과 같은 2차원 나노소재는 뛰어난 전기와 열 전도도를 지니고 있으며, 원자층 단위의 매우 얇은 두께를 가지면서도 높은 물리적 강도와 유연성을 지니고 있어 소자에 유연성, 전사가능성과 같은 새로운 특성을 부여할 수 있다. 본 연구에서는 1차원과 2차원 나노소재를 결합한 복합차원 나노소재를 이용하여 매우 얇고 유연하며 높은 집적도를 가지는 개별 어드레싱이 가능한 나노막대 소자 어레이를 제조하였고 소자의 특성을 분석하였다.

매우 얇고 유연하며 높은 집적도를 가지는 개별 어드레싱이 가능한 나노막대 소자 어레이는 그래핀층 위에 성장한 산화아연 (ZnO) 나노막대 어레이를 이용하며 제조하였다. 개별 어드레싱이 가능한 나노막대 소자를 이용하여 각각의 단일 ZnO 나노막대 소자의 특성을 측정할 수 있었으며, 더 나아가 ZnO 나노막대가 지닌 고유한 광전자 특성과 압전효과를 이용하여 고해상도의 나노광검출기와 나노압전센서를 시연할 수 있었다. 또한 질화갈륨(GaN)/ZnO 나노막대 이종구조를 그래핀 위에 제조하고 발광다이오드(LED)를 만들어 유연성 마이크로 디스플레이 소자로서의 가능성도 확인하였다. 이와 같은 GaN/ZnO 나노막대 이종구조 LED의 효율을 획기적으로 증가시키는 방안으로 금속 코어를 함유한 질화갈륨 마이크로튜브를 제조하여 향상된 LED 특

성 또한 확인할 수 있었다.

또한 그래핀 위에 성장한 반도체 마이크로소재를 기반으로 마이크로 디스플레이 소자를 제조하여 그 가능성을 확인해보았다. 본 연구에서는 패턴된 그래핀 위에 성장한 GaN 마이크로 디스크 LED 어레이를 이용하여 매우 얇으며 개별 어드레싱이 가능한 마이크로 디스크 LED 디스플레이를 제조하였다. 이에 더불어 총천연색의 마이크로 디스플레이를 위해 크기와 모양이 정교하게 조절된 마이크로 피라미드와 도넛 형태의 LED를 제조하였다. 이와 같은 마이크로 LED는 인가전압이나 LED 구조에 변화를 주는 방법으로 발광색상을 조절할 수 있다는 것을 확인하였다.

본 연구에서는 넓은 밴드갭(band gap)을 가지는 ZnO와 GaN와 같은 반도체 이외에도 좁은 밴드갭을 가지는 비화인듐(InAs)과 같은 1차원 반도체 나노막대 또한 그래핀 위에 제조할 수 있다는 것을 소재 성장 연구를 통해 보였다. 높은 밀도의 InAs 나노막대를 그래핀 위에 성장 할 수 있음을 비촉매 분자빔에피탁시(MBE)를 이용하여 시연하였고, 나노막대 이종구조 또한 제조하였다. 투과전자현미경(TEM)을 이용하여 그래핀 위에 성장된 나노막대의 결정구조 등을 분석할 수 있었으며, 고에너지반사전자회절장치(RHEED)를 통해 실시간으로 성장 과정을 관찰하여 성장 원리를 분석할 수 있었다.

마지막으로, 격자 상수의 차이가 많이 나는 넓은 밴드갭과 좁은 밴드갭을 가지는 ZnO와 InAs 나노막대를 그래핀의 각각의 면에 성장하는 새로운 방법으로 수직 방향으로 서로 다른 특성을 가지는 나노막대들을 결합할 수 있다는 것을 시연하였다. 이와 같은 신소재의 구조를 TEM을 통해 분석하였

고, 이 소재를 기반으로 제조한 광검출기의 독특한 특성 또한 확인하였다.

Curriculum Vitae

PERSONAL INFORMATION

Name: Youngbin Tchoe

Born: Seoul, Korea
January 7, 1987.

E-mail: ybtchoe@gmail.com, cybrosio@snu.ac.kr

EDUCATION

Seoul National University, Seoul, Korea
Ph.D. in Physics (M.S./Ph.D. combined course)
* Advisor: Prof. Gyu-Chul Yi Sep. 2011 – Feb. 2018

Sungkyunkwan University, Suwon, Korea
Research Student in Physics
* Advisor: Prof. Jung Hoon Han Sep. 2010 – Aug. 2012

Seoul National University, Seoul, Korea
B.S. in Physics Mar. 2006 – Aug. 2011

JOURNAL PUBLICATIONS

1. "Real-Time Characterization Using in situ RHEED Transmission Mode and TEM for Investigation of the Growth Behaviour of Nanomaterials“ Janghyun Jo, **Youngbin Tchoe**, Gyu-Chul Yi, and Miyoung Kim, *Scientific Reports* 8, 1694 **2018**

2. “*ZnO nanotube waveguide arrays on graphene films for local optical excitation on biological cells*” Hyeonjun Baek, Hankyul Kwak, Minho S Song, Go Eun Ha, Jongwoo Park, **Youngbin Tchoe**, Jerome K Hyun, Hye Yoon Park, Eunji Cheong, Gyu-Chul Yi *APL Materials* 5(4) 046106 2017 **2017**

3. *“Flexible resistive random access memory using NiO$_x$/GaN microdisk arrays fabricated on graphene films”* Keundong Lee, Jong-woo Park, **Youngbin Tchoe**, Jiyoung Yoon, Kunook Chung, Hosang Yoon, Sangik Lee, Chansoo Yoon, Bae Park, Gyu-Chul Yi *Nanotechnology* 28(20) 206202 **2017**

4. “*Microtube Light-Emitting Diode Arrays with Metal Cores*” **Youngbin Tchoe**, Chul-Ho Lee, Jun Beom Park, Hyeonjun Baek, Kunook Chung, Janghyun Jo, Miyoung Kim, and Gyu-Chul Yi,

ACS Nano 10 (3), 3114–3120 **2016**

5. "*Flexible GaN Light-Emitting Diodes Using GaN Microdisks Epitaxial Laterally Overgrown on Graphene Dots*"
Kunook Chung, Hyobin Yoo, Jerome K. Hyun, Hongseok Oh,
Youngbin Tchoe, Keundong Lee, Hyeonjun Baek,
Miyoung Kim, Gyu-Chul Yi
Advanced Materials 28 (35), 7688-7694 **2016**

6. "*Real-time device-scale imaging of conducting filament dynamics in resistive switching materials*"
Keundong Lee, **Youngbin Tchoe**, Hosang Yoon, Hyeonjun Baek,
Kunook Chung, Sangik Lee, Chansoo Yoon, Bae Ho Park, Gyu-Chul Yi
Scientific Reports 6, 27451 **2016**

7. "*Centimeter-sized epitaxial h-BN films*"
Hongseok Oh, Janghyun Jo, **Youngbin Tchoe**, Hosang Yoon, Hyun Hwi Lee,
Sung-Soo Kim, Miyoung Kim, Byeong-Hyeok Sohn, Gyu-Chul Yi
NPG Asia Materials 8 (11), e330 **2016**

8. "*Catalyst-free growth of* $InAs/In_xGa_{1-x}As$ *coaxial nanorod heterostructures on graphene layers using molecular beam epitaxy*"
Youngbin Tchoe, Janghyun Jo, Miyoung Kim, and Gyu-Chul Yi,
NPG Asia Materials 7, e206 **2015**

9. "*Growth and optical characteristics of high-quality ZnO thin films on graphene layers*"
Suk In Park, **Youngbin Tchoe**, Hyeonjun Baek, Jaehyuk Heo,
Jerome K Hyun, Janghyun Jo, Miyoung Kim, Nam-Jung Kim, Gyu-Chul Yi,
APL Materials 3 (1), 016103 **2015**

10. "*Statistical Analysis of Electrical Properties of Octanemonothiol versus Octanedithol in PEDOT: PSS-Electrode Molecular Junctions*"
Hanki Lee, Hyunhak Jeong, Dongu Kim, Wang-Taek Hwang, **Youngbin Tchoe**,
Gyu-Chul Yi, Takhee Lee,
Journal of Nanoscience and Nanotechnology 15 (8), 5937-3941 **2015**

11. "*Variable-Color Light-Emitting Diodes Using GaN Microdonut arrays*"
Youngbin Tchoe, Janghyun Jo, Miyoung Kim, Jae;hyuk Heo,
Geonwook Yoo, Cheolsoo Sone, and Gyu-Chul Yi,
Advanced Materials 26 (19), 3009-3023 **2014**

12. "*Growth and characterizations of GaN micro-rods on graphene films for flexible light emitting diodes*"
Kunook Chung, Hyeonjun Beak, **Youngbin Tchoe**, Hongseok Oh,
Hyobin Yoo, Miyoung Kim, Gyu-Chul Yi,

APL Materials 2 (9), 092512 **2014**

13. "*Skyrmion generation by current*"
Youngbin Tchoe and Jung Hoon Han,
Physical Review B 85, 174416 **2012**

MANUSCRIPTS UNDER PREPARATION

1. "*Integrated ZnO Nanorod Device Arrays on Graphene*"
Youngbin Tchoe, Jun Beom Park, Heehun Kim, Minho S. Song,
Joon Young Park, Hongseok Oh, Keundong Lee, Hosang Yoon, Gyu-Chul Yi
In preparation **2018**

2. "*InAs nanorods/graphene layers/ZnO nanorods hybrid dimensional nanomaterials for broadband solar cell applications*"
Youngbin Tchoe, Jun Beom Park, Janghyun Jo, Heehun Kim, Joon Young Park,
Kunook Chung, Yooleemi Shin, Sunglae Cho, Miyoung Kim, Gyu-Chul Yi
In preparation **2018**

3. "*Monolithic multicolor light-emitting diodes array using semipolar GaN pyramidal nanostructures*"
Youngbin Tchoe, Janghyun Jo, Keundong Lee, Miyoung Kim, Gyu-chul Yi
In preparation **2018**

4. "*Ultrathin and Flexible Microdisplay using GaN microdisk light-emitting diodes grown on graphene dots*"
Youngbin Tchoe, Kunook Chung, Keundong Lee, Jun Beom Park,
Joon Young Park, and Gyu-chul Yi
In preparation **2018**

INERNATIONAL CONFERENCE PRESENTATIONS

[Talk] "*Vertical nanodevice array for flexible high-spatial-resolution sensors*" **Youngbin Tchoe**, Heehun Kim, Minho S. Song, Joon Young Park, Hongseok Oh, Jun Beom Park, Keundong Lee, Hosang Yoon, and Gyu-Chul Yi, MRS 2017 fall, Boston, USA **2017**

[Talk] "*InAs nanorods/graphene layers/ZnO nanorods heterostructures for broadband solar cell applications*", **Youngbin Tchoe**, Jun Beom Park, Janghyun Jo, Heehun Kim, Joon Young Park, Kunook Chung, Yooleemi Shin, Sunglae Cho, Miyoung Kim, Gyu-Chul Yi, OSA Light Energy and the Environment Congress, Colorado, USA **2017**

[Talk] “*Flexible and individually addressable vertical nanotube crossbar arrays on graphene layers*”, **Youngbin Tchoe**, Younggul Song, Jongwoo Park, Heehun Kim, Keundong Lee, Jiyoung Yoon, Jun Beom Park, Hongseok Oh, Hosang Yoon, Takhee Lee, and Gyu-Chul Yi, PACRIM 12, Hawaii, USA **2017**

[Talk] “*Microtube Light-Emitting Diode Arrays with Metal Cores*”, **Youngbin Tchoe**, Chul-Ho Lee, Jun Beom Park, Hyeonjun Baek, Kunook Chung, Janghyun Jo, Miyoung Kim, and Gyu-Chul Yi, MRS spring 2016, Arizona, USA **2016**

[Talk] “*Catalyst-free Growth of $In_xGa_{1-x}As$/InAs Coaxial Nanorod Heterostructures on Graphene Layers Using Molecular Beam Epitaxy*”, **Youngbin Tchoe**, Janghyun Jo, Miyoung Kim, and Gyu-Chul Yi, SSDM 2015, Sapporo, Japan **2015**

[Talk] “*Catalyst-free Growth of $In_xGa_{1-x}As$/InAs Coaxial Nanorod Heterostructures on Graphene Layers Using Molecular Beam Epitaxy*”, **Youngbin Tchoe**, Janghyun Jo, Miyoung Kim, and Gyu-Chul Yi, PACRIM 11, Jeju, Korea **2015**

[Talk] “*Catalyst-free Growth of $In_xGa_{1-x}As$/InAs Coaxial Nanorod Heterostructures on Graphene Layers Using Molecular Beam Epitaxy*”, **Youngbin Tchoe**, Janghyun Jo, Miyoung Kim, and Gyu-Chul Yi, Compound Semiconductor Week 2015, Santa Barbara, USA **2015**

[Talk] “*Catalyst-free growth of $In_xGa_{1-x}As$/InAs core-shell nanorods on graphene layers by molecular beam epitaxy*”, **Youngbin Tchoe**, Janghyun Jo, Miyoung Kim, and Gyu-Chul Yi, ISPSA 2014, Jeju, Korea **2014**

[Talk] “*Variable-color Light-emitting Diodes Using GaN Microdonut Arrays*”, **Youngbin Tchoe**, Janghyun Jo, Miyoung Kim, Jaehyuk Heo, Geonwook Yoo, Cheolsoo Sone, and Gyu-Chul Yi, ICMOVPE XVII, Lausanne, Switzerland **2014**

[Poster] “*Flexible high-spatial-resolution nano-photodiode arrays using 1D+2D hybrid dimensional nanomaterials*”, **Youngbin Tchoe**, Jun Beom Park, Heehun Kim, Minho S. Song, Joon Young Park, Hongseok Oh, Keundong Lee, Hosang Yoon, Gyu-Chul Yi,
ICAMD 2017, Jeju, Korea **2017**

[Poster] “*Microtube Light-Emitting Diode Arrays with Metal Cores*”, **Youngbin Tchoe**, Chul-Ho Lee, Jun Beom Park, Hyeonjun Baek, Kunook Chung, Janghyun Jo, Miyoung Kim, and Gyu-Chul Yi, LEDIA ’16, Yocohama, Japan **2016**

[Poster] “*Variable-color Light-emitting Diodes Using GaN Microdonut Arrays*”, **Youngbin Tchoe**, Janghyun Jo, Miyoung Kim, Jaehyuk Heo, Geonwook Yoo, Cheolsoo Sone, and Gyu-Chul Yi, ICAMD 2013, Jeju, **2013**

Korea

DOMESTIC CONFERENCE PRESENTATIONS

[Talk] "*III-V Nanorod Heterostructures on Graphene Layers for Flexible Imaging Sensor Applications*". **Youngbin Tchoe**, Janghyun Jo, Miyoung Kim, and Gyu-Chul Yi, Optical Society of Korea Summer Meeting 2015, Gyeongju, Korea **2015**

[Talk] "*Catalyst-free growth of* $In_xGa_{1-x}As$*/InAs core-shell nanorods on graphene layers by molecular beam epitaxy*". **Youngbin Tchoe**, Janghyun Jo, Miyoung Kim, and Gyu-Chul Yi, 47th Summer Annual Conference of the Korean Vacuum Society, Gangwon-do, Korea **2014**

[Talk] "*Variable-color Light-emitting Diodes Using GaN Microdonut Arrays*", **Youngbin Tchoe**, Janghyun Jo, Miyoung Kim, Jaehyuk Heo, Geonwook Yoo, Cheolsoo Sone, and Gyu-Chul Yi, 46th Winter Annual Conference of the Korean Vacuum Society, Gangwon-do, Korea **2014**

AWARDS AND SCHOLARSHIP

Science Fellowship (Physics), POSCO TJ Park Foundation	**2014 - 2016**
Excellent presentation award, Applied Physics, Korean Physical Society	**2016**
Brain Korea 21+ Scholarship, Seoul National University	**2014, 2015**
Superior Academic Performance, Seoul National University	**2011, 2012**
The National Scholarship for Science and Engineering	**2006, 2007**

PATENTS

1. "*Light Emitting Diode and Method for Preparing the Same*"
   Jinho Hwang, Daeik Jung, Gunsoo Jin, **Youngbin Tchoe**, Keundong Lee, Gyu-Chul Yi, Korean Patent 10-1807021 (Registered) **2017**

2. "*Apparatus for Providing Tactile Information*"
   Gyu-Chul Ti, Jun Beom Park, **Youngbin Tchoe**
   Korean Patent 10-1790614 (Registered) **2017**

3. “Nano Structure Semiconductor Light Emitting Devices”
Geon Wook Yoo, Gyu-Chul Yi, **Youngbin Tchoe**, Jae Hyuk Heo
Korean Patent 10-2014-0074785 (Pending) **2014**

LAB EXPERTISE

Semiconductor Device Processing

- Highly experienced with ultrathin and ultraflexible device fabrication
- Highly experienced with nano- and micro-structure LED device fabrication

Growth

- Highly experienced with operation and maintenance of MBE
- Catalyst-free semiconductor nanostructures growth on graphene using MBE

Characterizations

- Highly experienced with EL setup, maintenance, and characterizations
- Highly experienced with SEM system maintenance
- RHEED installation, maintenance, characterization, and analysis
- TEM, STEM structural characterizations

Computational Skills

- Developed dynamic spintronics simulator using C/C++ (Monte Carlo Simulation, Runge-Kutta fourth order method) & Windows API for visualization
- Current spreading simulation in GaN nanostructure LEDs using COMSOL Multiphysics 4.3b semiconductor module
- $In_xGa_{1-x}N$/GaN quantum well blue shift & emission color estimation using C/C++